ABSTRACT

DENG, JIA. 3D Nanofabrication Using AFM-Based Ultrasonic Vibration Assisted Nanomachining. (Under the direction of Dr. Jingyan Dong and Dr. Paul H. Cohen).

Nanolithography and nanofabrication processes have significant impact on the recent development of fundamental research areas such as physics, chemistry and biology, as well as the modern electronic devices that have reached nanoscale domain such as optoelectronic devices. Many advanced nanofabrication techniques have been developed and reported to satisfy different requirements in both research areas and applications such as electron-beam lithography. However, it is expensive to use and maintain the equipment. Atomic Force Microscope (AFM) based nanolithography processes provide an alternative approach to nanopatterning with significantly lower cost.

Recently, three dimensional nanostructures have attracted a lot of attention, motivated by many applications in various fields including optics, plasmonics and nanoelectromechanical systems. AFM nanolithography processes are able to create not only two dimensional nanopatterns but also have the great potential to fabricate three dimensional nanostructures. The objectives of this research proposal are to investigate the capability of AFM-based three dimensional nanofabrication processes, to transfer the three dimensional nanostructures from resists to silicon surfaces and to use the three dimensional nanostructures on silicon in applications. Based on the understanding of literature, a novel AFM-based ultrasonic vibration assisted nanomachining system is utilized to develop three dimensional nanofabrication processes. In the system, high-frequency in plane circular xy-vibration was introduced to create a virtual tool, whose diameter is controlled by the amplitude of xy-vibration and is larger than that of a regular AFM tip. Therefore, the feature width of a single trench is tunable. Ultrasonic

vibration of sample in z-direction was introduced to control the depth of single trenches, creating a high-rate 3D nanomachining process. Complicated 3D nanostructures on PMMA are fabricated under both the setpoint force and z-height control modes. Complex contours and both discrete and continuous height changes are able to be fabricated by the novel 3D nanofabrication processes. Results are imaged clearly after cleaning the debris covering on the 3D nanostructures after nanomachining process. The process is validated by fabricating various 3D nanostructures. The advantages and disadvantages are compared between these two control modes. Furthermore, the 3D nanostructures were further transferred from PMMA surfaces onto silicon surfaces using reactive ion etching (RIE) process. Recipes are developed based on the functionality of the etching gas in the transfer process. Tunable selectivity and controllable surface finishes are achieved by varying the flow rate of oxygen.

The developed 3D nanofabrication process is used as a novel technique in two applications, master fabrication for soft lithography and SERS substrates fabrication. 3D nanostructures were reversely molded on PDMS and then duplicated on new PMMA substrates. 3D nanostructures are fabricated, which can be either directly used or transferred on silicon as SERS substrates after coating 80 nm gold layers. They greatly enhanced the intensity of Raman scattering with the enhancement factor of 3.11×10^3. These applications demonstrate the capability of the novel process of AFM-based 3D nanomachining.

3D Nanofabrication Using AFM-Based Ultrasonic Vibration Assisted Nanomachining

by
Jia Deng

A Dissertation Proposal submitted to the Graduate Faculty of
North Carolina State University
in partial fulfillment of the
requirements for the degree of
Doctor of Philosophy

Industrial Engineering

Raleigh, North Carolina

2017

APPROVED BY:

Jingyan Dong Committee Co-Chair	Paul H. Cohen Committee Co-Chair
Yuan-Shin Lee	Chih-Hao Chang Minor Member

DEDICATION

To my parents, Qiyuan Deng and Kehui Zhu.

BIOGRAPHY

Jia Deng was born in Jingzhou, Hubei, China. He received the B.S. degree in Process Equipment and Control Engineering from Wuhan University of Technology, Wuhan, China, in 2010. He received the M.S. degree in Mechanical Engineering from Huazhong University of Science and Technology, Wuhan, China, in 2013. He joined the Ph.D. program in Industrial & Systems Engineering at North Carolina State University in fall 2013. His research focuses on the processes development and applications of 3D AFM-based nanofabrication techniques. Upon graduating, he will join Binghamton University as an assistant professor in the Department of Systems Science and Industrial Engineering.

ACKNOWLEDGMENTS

I would like to acknowledge my co-advisors, Profs. Jingyan Dong and Paul Cohen, for mentoring, supporting and challenging me in the past four years. Their attitude towards research and their personality set themselves as role models for me. This work cannot be accomplished without the guidance from them. At the same time, I also would like to express my gratitude to the rest of my committee, Prof. Yuan-shin Lee and Prof. Chih-Hao Chang, for their valuable thoughts and feedback. In addition, I would like to thank Prof. Consuelo Arellano for taking the role of Graduate School Representative on my committee.

I am truly grateful for the mentoring and help from Profs. Thom Hodgson and Shu-Cherng Fang. I am happy of having an opportunity of being a teaching assistant of Prof. Karen Chen. I also want to express my gratitude to all other faculties and staff in our ISE department. They are always friendly and helpful. I sincerely appreciate the help on my research from some other research groups at NCSU. They are Dr. Xiao Zhang and Mr. Oluwafemi Adelegan from the group of prof. Omer Oralkan, Dr. Shanshan Yao and Mr. Jianxun Cui from the group of Prof. Yong Zhu, Mr. Pratik Sen from the group of Prof. Brendan O'Connor, and Mr. Yaning Zhong from the group of Prof. Gufeng Wang.

This journey becomes so wonderful because of my surrounding colleagues and friends. Your support makes my research a lot easier and my life much better.

TABLE OF CONTENTS

LIST OF TABLES

LIST OF FIGURES

CHAPTER 1 INTRODUCTION

1.1 Motivation

Nanopatterning and nanofabrication processes have significant impacts on the development of modern electronic devices that have reached nanoscale domain, such as optoelectronic devices, as well as fundamental research areas such as physics, chemistry and biology. In order to satisfy the needs from both applied and fundamental research areas, many advanced nanofabrication techniques have been developed and reported, including e-beam lithography, ion beam lithography, x-ray lithography, soft lithography, colloid lithography, and tip-based nanofabrication.

In above techniques, tip-based nanofabrication has been implemented to produce sub-50 nm patterns on various types of sample surfaces, such as polymers, silicon and metals [1-8]. It is a low-cost and easy-to-setup technique. Tools used in tip-based nanofabrication are scanning probe microscopy (SPM). It includes Scanning Tunneling Microscopy (STM) and Atomic Force Microscope (AFM). They can be used both as an image tool and modification tool, providing the in-situ visualization and inspection capabilities of nanomachining. AFM attracted much more concerns than STM in nanofabrication since it can be used as a mechanically modification tool without strict requirements like ultra-high vacuum (UHV) environment and conductive tips. Many two dimensional patterns have been successfully fabricated using AFM based nanofabrication techniques.

Not only two dimensional patterns, but three dimensional nanostructures have attracted a lot of attention recently, motivated by many applications in various fields, including optics, plasmonics and nanoelectromechanical systems. Some three dimensional structures have been fabricated by AFM such as a protruding circle in a pocket and three-layer nanostructure [9], using mechanical scratching through a combined AFM/precision-stage system. Besides AFM-based three dimensional nanofabrication techniques, many other approaches have also been developed for the fabrication of three dimensional nanostructures, such as grayscale e-beam lithography (EBL) [10, 11], laser nanopatterning [12, 13], focused ion beam lithography (IBL) [14-16], and corner lithography [15, 17]. Among those approaches, grayscale EBL is the most competitive one with high resolution and process flexibility. But the capital and maintenance costs are much higher than AFM-based nanofabrication processes.

However, traditional AFM-based nanomachining approaches have several limitations. Direct scratching methods usually have slow machining speed, large interaction force between the tip and sample surfaces and limited life time of tips. Some of the methods need repeated scratches to create just one trench. Features created from the traditional AFM-based nanomachining methods generally have very small width and depth if the set point force is small. It is extremely difficult and inefficient to create nanostructures at large scales, especially for three dimensional nanostructures which often have relatively large depth.

An AFM-based nanofabrication approach regulating by ultrasonic force was developed for high rate nanomachining [18, 19]. In this approach, a high frequency in-plane circular xy-vibration and an ultrasonic frequency vibration in z direction are used to improve the efficacy and efficiency of the nanomachining process. The in-plane circular xy-vibration was used to control the width of features in one machining pass and increase the material removal rate since thin slices of materials are removed in each machining circle. Ultrasonic z-vibration of the sample driven by piezo in z direction results an ultrasonic force between the sample surfaces and the cantilever tip. This ultrasonic force is used to regulate depth of the machined features. One machining pass can create trenches with widths ranging from tens to hundreds of nanometers and depths of a few to tens of nanometers. Based on this high rate AFM-based nanomachining approach, depth control becomes much easier than traditional AFM-based nanomachining approaches. Therefore, it provides a possible approach for us to develop novel AFM-based three dimensional nanofabrication processes.

This research proposal focuses on development of AFM-based three dimensional nanofabrication processes using ultrasonic vibration assisted nanomachining. High precision three dimensional nanostructures will be fabricated by tuning the setpoint force and by controlling the z-height, respectively.

1.2 Research Objectives

The broader objectives of this research are to investigate the capability of AFM-based three dimensional nanofabrication processes, to transfer the three dimensional nanostructures from resists to silicon surfaces and to use the three dimensional nanostructures on silicon in applications.

The specific objectives of this research proposal are as follows:

1) Developing and investigating an AFM-based 3D nanofabrication process in which depths of features are regulated by setpoint force.

   a. Developing a setpoint force regulating AFM-based 3D nanofabrication process.
   b. Identifying critical parameters that affect the process.
   c. Characterizing and analyzing 3D nanostructures fabricated using this novel nanofabrication approach.

2) Developing and investigating an AFM-based 3D nanofabrication process in which depths of features are regulated directly by z-height of the tip.
   a. Developing a direct z-height controlling AFM-based 3D nanofabrication process.
   b. Identifying critical parameters that affect the process.
   c. Characterizing and analyzing 3D nanostructures fabricated using this novel nanofabrication approach.

3) Applying the novel nanofabrication process to make 3D nanostructures on silicon substrates.
   a. Transferring nanostructures from Poly(methyl methacrylate) (PMMA) resists to silicon substrates.
   b. Characterizing the structures on silicon substrates.
   c. Utilizing the 3D nanostructures in applications.

1.3 Dissertation Outline

This dissertation proposal is composed of six chapters. Chapter 2 presents literature review related to nanofabrication processes. Chapter 3 illustrates the content about development of 3D nanofabrication processes. Chapter 4 presents 3D nanofabrication results and analysis. Chapter 5 demonstrate the capability of 3D nanomachining process by a number of applications. The dissertation concludes in Chapter 6 with discussion about the future work.

1.4 Chapter Summary

This chapter discusses the research motivation of developing novel three dimensional nanofabrication processes, which have significant impacts on the development of modern electronic devices that have reached nanoscale domain as well as fundamental research areas. Then it presents the research objectives and contributions, following by the outline of the entire dissertation.

CHAPTER 2 LITERATURE REVIEW

2.1 Overview of Nanofabrication Techniques

Recently, many nanofabrication techniques have been developed and utilized to achieve patterns in nanometer scale in a various way. The representing techniques include electron-beam lithography (EBL), ion-beam lithography (IBL), Extreme Ultraviolet (EUV), X-ray Lithography and soft lithography.

2.1.1 Electron-Beam Lithography

EBL has been widely used as an advanced nanolithography technique to fabricate devices and circuits. The equipment and system of e-beam lithography is developed starting from 1960s. After that, upgrading and optimizations are in progress in order to make e-beam lithography a high throughput and reliable process with higher resolution. The working principle of e-beam lithography system is described as follows: the thermally generated electrons accelerating by a high voltage travel through electrostatic blanking plates with a certain aperture and are focused by focusing lens forming a beam before reaching on the substrate surfaces. The focused electron beam scans over the surfaces in a prescribed manner which describes the desired patterns. Exposed areas of electron-sensitive resists are either removed (positive resist) or kept (negative resist) in developer according to the tone of resists. In general, two pattern generating strategies, project printing and direct writing, are adopted in e-beam lithography. Project printing is an approach projecting a large e-beam pattern in parallel through a mask on the resist layer. Direct writing is using a small e-beam spot directly write on the resists following design paths without the expensive and time-consuming preparation process of the mask.

E-beam lithography has wide applications ranging from the semiconductors to bioscience. Cumming et al. [20] fabricated 3nm NiCr wires with 100 keV e-beam lithography using PMMA as resists. Sub-10 nm features are created on TiO2 using e-beam lithography with overlapping and overexposure techniques [21]. Sub-20 nm COMS FinFET is created using e-beam lithography [22]. Vitor R et al. [23] achieved 2 nm isolated feature size and 5 nm half-pitch in hydrogen silsesquioxane resist. In bioscience, e-beam lithography is also used to fabricate nanostructures such as deep nanofluidic channels on quartz chips to separate DNA [24].

2.1.2 Ion Beam Lithography

Ion beam lithography is a versatile approach to fabricate patterns in nanoscale by physical sputtering, interacting with a resist layer, implantation of ions and local material deposition. Because of its versatility, it can be applied on almost any solid materials. Two types of ion beam lithography techniques are applicable, “projection technique” and “direct-write technique”. The projection technique is similar with traditional photolithography process that projects medium energy ions (typically 100 keV) through a mask for rapid nanofabrication. Broad beams with ions that are created by electric discharge or plasma are used as ion sources in the projection technique. The direct-write technique needs focused ion beams that are generated from Ga liquid metal ion sources (LMIS). This technique is used in focused ion beam (FIB) milling to remove materials physically or locally change the chemical property of materials [25-29].

Li et al. [30] created line patterns with a few nanometer half-pitches by exposing a layer of hydrogen silsesquioxane (HSQ) resist with a scanning focused helium ion beam. Clear line patterns with half-pitch of 4 nm are identified using this lithography technique. This pattern is used as template to transfer patterns onto UV-curable resists using nanoimprint lithography. Baglin et al. [31] explored the characteristics of patterns on PMMA and polystyrene (PS) films on silicon using ion beam lithography technique. Different responses of resists were studied patterning by low-energy H^+, He^+ and Ne^+ beams. Using AFM, they examined the feature profiles created after solvent development process of the polymer layers, and examined the dependence of the polymer responses upon ion species and influences. Gopal et al. [32] fabricated ohmic contacts using metal deposition and patterning methodology based on combined focused ion beam and electron beam induced decomposition of a metal-organic precursor gas.

2.1.3 Extreme Ultraviolet (EUV) and X-Ray Lithography

EUV lithography is a lithography technology using a much smaller wavelength of 13.5 nm than that of deep UV technology to achieve higher resolution in nanoscale. The fabrication of mirrors for EUV is a real challenge because all matter absorbs EUV radiation. The optical components need the high performance molybdenum–silicon multilayer materials and they must be housed in a near-vacuum environment [33]. But the maximum reflectivity of the Mo/Si mirrors is about 70% [34], meaning that a high power and a high sensitive resist are needed.

Lorusso et al. [35] demonstrated the capability of EUV alpha demo tool (ADT) by imaging of contact holes, pattern transfer and successful printing of the contact holes level on a 32 nm SRAM device. Seung et al. [36] synthesized and evaluated a series of tert-butyloxycarbonyl (t-Boc) protected C-4-hydroxyphenyl-calix resorcinarenes derivatives as positive tone molecular glass resists for EUV lithography. After patterning and development, feature sizes of 30 nm with low line edge roughness were obtained by them.

With shorter wavelengths of sub-nanometers, X-ray lithography is another extension of optical lithography, which can practically produce patterns with resolution less than 15nm [37]. A mask with absorbers defines the pattern of replicating on a predeposited resist film on silicon substrate. The chemical reaction between the resist material and the X-ray defines the resist as a negative (cross linking after exposure) or positive one (bond breaking after exposure). The advantages of the X-ray lithography are as follows [38]: the masks can be inspected and repaired unlike that in EUV lithography. The resolution and throughput are high. Structures of high-aspect ratio and on curved surfaces are achievable. The limitations include fundamental diffraction limits and the high cost masks. Applications of X-ray lithography have a wide range [39-42].

Buckley et al. [43] used X-ray lithography with synchrotron radiation to generate gold zone plate replicas from semi-transparent carbon zone plate (ZP) masks with an outer zone width of 75 nm. The template, which has an outer zone width of 40 nm, is fabricated by contamination E-Beam lithography. Di Fabrizio et al. [44] also fabricated different types of ZPs by e-beam lithography and X-ray lithography for various X-ray beam focusing: high resolution ZPs for high resolution beam focusing, multilevel phase ZPs to increase the diffraction efficiency in the desired order and high aspect ratio ZPs for hard X-rays. Su et al. [45] fabricated patterns by direct-write X-ray lithography using a hard X-ray beam focused by a Fresnel zone plate with an outermost zone width of 40 nm, which results in an X-ray beam at 7.5 keV focused to a nano-spot was employed to write arbitrary patterns on a photoresist thin film with a resolution better than 25 nm. Direct-write X-ray lithography is also utilized to fabricate a proof-of-concept Josephson Device on $Bi_2Sr_2CaCu_2O_8+\delta$ Superconducting Oxide using a 17.6 keV synchrotron nanobeam by Truccato et al. [46].

2.1.4 Soft Lithography

Soft lithography is a non-photolithographic strategy using a patterned elastomer (usually polydimethylsiloxane, known as PDMS) as the stamp and mode to create patterns and structures ranging from 30 nm to 100 µm. There are five technique categories [47]: microcontact printing (µCP), replica molding (REM), microtransfer molding (µTM), micromolding in capillaries (MIMIC), and solvent-assisted micromolding (SAMIM). Those techniques are cost effective and very easy to be applied widely on many surfaces using different mold materials [48-50]. They can be used to create three-dimensional structures that light based lithography cannot create by one step. Limitations include the shrinkage of the PDMS and the limited aspect ratio to get precise nanostructures.

Mogi et al. [51] used two-step soft lithography to realize rigid nano/microfluidic devices which have high mechanical and thermal stability, good chemical resistance and replication accuracy. This technique enables the production of rigid nano/micro structures including inlet and outlet ports by utilizing a mold master made from a soft material. Auzelyte et al. [52] employ a nano-molding process using a nature-created master. The curved pattern having 100nm-scale structures is used as the master mold from which nanostructures are replicated onto a flat substrate. Copy of the master surface with dense arrays of 200nm high and 100-120nm wide posts are generated. Results successfully preserve the integrity of the nanostructures. Commercial PDMS stamps have shown limitations in soft lithography with nano-scale resolution due to the low physical toughness and high thermal expansion coefficients, Choi [53] developed a stiffer photocured PDMS, which is specifically for nanosized soft lithography and photopatternable nanofabrications.

2.2 Overview of AFM-Based Nanolithography

Atomic Force Microscopy (AFM) originally designed as a measurement instrument for the morphology of samples [54-56]. An AFM consists of a cantilever with a sharp tip at the end, a photodiode to detect the deflection indicating by a laser beam, controllable xyz moving stages and optical components. A laser beam reflected by cantilever in the AFM detects by a photodiode, which shows the mechanical distortion of the cantilever. Knowing the spring constant of the cantilever, normal and lateral forces are able to be calculated. The force information in raster scanning process can be interpreted as the topographic information.

Besides used as a high-resolution topographic measurement tool, AFM has also been developed as an equipment to modify sample surfaces in various approaches including mechanical direct scratching, dynamic plowing, local anodic oxidation and dip-pen lithography. Nanodots, nanolines and other nanopatterns are fabricated on different materials, such as metals, polymers and semiconductors. Because of the properties of low cost, high precision and flexible control, AFM-based nanolithography approaches have been intensively investigated. The capital investment of AFM is around 50K. However, e-beam and ion-beam lithography requires around 1 million investment and thousands of yearly maintainece fee.

2.2.1 Mechanical Direct Scratching

Mechanical direct scratching process is a most commonly used process in AFM based nanolithography. Friction-induced techniques have been utilized for nanofabrication recently [57-64]. Oxides can be created during scratching process with the increased internal stress and plastic deformation following by the wet (KOH) etching process to etch silicon surface not covered by oxides. The process is tip radius sensitive and normal force related. If the tip radius is relatively small, a relatively small applied normal force help penetrate the silicon surface to a relative deeper location. Grooves form when protruded SiO_x layer cannot compensate the height value that decreased by the removed silicon layer. However, if the tip radius is large and normal force is also not large enough, protuberance forms on silicon surface. Miyake et al. show the mechanistic models in Figure 2.1 [65]. Miyake et al. fabricated protuberance and grooves using a diamond tip with 140 nm radius applying 10 to 90 μN normal forces on silicon surfaces [66]. They also controlled the oxidation level by controlling the diamond tip radius (50, 100, 200nm) and the normal forces (10-40 μN) [67]. Following etching processes by KOH are investigated [67, 68].

As for the purpose of directly removing materials from substrates using direct scratching approach, many researchers have made furrows or grooves on a nanometer scale by

(a) (b)

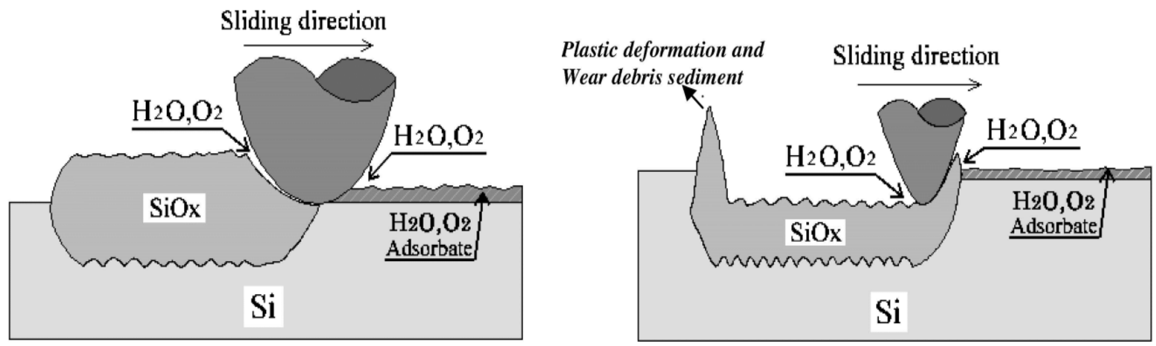

(a) Protuberance processing of silicon (b) Groove processing of silicon

Figure 2.1 Mechanistic models for (a) protuberance and (b) groove processing by diamond tip sliding [65].

applying a relative larger normal force than that in the measuring process on various surfaces. Magno and Bennett [69] used a Si_3N_4 tip in contact mode with a spring constant of 0.37 N/m to fabricate grooves in a GaSb/InAs heterostructure under machining force 100, 125, 150 nN. Resulting trenches penetrated through the GaSb into the InAs, as shown in Figure 2.2. Malekian et al. [70] used a diamond tip with spring constant of 144 N/m to investigate the cutting behavior with 3, 4.5, 6 and 0-6 µN normal force under two cutting speed 0.5 and 5 µm/s. Nanogrooves under 20 nm are fabricated on a chromium workpiece. Rank et al. [71] used a Si_3N_4 tip in non-contact mode with force range of 10-100 µN and a Si contact tip with force range of 17-51 nN to plow lines made of Al and AuPd. Result showed that the larger number of scratches the deeper furrow showed on lines. Sumomogi et al. [72] investigated the scratching process on Cu, Au and Ni using a diamond tip with normal force of 0.5-19.6 µN

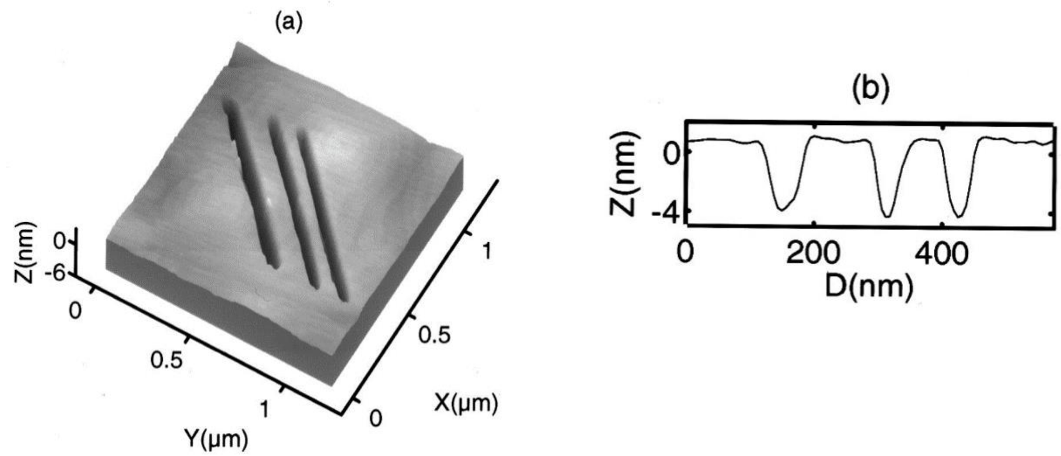

Figure 2.2 (a) Three 0.5 mm long lines scribed in 5 nm GaSb/20 nm InAs, and (b) profile of the lines showing that they penetrate through the GaSb into the InAs [69].

getting flat squares with depth of 5-50 nm. Fang et al. [73] made multiple trenches with a diamond tip of 15 nm radius on a silicon substrate coated with aluminum films under 4, 8, 12 and 16 N. After direct scratching process, further processes such as electrochemical deposition can be utilized to make nanowires. Besides nanomachining can be used leading to an effective doping in graphene.

2.2.2 Dynamic Plowing Lithography

Dynamic plowing lithography (DPL) has been investigated and developed as a commonly used AFM-based nanolithography. The sample surfaces are modified by indenting a vibrating tip under the AFM tapping mode. Patterns on resists are fabricated before transferring onto the substrates, including Si and SiO_2, GaAs/GaAlAs, Au etc. Comparing with the nanoindentation process, it is more efficient and tend to break polymer chain during machining process resulting border walls with loosen debris [74, 75].

Wendel et al. [76] proposed a novel technique using an AFM for integrated nanometer scale lithography on various mask materials, such as photoresist and gold covering a mesa-etched GaAs-AlGaAs heterostructure at ambient conditions. Klehn et al. [77, 78] indented a photoresist layer with a thickness of several nanometers. The pattern was transferred onto a SiO_2 layer on Si by wet etching process resulting in 20-40 nm wide lines. Also, they transfer patterns created by DPL using wet etching process into Si, GaSs and Au films. Skaberna et al. [79] fabricated extremely confined ballistic constrictions. Etching by a strongly diluted aqueous etchant, approximately 30 nm deep grooves were fabricated in the channel area of a modulation-doped GaAs/GaAlAs field-effect transistor. Vasic et al. [80] employed DPL for exfoliated graphene on silicon dioxide substrates. By controlling the tapping force at a moderate level, local strain of the order of 0.1% was generated. Increasing the force to a sufficiently large level, AFM tip can hook graphene and pull it, cutting the graphene along the direction of tip motion. Heyde et al. [81] created patterns on polymethylmethacrylate (PMMA) films. By changing the oscillation amplitude of the cantilever, the indentation depths can be changed. Also, sample surfaces can be either imaged or modified in control. They presented a program to the control of the scanning process. The program can be used to convert the gray scale of pixel images into voltages used to control the dither piezo driving cantilever oscillations thus controlling the indentation depth. He also utilized this DPL to dislocate the antimony culsters that evaporated on graphite surfaces [82].

2.2.3 Bias-Assisted AFM-Based Nanolithography

Electrical energy also has been included in AFM-based nanolithography approaches in order to make modifications on different substrates at the nanometer scale. Researchers investigated the effect of applying bias between conductive AFM tip and substrates. Resists coated on conductive substrates are exposed by electron-flows came out from the conductive tip and formed certain patterns after processing in developer. Majumdar et al. [83] fabricated a pattern with a 35 nm line width and 68 nm periodicity on PMMA films. Wilder et al. [84] demonstrated that the field emission current from the tip is sensitive to the tip-to-sample spacing and fabricated features with sizes below 30 nm in 65-nm-thick resist.

Besides resist exposure, anodic oxidation lithography is another technique that employs electrical energy. The set-up basically is similar to the previous resist exposure approach. The only difference is that the substrates are somewhat conductive materials, meaning metals or semiconductors, other than resists. When applying a bias voltage, the negatively biased tip induces a high electric field in the tip-sample gap, which ionizes the water vapor from the ambient and induces the electrochemical reaction. The field strength decays as the oxide film grows. So the oxide grow process terminates automatically after the electric field is below the critical electric field of the order of 10^9 V/m as discussed by Nemutudi et al. [85]. Yasutake et al. [86] firstly reported the oxidation of Si surface using a biased AFM. Day and Allee [87] created sub-100 lines using conductive tip by performing selective oxidation. Calleja et al. [88, 89] found that short pulses at high voltages helps to create oxidized features on silicon with high aspect ratios. Abdullah et al. [90] systematically studied the effect of relative humidity in the range of 55-72%. Result shows that oxide thickness increase with the relative humidity. In addition to Si substrates, the oxidation of other semiconductors has also been studied such as Si_3N_4, SiGe, GaAs, GaN, SiC [91-96]. Chien et al. [91, 92] investigated the oxide growth of Si_3N_4 and the conversion to SiO_x. Cambel et al. [97] proposed a novel oxidation technology and applied it to InGaP/AlGaAs/GaAs heterostructure with doping layer only 6 nm beneath the surface. Besides semiconductors, AFM local oxidation has been applied to various metals, such as Ti, Al, Cr, Nb, Ni, Mo, and Co [98]. Snow and Campbell [99] created metal wires and metal-oxide-metal junctions by a real-time control and *in-situ* measurement oxidation process. Matsumoto et al. [100] fabricated a single-electron memory using the oxidation process which oxidized the surface of the thin Ti on the atomically flat Al_2O_3 substrate forming the narrow TiO_x line that worked as a tunnel junction for the device.

2.2.4 Dip-Pen Nanolithography

Dip-pen nanolithography has been used to create patterns using a range of inks on a variety of substrates. In this technique, AFM tips act as a "pen", on which chemical compound acting as "ink" and substrates performing as "paper". The capillary force helps transport the molecules from the AFM tip to the substrate at a nanometer scale. Piner et al. [101] developed this direct-write dip-pen nanolithography to deliver collections of molecules in a positive printing mode. He wrote alkanethiols with 30-nanometer linewidth resolution on a gold thin film. Amro et al. [102] developed an approach that can produce desired patterns with multiple components combining the dip-pen lithography and nanografting process. Maynor et al. [103]

used surface-induced reduction of metal ions combined to create metallic nanostructures on Si surfaces, demonstrating DPN is a general method for nanopatterning.

Capability of dip-pen lithography has been enlarged by using tip arrays. Nanoplotters consist of multiple tips are investigated by Hong and Mirkin [104]. They used eight tips to create nanostructures. But only one of the eight tips in the parallel writing mode has the feedback system to monitor tip position and detect force. Zhang [105] developed the concept of nanoplotter by developing two types of devices consisting 32 Si_3N_4 tip and 8 boron-doped Si tips. Nanoscopic monolayer patterns with linewidth in 60 nm level have been fabricated using the silicon tip array. Furthermore, thermally actuated probe arrays were developed by Bullen et al. [106, 107]. The tip array was actuated by passing 10mA of dc current through 2.1mW of heating power to the tips. Using 1-octadecanethiol (ODT) as the ink, they created a 20nm substrate of evaporated gold film on an oxidized silicon wafer, which demonstrated the parallel writing capabilities. Fabrication processes of using tip arrays are widely investigated [108-112].

Many other developments have been made based on DPN. Proteins and biomolecules are patterned using DPN. Lee et al. [113] constructed arrays of proteins with 100 to 350 nm features providing the opportunity to study a variety of surface-mediated biological recognition processes. Salazar et al. [114] fabricate nanopatterned (bio) reactive platforms based on dendrimers on reactive self-assembled monolayer (SAM) and polymer thin films. Hyun et al. [115] fabricated and characterized the stimulus-responsive elastin-like polypeptide (ELP) nanostructures grafted onto ω-substituted thiolates that were patterned onto gold surfaces.

2.3 Overview of 3D Nanofabrication Processes

Three dimensional nanofabrication approaches have attracted a lot of attention recently, motivated by many applications in various fields, such as optics, plasmonics, nanoelectromechanical systems. In order to satisfy the increasing needs of 3D nanostructures, a few 3D nanofabrication approaches have been developed recently. There are some typical approaches, such as grayscale e-beam lithography (EBL) [11, 116-120], laser nanopatterning [12, 13], focused ion beam lithography (IBL) [14-16, 121], and corner lithography [15, 17].

2.3.1 AFM-Based 3D Nanofabrication Techniques

In order to fabricate curvature surfaces or even more complex 3D nanostructures, researchers made efforts by using AFM-based scratching, scribing and machining processes. Commercially available multi-axis stages allow users to move the workpiece. But limiting by the resolution of multi-axis stages, most 3D patterns are actually in micro scale other than nanoscale. Besides direct scratching process, other energy assisted machining process are investigated to create 3D nanostructures.

Yan et al. [9] integrated an AFM with a precision stage in order to solve the problem of nonlinearity and low repeatability positioning accuracy of AFM scanner in a larger scale. They investigated the effects of the tip geometry, the scratching direction, the normal load, the machining velocity and the feed on the machining depth. Using this system, they successfully fabricated three-dimensional micro/nano-structures such as protruding squares and circles on Cu films by diamond tip using AFM-based direct scratching technique. Later on, they further studied the capability of direct scratching technique using the precision stage integrated AFM system [122]. Many 3D patterns are fabricated to demonstrate the capability of the direct scratching technique including 3D human face micro/nanostructures, nanolines/nanodots arrays, and arrays of sine-shaped, hemispheric, and concave/convex nanopatterns. Those 3D nanostructures are fabricated on Al surface using a diamond tip in a controllable and reproducible fashion. Moreover, Mao et al. [123] modified a commercial AFM by replacing its original probe control system with a personal computer (PC) based controller implementing a multi-axes motion control to perform trajectory planning, to test various cutting strategies and to scratch 3D objects.

Besides direct scratching method by changing normal forces applied on metal and polymer surfaces, other energy assisted AFM-based 3D nanofabrication techniques are utilized to generate 3D nanostructures. Knoll et al. [124] used a heated tip to modify an organic material, which could be easier to be scratched under high temperature. As a result, the scratch depth was a function of the normal forces as well as the temperature. A 3D world map is written into a 250 nm thick polyphthalaldehyde layer. Besides that, polymer materials can also be scratched out in a layer by layer method with fixed depths. Pires et al. [120] demonstrated that 3D patterns with a half pitch of 15 nm could be written by simultaneously applying a force and temperature pulse. A microscale replica of the Matterhorm Mountain into a 100-nm thick molecular glass film was fabricated by 120 steps of layer-by-layer removal process ending up to a 25-nm tall 3D nanostructure. Miyake and Kim [125] first scratched Si surface (2x2 μm^2) with relatively high normal force of 25 μN to create a high square protuberance of 0.6 nm oxides. A second area (5x5 μm^2) covering the first area is scratched with a lower load and lower density, which induced a thinner oxidized layer. After KOH solution etching process, a two layer protruding 3D nanostructure of 15 nm and 18 nm is created on the silicon surface.

2.3.2 3D Nanofabrication by E-Beam Lithography

Many researchers have investigated the capability of 3D nanofabrication using grayscale e-beam lithography [10, 11, 119, 126, 127], defocused e-beam lithography [118, 128, 129] and customized apparatus integrated e-beam lithography system [116, 117, 130].

The basic idea of grayscale e-beam lithography is varying the writing dose of electron beam on resist under a certain development time. By changing the exposure dose on resists, depths of affected area change. After a certain development time, 3D micro/nanostructures are able to be fabricated on resists. The reason this 3D nanofabrication technique is called as grayscale e-beam lithography is that it has grayscale gradients represents the height differences. This is distinct from the traditional black and white exposure, which simply block and transmit the photo or e-beam to form a 2D pattern. Procedures of fabricating a 3D micro/nanostructure are as follows. Firstly, an e-beam sensitive resist needs to be spin coated on a silicon substrate. The majority of resists chose by researchers is Polymethylmethacrylate (PMMA). As a positive photoresist, its achievable resolution is very high. Thickness of PMMA film varies according to the concentration of PMMA and the spinning speed. After acquiring a desired PMMA thickness on substrate, relationship between electron dose and depth of clearance needs to be calibrated. Electron beams can be considered as scissors that cutting the polymer chains in PMMA, which increase the solubility of PMMA in its developer. The more intense the dose used, the more polymer chains are cut. That means the higher the dose, the larger depth will form after developing process. However, e-beam lithography tools and environments that using the equipment are not exact the same. Voltages and currents chose by researchers are not always identical. The results on PMMA and silicon are shown in Figure 2.3 [10]. The top view clearly shows the five layers staircase structure. And the cross-sectional view illustrates the height for each layer is around 20 nm, although the walls between layers are not perfectly perpendicular to the floor and surfaces are not perfectly flat. Besides fabricating 3D nanostructures on PMMA surfaces, Kim et al. [10] transferred the 3D nanostructures on to silicon surfaces after fabricating on PMMA surfaces.

As for the defocused e-beam lithography, the exposed patterns depend on the defocusing length of the electron beam in the e-beam lithography. Niemann et al. [129] found this special method and applied it on the optical gratings that with smoother edge roughness. Seung et al. [118] utilized the defocused e-beam lithography to fabricated nanocones and nanolens for SERS (surface enhanced Raman spectroscopy). This is due to the fact that the distribution and intensity of electron beam energy are changed by the defocusing length degree.

Yamazaki et al. [116, 117, 130] developed a two-axis-of-rotation drive system which enables e-beam lithography to be applied to 3D nanofabrication. This apparatus with a positional accuracy of a few milliradians can be loaded into the e-beam lithography system, allowing exposure of the resists from various directions and fabricating 3D nanostructures. A smallest globe has been fabricated with a minimum feather size of 10 nm over the world map. Besides, 3D nanostructures with high aspect ratio were also fabricated by suppression the proximity effect.

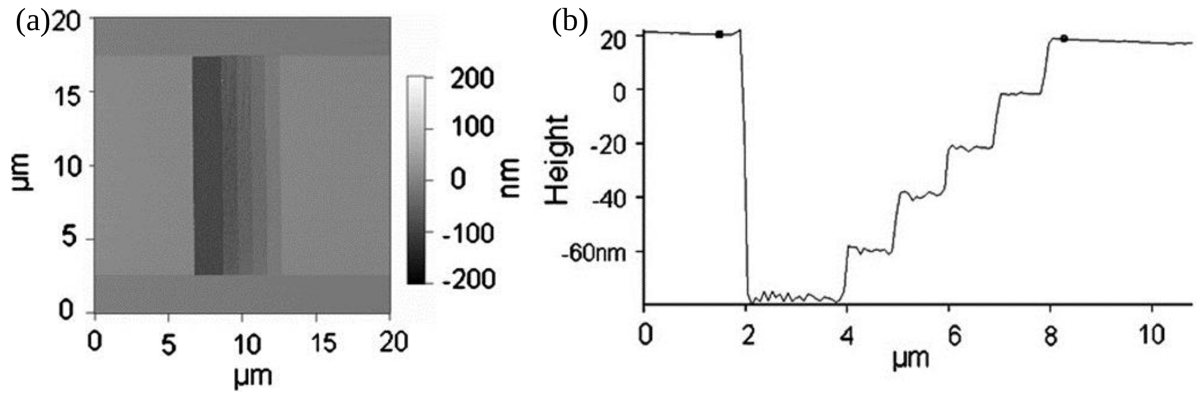

Figure 2.3 (a) Top view and (b) cross-section of the remaining resist profiles, after development, of the staircase structures transferred onto PMMA on Si when the step width is 1.0 µm [10].

2.3.3 3D Nanofabrication by Other Techniques

Many other techniques have been investigated to fabricate 3D nanostructures on resists and semiconductor substrates, including focused ion beam lithography, nanoimprint lithography and colloidal lithography.

The focused ion beam lithography based 3D fabrication process is similar to e-beam lithography, as shown in figure 2.4 [131]. Firstly, spinning coat a thin layer of resist on silicon substrates. Secondly, bake on hot plate for a certain time to dissipate surplus solvents. Then focused ion beam is used to damage the polymer bonds by the chain scission of positive resists or the cross-link of negative resists. After that, a certain developer is applied for a certain time to generate 3D nanostructures on the surface. Then after transferring 3D patterns from resist layer to silicon layer, striping process is employed.

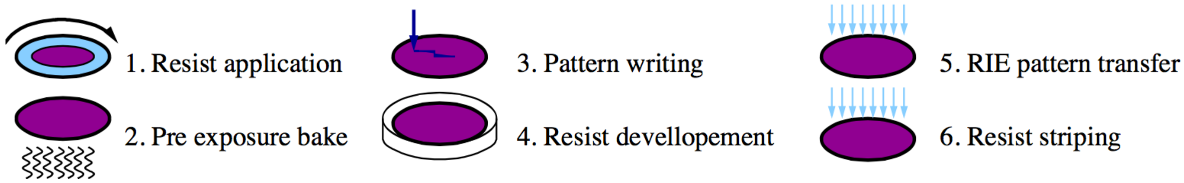

Figure 2.4 Focused ion beam 3D fabrication process [131]

Li et al. [16] investigated a high-resolution patterning method suitable for nanocontact imprinting using focused ion beam. Different ion beam currents, milling times and dwell times are optimized to create single-pixel lines and 3D nanodots on a silicon master and replicated on polydimethylsiloxane through replica molding. Taniguchi et al. [121] investigated the characteristics of focused ion beam lithography for spin-on-glass(SOG) and PMMA using 30 kV acceleration voltage and 0.35 pA current. A six layer staircase is fabricated on SOG, which is clearer than the same pattern on PMMA. Wald et al. [132] employed an additional layer absorbing the implanted Ga and enabled 3D nanopatterning with sub-100 nm lateral resolution in conjunction with smooth height transitions and surface roughness down to 4 nm root mean square. At the same time, they demonstrated that the surface roughness experienced following etching is linked to the presence of Ga in the Si substrate.

3D nanoimprint lithography is a contact nanolithography process using 3D nanomolds and UV-curable imprint resist material to reversely replicate the 3D nanostructures in the molds, which has been implemented by many researchers [133-138]. Wu et al. [133] fabricated 3D cone arrays with tip radius around 10 nm on a UV-curable resist, composed of a low viscosity UV-curable acrylated poly(dimethylsiloxane) material. The process contains four phases: fabrication of the master mold on silicon; duplication of a daughter mold with reversed patterns on cross-linked polymers; formation of polymer cones on a substrate; finalization with metal coating. Faithful replications of cones with both small and large aspect ratios are fabricated. Konijn et al. [136] fabricated multilevel imprint molds with sub-100 nm dimensions on silicon nitride using varying dosage of e-beam lithography. Parallel lines with increasing heights and other 3D nanostructures are fabricated by nanoimprint lithography.

Burouni et al. [17] investigated the repeated corner lithography, obtaining sub-50 nm apertures. This innovative technique can control the aperture size and feature by initial layer thickness of nitride and proper choice of processing temperature and oxidation time. Yesilkoy et al. [139] studied a novel fabrication method for 3D metal nanostructures by high-throughput nanostencil lithography. They utilized 100 nm thick stencils created by e-beam lithography and physical vapor deposition to fabricate complex topographies at the nanoscale.

2.4 Applications of 3D Nanostructures

3D nanostructures have been fabricated on various materials including semiconductors, metals and polymers. They are fabricated and investigated in many applications, such as 3D nanochannels in fluidic deivces [140-142], 3D plasmonic nanostructures [143-145] with extraordinary optical transmission phenomenon, 3D nanofocusing structure [146-149] and some 3D nanostructures for supercapacitors [150-152].

Ma et al. [140] used the silicon sidewall scallops creating by EBL and silicon etching process to fabricate 3D nano-fence matrixes for nanofluidic channels. They integrate the micro-channel into nano-channels, which will be very useful for fluid purification, segregation and bias application in certain fluid detection. Perry et al. [141] fabricated nanochannel masters with symmetric pores and asymmetric funnels are written in the negative-tone resist SU-8 by e-beam lithography and shaped by Electron-Beam-Induced Etching (EBIE) with H_2O as the precursor gas. They measured current - voltage (I-V) curves for funnels cast from unmodified and EBIE-modified masters. Stavis et al. [142] fabricated a prototype 3D nanofluidic device utilizing a single layer of grayscale photolithography and standard integrated circuit manufacturing tools. It shows implements size exclusion of rigid nanoparticles and variable nanoscale confinement and deformation of biomolecules.

Choo et al. [146, 147] demonstrated a highly efficient on-chip three-dimensional linear-tapering metal-insulator-metal (MIM) nanoplasmonic photon compressor (3D NPC). In a two-photon luminescence measurement, the device achieved an intensity enhancement of 400 within a 14×80 nm^2 area, and a transmittance of 74%. Lindguist et al. [153] demonstrated the design, fabrication and characterization of a near-field plasmonic nanofocusing probe with a hybrid tip-plus-aperture design. The combination of large transmission through a C-shaped aperture aligned to the sharp apex (<10 nm radius) of a template-stripped metallic pyramid allows the efficient delivery of light—via the C-shaped aperture—while providing a nanometric hotspot determined by the sharpness of the tip itself. Lindguist et al. [148] also demonstrate three-dimensional plasmonic nanofocusing of light with patterned metallic pyramids obtained via template stripping. Gratings on the faces of these pyramids convert linearly polarized light into plasmons that propagate toward and converge at a ∼10 nm apex.

Results of experiments and computer simulations confirm that optical energy is focused into a nanoscale volume (5×10^{-5} wavelength^3).

Zhu et al. [152] demonstrated an efficient approach for large-scale production of 4 nm thick V_2O_5 nanosheets, which is utilized as building blocks for constructing 3D architectures via a freeze-drying process. The resulting highly flexible V_2O_5 structures have ultrathin walls, and multilevel pores, which can be used to fabricate supercapacitor with capacitance retention after 4000 cycles is more than 90%, and the energy density is up to 107 $W \cdot h \cdot kg^{-1}$ at a high power density of 9.4 $kW \cdot kg^{-1}$. Mao et al. used an adsorption-hydrothermal strategy for the *in-situ* growth of ~ 40 % $Ni(OH)_2$ nanoplates in three dimensional nitrogen-containing graphene hydrogel (NG), which achieves a high specific capacitance of 782 $F \cdot g^{-1}$ at the current density of 0.2 $A \cdot g^{-1}$, which equals to a specific capacitance of 1748 $F \cdot g^{-1}$ based on the mass of $Ni(OH)_2$ alone. Extraordinary cycling stability is also achieved that only 10% capacitance loss after 10,000 cycles.

2.5 Chapter Summary

This chapter discusses the overview of literatures. Firstly, the nanofabrication techniques are discussed, including E-Beam, Ion beam, EUV, X-ray and soft lithography. Then different AFM-based nanofabrication processes are discussed in details. Moreover, 3D nanofabrication techniques are overviewed. Grayscale e-beam lithography, direct-write ion beam lithography and other techniques are discussed. Finally, the applications such as nanofocusing photon compressor and superconductors using 3D nanostructures are reviewed.

CHAPTER 3 3D NANOFABRICATION PROCESSES DEVELOPMENT

3.1 Introduction of the Nanomachining System

In order to fabricate 3D nanostructures with good controllability, high throughput, and high flexibility, ultrasonic vibration assisted 3D nanomachining processes are developed to fulfill the requirements. The 3D nanomachining processes are developed and implemented by an experimental setup customized and constructed in the Micro/Nanomanufacturing Laboratory. The experimental setup consists of a commercial AFM system and a customized stage, which provides high speed in plane xy-vibration and ultrasonic z-vibration. Hardware and functions of the experimental setup are described and discussed in detail in the following sections.

3.1.1 Hardware of the Nanomachining System

Figure 3.1 illustrates the schematic of the experimental setup. By integrating a lab-designed nanovibrator with a commercial AFM from Park Systems, the base 3D nanomachining process is constructed. The nanovibrator is driven by stack piezo actuators in x and y directions, generating high frequency in plane xy-vibration. Another ultrasonic frequency piezo actuator is attached on the top of the pillar, standing in the center of the nanovibrator stage and providing ultrasonic vibration to the sample attached on the top of it. Piezo actuators are driven by sinusoid signals with appropriate voltages, generated from a commercial signal output device from National Instruments. The laser beam in the AFM reflected from the backside surface of the cantilever reflects the setpoint force between the tip and substrate. It can be also used to measure the deflection, also the normal force, of the cantilever. Signals from the laser beam are transmitted to the signal access module to collect and monitor them. Details about the hardware are described in the following subsections.

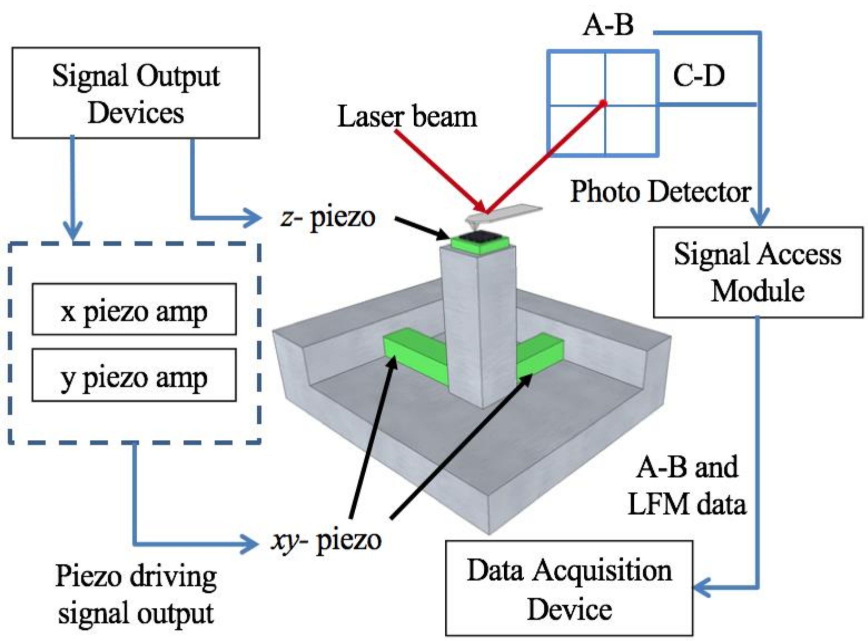

Figure 3.1 Schematic illustration of experimental setup.

3.1.1.1 Atomic Force Microscope

AFM is originally designed as an instrument for measuring the physical morphology of different solid samples with great resolution as high as sub-nanometer. An AFM consists of many components. The major ones are a cantilever with a sharp tip at the end, which can be various materials; a photodiode to detect and the movement of a laser beam, which indicates the deflection of the cantilever; controllable moving stages in all three dimensions. Knowing the spring constant of the cantilever, normal and lateral forces are able to be calculated through the deflection of the cantilever. Besides as a tool of acquiring images, AFM has also been used as an equipment to modify sample surfaces in various approaches. Our research group modified it into a nanomachining platform to generate 2D patterns as well as complicated 3D nanostructures.

The AFM we used for the experiments is a commercial product XE-70 system from Park Systems. The three components are the XE-70 AFM stage, the XE-70 control electronics and a computer with monitors. Figure 3.2 shows the XE-70 AFM stage, which includes an X-Y scanner fixed on an X-Y stage, a Z scanner carried by a Z stage, an illuminator cable, a CCD camera, an objective lens and focus-adjusting knob.

By the orthogonal design of all three scanner's axes, the cross-talk problems between each two of the scanner's axes are eliminated. The range of the XY scanner is 50 μm × 50 μm. The parallel Kinematics design makes the X-Y scanner has low inertia and axis-independent performance. The Z scanner can move up to 12 μm. It is able to maintain constant feedback conditions as it is moved such as constant setpoint force and constant height. The Z stage can be adjusted up and down with a movement range of 29 mm. The X-Y stage has a rage of 25 mm in both X and Y axes and is used to fix the sample and adjust it to an appropriate position that can be illuminated by lights from the optical components.

The optical components in the AFM stage are used to manually focus the laser beam onto the backside of the cantilever and to locate the cantilever to targeted regions on the sample surfaces. The 10X objective lens yields about 500 times magnification. The whole stage is carried by a mechanical vibration isolation platform to get rid of the affect from environmental noise and vibrations. The nanovibrator is screw-tightened on the X-Y scanner to utilize the precise X-Y directional movement of it. Details of the nanovibrator are described later.

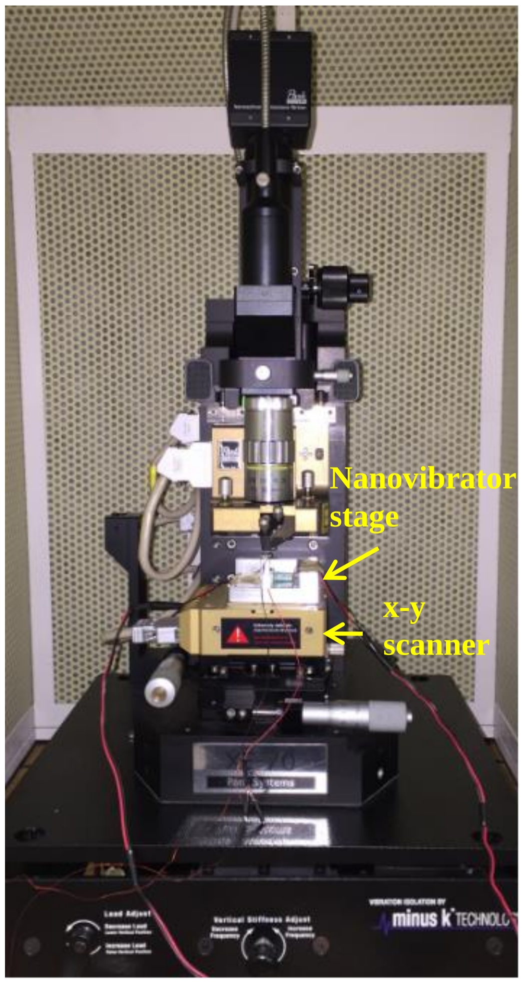

Figure 3.2 XE-70 AFM stage with customized nanovibrator

3.1.1.2 Customized Nanovibrator

Figure 3.3 shows the nanovibrator stage amounted on the AFM X-Y scanner. Its function is to provide high frequency in plane circular xy-vibration and ultrasonic z-

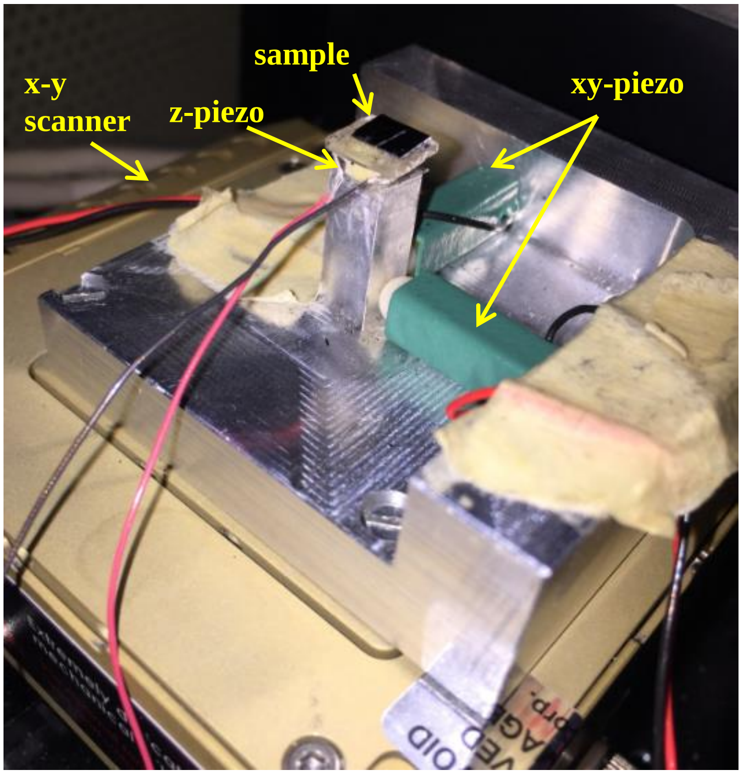

Figure 3.3 Nanovibrator stage amounted on the AFM X-Y scanner

vibration. The entire nanovibrator stage is made of aluminum. In the center, there is an extruding pillar with the dimension of 6 × 6 × 15 mm, which is vibrated to create an in-plane circular xy-vibration. The pillar is driven by two piezo actuators in x and y axes, which are fixed perpendicularly to each other at the bottom of the pillar. Two identical xy piezo actuators which touched the bottom of the pillar generate displacements when applying the command signal. The sinusoid signals with the 90 degree of phase difference and the same amplitude applying on x and y piezo actuator cause a circular vibration at the bottom of the pillar. The vibration can be transmitted from the bottom to the top of the pillar. On the top, the z piezo actuator is able to provide a Mega-Hz level ultrasonic vibration in the z direction, which has the AFM tip penetrates into PMMA samples.

Figure 3.4 (a) shows the x/y piezo actuator in the nanovibrator stage. They are low voltage co-fired multilayer stacks piezo actuators from APC International Ltd. The type of xy piezo actuators is PSt 150/5×5/20 with their specifications listed in Table 3.1. And the z piezo actuator is shown in Figure 3.4 (b). The type of z piezo actuator is PSt 150/3×3/2 with specifications listed in Table 3.1.

(a)

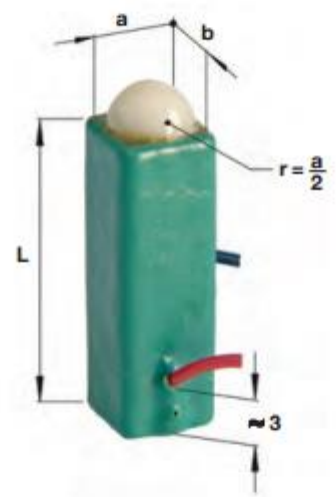

(b)

Figure 3.4 (a) X/Y piezo actuator. (b) Z piezo actuator

Table 3.1 Specifications of xy piezo actuators and z piezo actuator

	X/Y piezo actuators (Type: PSt 150/5×5/20 U_{max}=150 V)	Z piezo actuators (Type: PSt 150/3×3/2 U_{max}=150 V)
Cross-section (a×b) (mm×mm)	5 × 5	3 × 3
Thickness (L) (mm)	18	2
Max. Stroke (µm)	20	>2
Capacitance (nF)	1800	30
Resonance frequency (kHz)	50	>500
Stiffness (N/µm)	60	190
Blocking force (N)	1600	500
Max. load force (N)	2000	500

3.1.1.3 Driving Signal Generation and Data Acquisition

Driving signals are required for xy piezo actuators to vibrate under a certain frequency and amplitude. Figure 3.5 (a) shows the National Instrument (NI) USB-6259 from which the driving signals are generated. It connects with the computer, also one of three major components of the XE-70 systems. Signal Express is the software that installed in the computer to output the driving signals through the NI USB-6259. It also used to acquire signal feedback from the AFM, to record, analyze and present signals. The output channels of the NI device AO 0 and AO 3 are used to provide driving signals for x and y piezo actuators. The voltage, however, is not high enough, and two amplifiers are used to amplify the signals from the NI device. They are VF-500 amplifiers from DSM with the gain of 20 and a bandwidth around 5kHz. The input channel of AI 0 collects data of A-B signal, which reflects the deflection of the AFM cantilever. The input channel of AI 1 collects data of C-D signal, which reflects the torsion of the AFM cantilever. The input channel of AI 2 collects data of Z DET value, which reflects the absolute height value of z scanner in AFM. Figure 3.5 (b) shows the Agilent 33220A function generator for the z piezo actuator, providing 0-10 V driving signals.

(a)

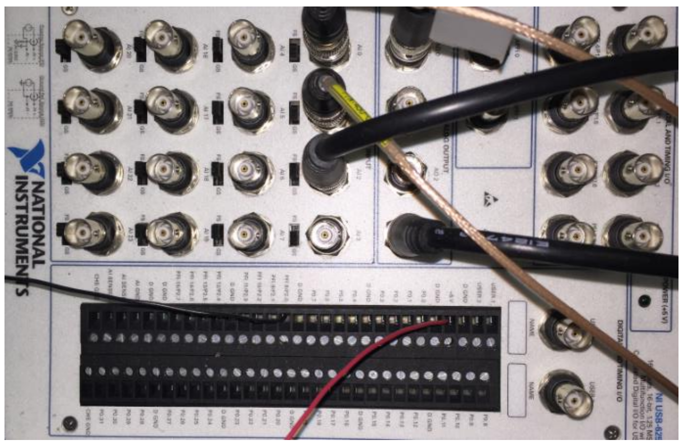

(b)

Figure 3.5 (a) NI USB-6259 data generation and acquisition module. (b) Agilent 33220A function generator.

3.1.1.4 Sample Material and Cantilevers Used in Experiments

The sample material we used is PMMA, which is a commonly used resist for photolithography and EBL. And it is a polymer, which is easy to be machined. PMMA (950 PMMA A4 from Microchem, 4% dilution in anisole) film was spin coated on cleaned silicon wafers at 4000 RPM for 40 s by a Headway Spinner. Then silicon wafers were baked at 180 °C for 90s. The final PMMA thickness is around 200 nm. In order to transfer 3D nanostructures from PMMA surfaces on to silicon surfaces with high fidelity and quality, it is helpful to decrease the residual layer after 3D nanofabrication process, PMMA with 100 nm thickness were also spin coated on silicon substrates by using 950 PMMA A2 from Microchem, 2% dilution in anisole. Other operations and parameters are the same.

Tips used in experiments should have the property of high wear resistance, since 3D nanomachining process needs to remove a relative large amount of sample material. Small tip radius is also necessary since the initial process before nanomachining is the indentation process. This process will be more efficient with smaller tip radius. Also, small tip radius helps increase the resolution of 3D nanostructures. Also, relatively large spring constant of the AFM tip ensures the first indentation of the tip into sample surfaces and maintaining enough nanomachining forces during nanofabrication process. Moreover, resonant frequency is also important for our experimental set up. Small resonant frequency has better "freezing" effect when applying the ultrasonic vibration in z direction.

From the requirements of tips discussed above and pilot experimental results. We chose the AFM probe Tap 190 DLC from Budget Sensor. This tip has diamond-like-carbon

(DLC) coatings on silicon body. Specifications of the tip are listed in Table 3.2. The same tip that is used in the machining process is also used to image the features under non-contact mode directly after the machining process because of the negligible wear.

Table 3.2 Specifications of the Tap 190 DLC AFM tip

	Value	Range
Resonant Frequency	190 kHz	$\pm$ 60 kHz
Force Constant	48 N/m	20 N/m to 100 N/m
Length	225 µm	$\pm$ 12 µm
Mean Width	38 µm	$\pm$ 9 µm
Thickness	7 µm	$\pm$ 1 µm
Tip Height	17 µm	$\pm$ 2 µm
Tip Set back	15 µm	$\pm$ 5 µm
Tip Radius	< 15 µm	
Half Cone Angle	20°-25° along cantilever axis 25°-30° from side 10° at the apex	

3.1.2 Functions of the Nanomachining System

Figure 3.6 (a) illustrates the nanomachining process of a single trench using ultrasonic assisted nanomachining. It is easy to fabricated single trenches with widths of tens or a few hundred nanometers and depths of tens of nanometers with the help of high frequency xy vibration and ultrasonic z vibration. The process is similar with the fly cutting process in the conventional scale with a single point tool. The cutting edge of the nanomachining is the edge of the AFM tip in touch with the sample material at a specific moment and varies as the tool is fed.

In the 3D nanofabrication system, two piezoelectric actuators are driven by sinusoid signals with 90 degree phase difference in x and y directions to generate sinusoid displacements. Therefore, an in-plane circular xy-vibration is generated between the tip and the sample, which effectively forms a virtual tool for the machining processes, as shown in Figure 3.6 (b). The blue circle shows the diameter of the virtual tool, forming by the red circle, which is the circular motion induced by xy-vibration, and the black dot circle, which is the diameter of the AFM tip. The virtual tool is formed from the AFM tip and the circular motion of the xy-vibration. The Radius of the virtual tool R' can be expressed as:

$$R' = R + r \qquad \text{(Eq. 3.1)}$$

where, R is the radius of the AFM tip at a certain height, and r is the radius of the circular motion. With high frequency circular xy-vibration, only a thin slice of sample material is removed in one machining cycle, which greatly enhances the machining speed and reduces tip-sample interaction force. The machining speed can be expressed as:

$$V = f * FPR \qquad \text{(Eq. 3.2)}$$

where f is the vibrational frequency, FPR is the feed per rotation. The regular trench width with 30 mV xy-vibrational driving voltage is around 100 nm. Therefore, it is reasonable to choose 1-10 nm feed per rotation without a rough trench wall. With the vibrational frequency of 2-10 kHz, the nanomachining speed can be chosen in a range of 2-100 µm/s. It is a widely applicable range that we can choose to optimize the machining process. If the requirement of

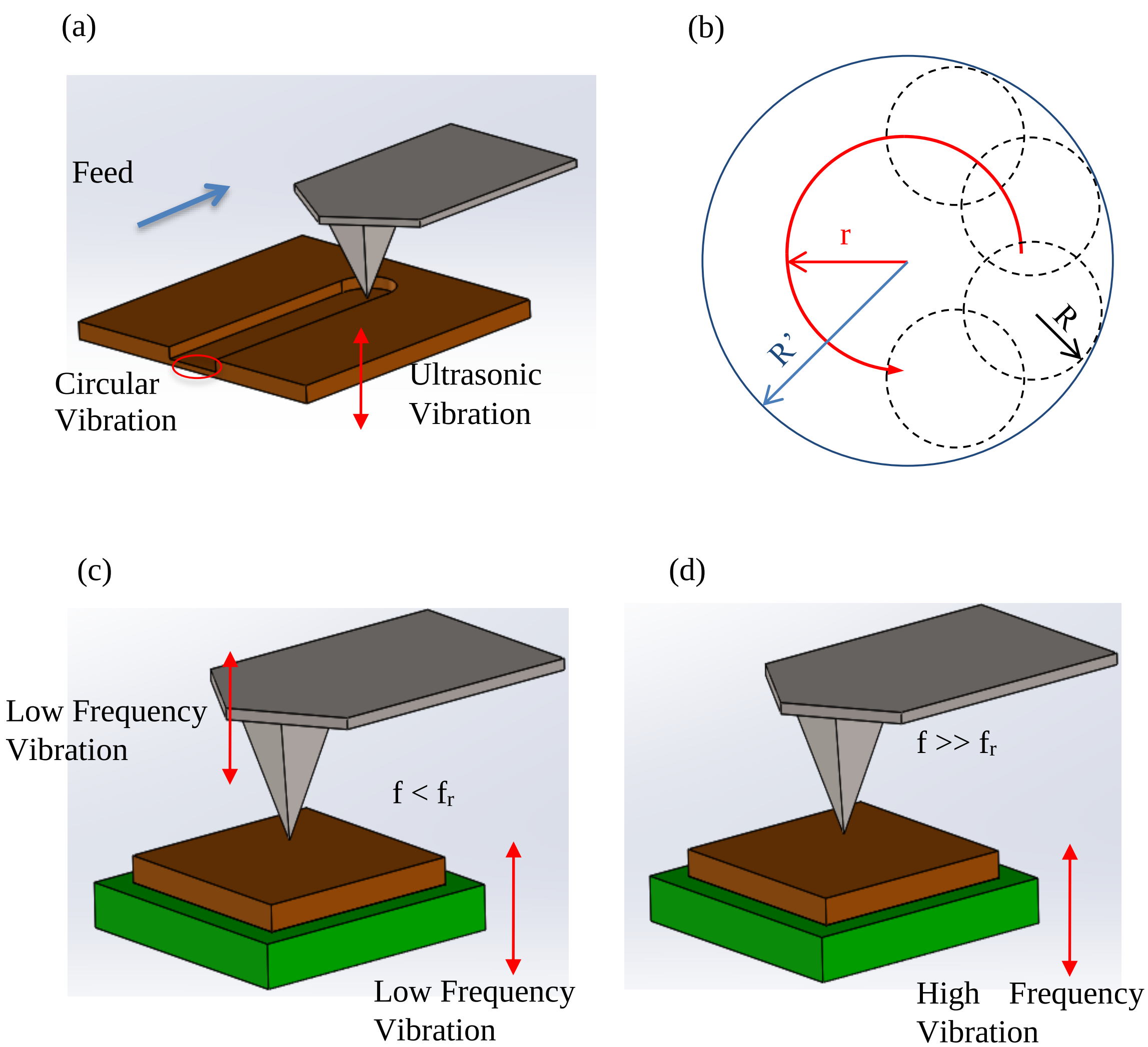

Figure 3.6 (a) Schematic illustration of ultrasonic vibration assisted nanomachining. (b) Virtual tool when tip is vibrated with a xy circular path. (c) Tip-sample interaction with z-vibration in low frequency. Tip vibrates with z-piezo. (d) Tip-sample interaction with z-vibration in ultrasonic frequency. Tip does not vibrate with z-piezo, “freezing” at the current location.

the surface finish is critical, we may slow down the machining speed. But if the area to be machined is large and we do not care about the final surface finish, very high nanomachining speed can be chosen, which is extremely hard to achieve by other nanofabrication techniques. Besides the high machining speed, the diameter of the virtual tool is linearly related with the xy-vibration amplitude, which directly regulates the feature width machined in one single path. The larger the xy-vibrational amplitude is, the larger the diameter of the virtual tool and also the width of the single machining trench created on PMMA.

Ultrasonic z-vibration is used to reduce the frictional force and to increase the depth of feature during nanomachining processes. When z piezoelectric actuator drives samples to a frequency less than the resonant frequency of the cantilever ($f < f_r$), the cantilever, contacting with the sample surface, follows the vibration of samples, as shown in Figure 3.6 (c). But when z-vibrational driving frequency is much higher than the resonant frequency of the cantilever ($f >> f_r$), the cantilever dynamically 'freezes' due to its inertia and the AFM tip is able to penetrates into sample surfaces with the help of ultrasonic vibration, as shown in Figure 3.6 (d). The feature depths are controlled by the amplitude of z-vibration. The larger the amplitude, the deeper the features are. In actual experiments, it is controlled at a certain level around 2V. Besides the depths between tip and sample controlled by the z piezoelectric actuator, lateral displacements of the pillar make the top surface tilt to some extent. If the tilting angle is large, the machining depths of trenches increase at the top-right area and decrease at the bottom-left area. The reason is that the two piezo actuators in x and y direction push the pillar toward the left and bottom, respectively. However, the tilting angle of the top surface is extremely small that there is only around 10 nm height change across a 3 mm lateral distance. Thus, changes of height in z-direction caused by xy-vibration are negligible since lateral dimensions of 3D nanostructures are often in the level of a few micrometers.

3.2 Development of 3D Nanomachining Approaches

Based on the experimental set up and the effects of different input parameters, we are able to tune the parameters to achieve different depths. By designing and fabricating various depths on 2D pocket patterns, 3D nanostructures can be fabricated. Two 3D nanofabrication approaches are developed based on two depth control modes, setpoint force control mode and z-height control mode. Under the setpoint force mode, the interaction forces (reflected by the cantilever deflection) between the tip and the sample is close-loop controlled is specified by the user. Under the z-height control mode, the absolute height of z scanner (reflected by the cantilever deflection) is open loop controlled as specified by the user.

3.2.1 3D Nanomachining under Setpoint Force Control Mode

With the experimental set up, it is possible to create single trenches with depths from a few nanometers to hundreds of nanometers when machining PMMA. For example, single trenches are created when input parameters are chosen as follows: 30 mV driving voltage of xy-vibration (which is an experimental value we generally use); 3 V driving voltage of z-vibration and 1 μm/s nanomachining speed. The results of trenches on PMMA are shown in Figure 3.7 (a). Four trenches are fabricated under setpoint force control mode with a gradually increasing setpoint force from 50 nN to 500 nN, increasing by 150 nN. Resulting trenches have depths of 0, 14, 33, 52 nm, respectively. The result concords with the effect of the setpoint

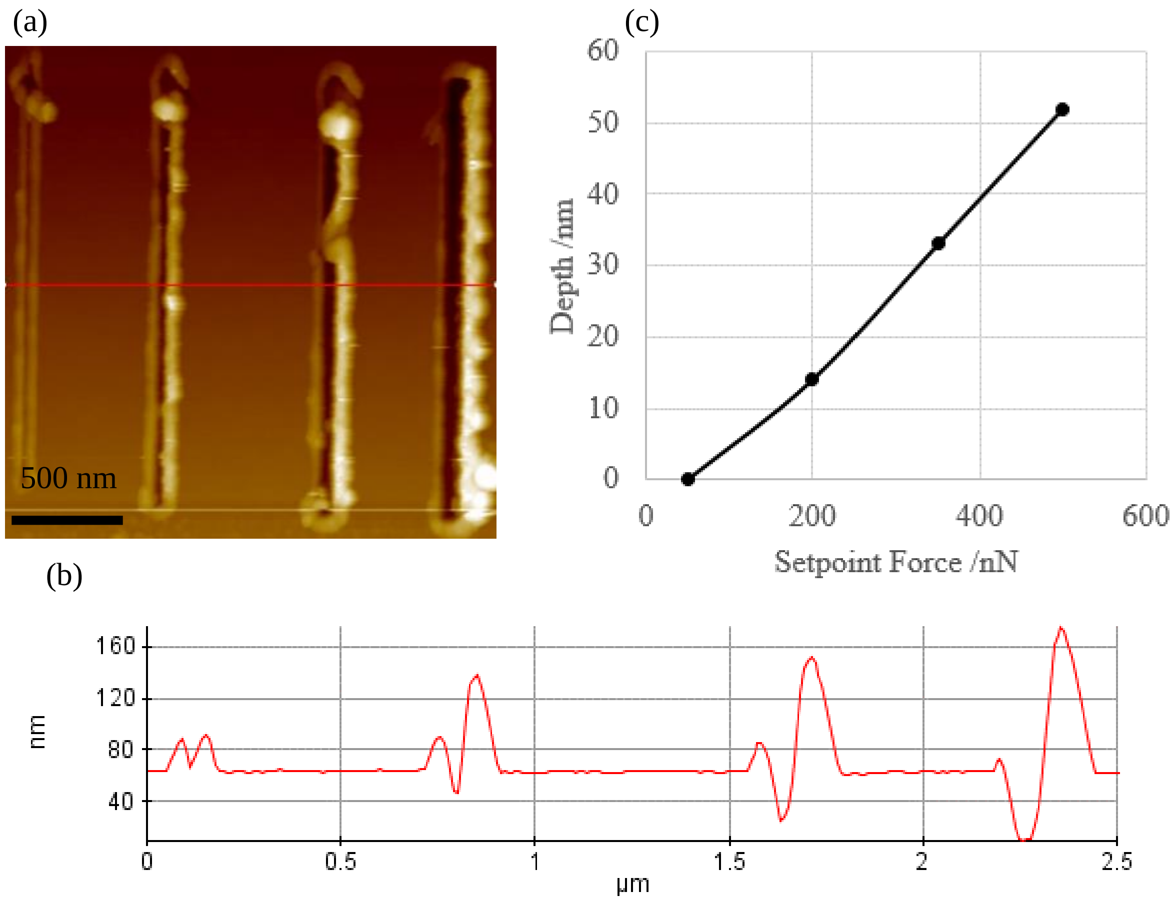

Figure 3.7 (a) Trenches on PMMA fabricated under the setpoint force control mode with setpoint forces of 50, 200, 350, 500 nN with 30 mV driving voltage of xy-vibration and 3 V driving voltage of z-vibration. (b) Cross-sectional profile of the trenches. (c) Trench depth and setpoint force relationship

force from 50 nN to 500 nN, increasing by 150 nN. Resulting trenches have depths of 0, 14, 33, and 52 nm, respectively. The result concords with the effect of the setpoint force our research group demonstrated previously. The larger the setpoint forces applying on the sample, the deeper the trenches are. Figure 3.7 (c) shows a linear relationship between the force and the depths.

Because of the tunable depths possible by controlling the setpoint force, 3D nanostructures are able to be fabricated. The first step is to verify the capability of extending the machining area by combining the machining trenches together. And the features of pockets are also need to be examined and analyzed.

From previous results and analysis of single trenches, pocket patterns are designed to investigate the capability and potential of the 3D nanomachining. Pockets on PMMA fabricated under setpoint force control mode are designed in 10 vectors representing 10 nanotrenches with 25 nm distance between adjacent two vectors, as shown in Figure 3.8 (b). From the results of single trenches above, it is reasonable to choose a relatively small setpoint force to fabricate depths appropriate for the pocket feature. The setpoint forces were set as 100 nN, 150 nN, and 200 nN from the left pocket to the right one. The driving voltage of xy-vibration was set as usual 30 mV and driving voltage of z-vibration was 3 V.

Figure 3.8 (a) shows the results of combining 10 vectors for each pocket. Figure 3.8 (d) shows the cross-sectional profile of the 3 pockets on PMMA. The readings, given in Figure 3.8 (c), indicate that the depths of the three pockets are around 15 nm, 25 nm and 43 nm, respectively. The depths of the pockets are increasing along with the increasing setpoint force. The result shows that it is possible to combine the trenches together forming a 3D nanostructure in a relatively wider area, although the pockets are not flat enough and the walls of the pockets are not straight enough. The reason of the wedge-shape is the poor settings of the overlap percentage under the setpoint force control mode. The area covered by the first vector will only be machined once but the adjacent area will be machined more than once under a certain setpoint force. The specific machining times of that area will determined by the overlap percentage. Because of these unavoidable machining characteristics, the pockets easily have wedge-shape walls.

(a)

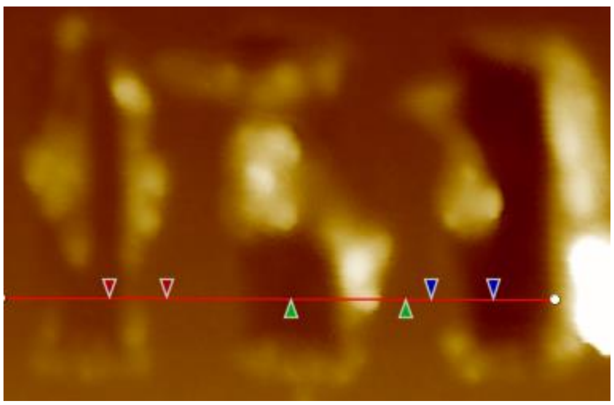

(b)

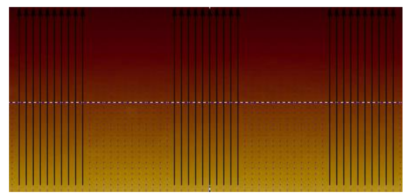

(c)

Cursor	ΔX(µm)	ΔY(nm)
Red	0.191	11.539
Green	0.378	25.407
Blue	0.202	-42.918

(d)

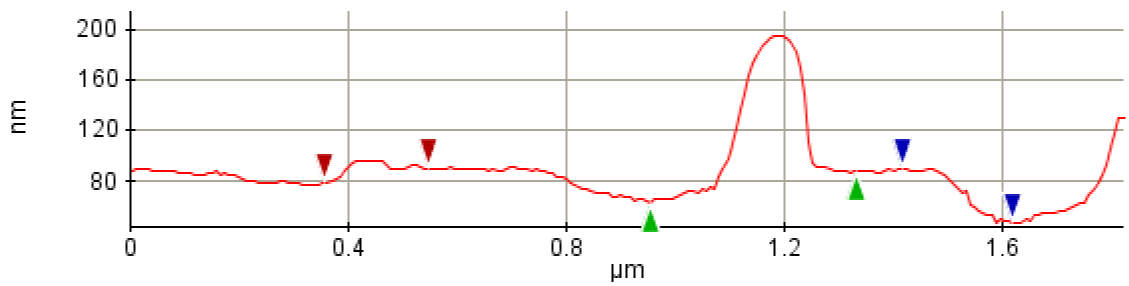

Figure 3.8 (a) Pockets on PMMA fabricated under setpoint force control mode with setpoint force values of 100, 150, 200 nN with 30 mV driving voltage of xy-vibration and 2 V driving voltage of z-vibration. (b) Vectors to form the pocket pattern. (c) Readings from (d) Cross-sectional profile of the pockets.

3.2.2 3D Nanomachining under Z-Height Control Mode

3D nanofabrication approach is also developed under z-height control mode. Similar to the 3D nanofabrication under the setpoint force control mode, 10 lines are combined to form a pocket pattern. The xy-vibration driving voltage is 30 mV. No z-vibration is applied. The designed depths are 35 nm, 20 nm and 10 nm from the left to the right. Figure 3.9 (a)

(a)

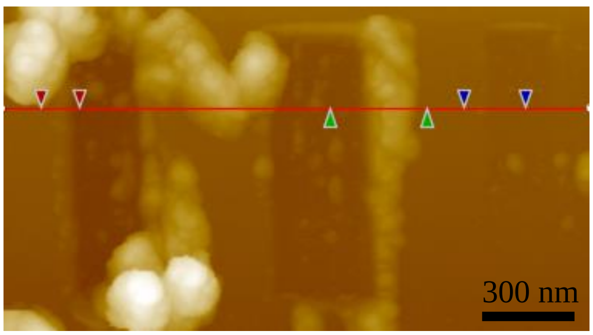

(b)

Cursor	ΔX(μm)	ΔY(nm)
Red	0.133	-31.045
Green	0.327	15.667
Blue	0.210	-6.250

(c)

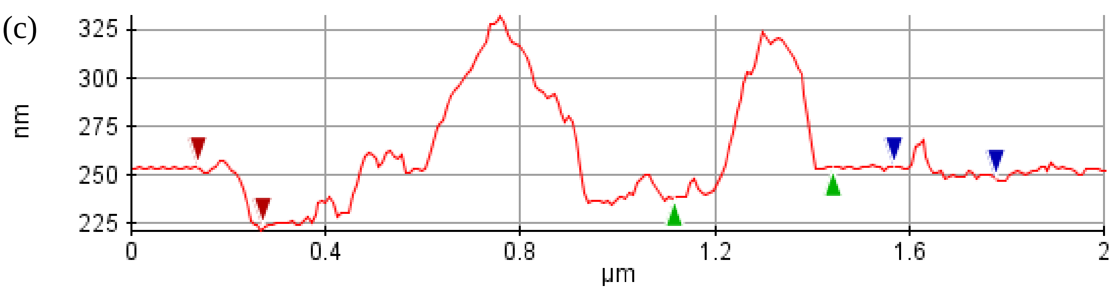

Figure 3.9 (a) Three pockets on PMMA fabricated under z-height control mode with design depth values of 10, 20, 35 nm. (b) Readings from (c) Cross-sectional profile.

shows the result after fabrication. The actual depth in each pocket from the top to the bottom is not uniform because of the sample was tilted a little upwards at the top. Tilting angle is close to zero laterally, however. Figure 3.9 (b) shows the reading values of the depths of three pockets. Figure 3.9 (c) shows the cross-sectional profile of the pockets after nanofabrication. From the profile, we can see that the bottom of each pocket is flatter than that fabricated under the setpoint force control mode. The wedge-like walls are largely caused by the shape of the AFM tip.

Another parameter that affects the 3D nanofabrication processes is the overlap percentage between two adjacent trenches. Figure 3.10 (b) shows 30 vectors representing

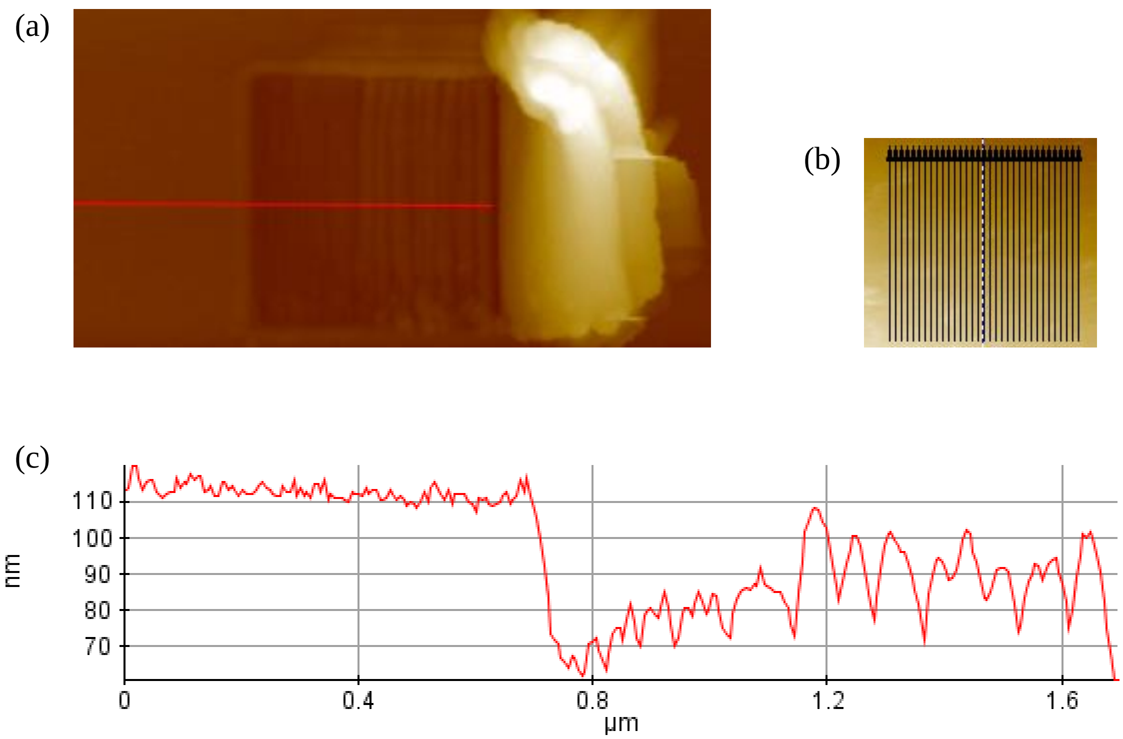

Figure 3.10 (a) A pocket pattern on PMMA fabricated under z-height control mode with 33 lines in total and 30 nm distance between adjacent two lines. (b) Vectors that form the pocket pattern (c) Cross-sectional profile of the pocket pattern.

machining trenches are combined together to form a 1 µm × 1 µm pocket with a relatively small overlap percentage of approximately 40%. Figure 3.10 (a) illustrates the result of the pocket after nanomachining process. The machining direction is following the vectors from the bottom to the top and from the left to the right. The debris is pushed toward right. From the cross-sectional profile, we can see that the overlap rate is too small that the surface is covered with ploughing patterns.

3.2.3 Characterization of the Nanomachining Process in Z-Height Control

In order to understand the nanomachining process, I investigated the practical nanomachining resolution of the xy-vibration in vector mode under z-height control.

I designed seven parallel single machining paths with decreasing pitch values. Theoretically, the minimum distance between two trenches with a certain depth is set by the diameter of the tip radius. For example, when using 30 mV xy-vibration and design 10 nm depth, the single machining width is about 100 nm. If the tip is blunt, two trenches designed too close will be overlap with each other. However, we do not know whether the machining process could achieve a practical high resolution or not with a certain xy-vibrational amplitude, although very small. The manufacturing of the AFM tip DLC190 announces that the radius of the tip is less than 15 nm. According to this, I designed seven machining paths for each of the following decreasing half pitch values, 40, 35, 30, and 25 nm, under 5 mV xy-vibration and 10 nm feature depth.

Figure 3.11 shows the results and the cross-sectional profiles of the trenches. In the figure, it is easy for us to identify seven clear trenches separated from each other. The results demonstrate that the machining resolution is at least 25 nm half-pitch when the xy-vibrational amplitude is 5 mV and the machining depths are 10 nm. This results also shows the flexibility of the nanomachining process. As mentioned before, the theoretical resolution is related with the actual AFM tip diameter without any xy-vibration. In order to fabricate 3D nanostructures, there is a tradeoff between the single trench width and the machining efficiency. The higher the resolution, the longer time it takes to finish machining a 3D nanostructure.

(a)

(b)

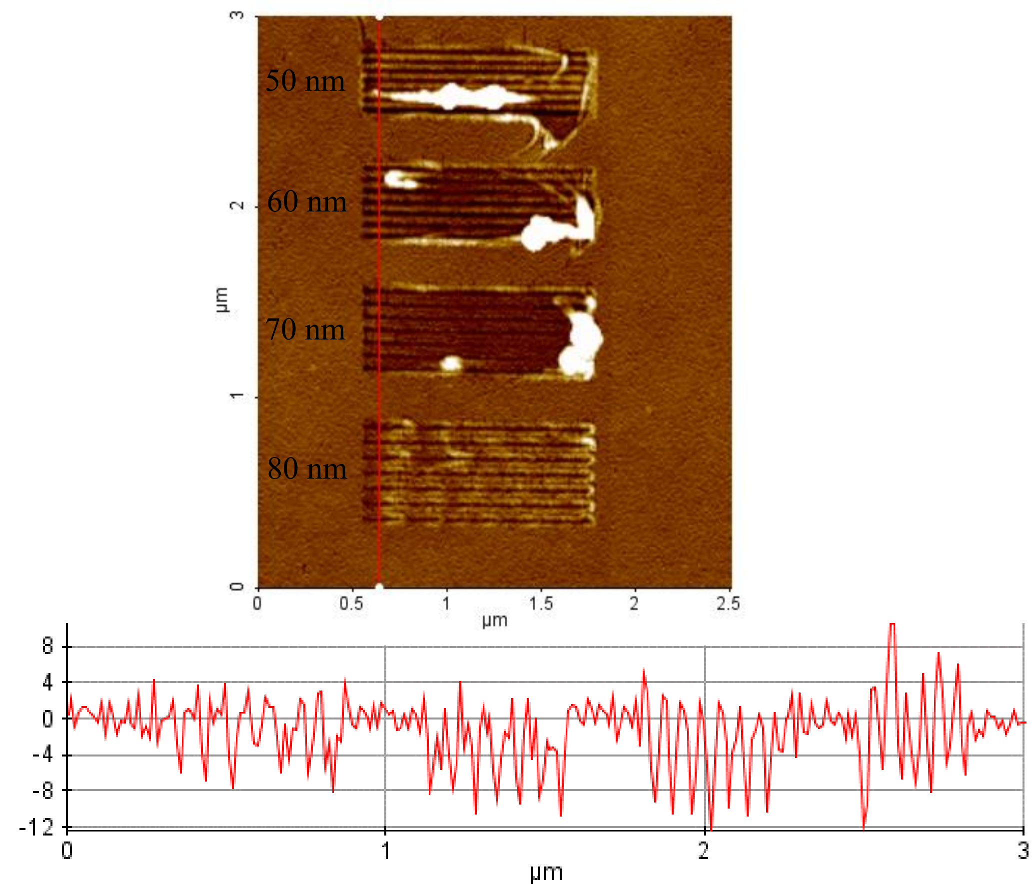

Figure 3.11 (a) AFM image and (b) cross-sectional profile of four sets of trenches with decreasing pitch values from 80 nm to 50 nm. Each of the set includes seven trenches.

Besides the characterization of xy in-plane vibration, I also investigated the characteristics of the ultrasonic vibration assisted nanomachining process in z-height control by three sets of experiments. The first set investigates the effect of ultrasonic z-vibrational amplitude on feature depths of nanostructures. The second set of experiments explores the relationship between the feature depth and the assigned base depth under a fixed amplitude of z-vibration. The third set of experiments explores the relationship between the feature depth and the machining speed.

For the first set of experiments (investigating the effect of ultrasonic z-vibrational amplitude on feature depths of nanostructures), I designed five pockets with assigned base depths of 20 nm using different z-vibrational amplitudes, 1.5, 2, 2.5, 3 and 3.5V. Machining speed is set as 0.5 µm/s. The reason to machine pockets are as follows. First, pockets are considered as a basic component of 3D nanostructures since we are able to fabricate a 3D nanostructure using layer-by-layer technique. Moreover, the feature depth measurement is more accurate that single trenches. After experiments, I measured each pocket five times to get average feature depths. The measurement data, the calculated mean, standard deviation (SD), median absolute deviation (MAD), and coefficient of variance (CV) are shown in Table 3.3.

Table 3.3 Final pocket depths under different amplitudes of z-vibration

Z-amplitude (V)	1.5	2.0	2.5	3.0	3.5
Meas. 1 (nm)	14.9	23.4	38.3	57.8	85.8
Meas. 2 (nm)	12.8	25.4	38.5	59.3	84.4
Meas. 3 (nm)	14.7	26.7	39.9	60.0	83.6
Meas. 4 (nm)	15.0	23.4	41.3	60.0	87.5
Meas. 5 (nm)	13.8	25.9	39.5	64.9	88.8

Table 3.3 Continued

Mean (nm)	14.2	25.0	39.5	60.4	86.0
SD (nm)	0.9	1.5	1.2	2.7	2.1
MAD (nm)	0.3	1.3	1	0.7	1.7
CV	7%	6%	3%	4%	2%

The result shows that the actual pocket depths increase with the amplitude of ultrasonic z-vibration. The standard deviation and the median absolute deviation values are fluctuating up and down. But the coefficient of variance is decreasing from 7% to 2%. It shows that the machining process has smaller relative dispersion when increasing the z-vibrational amplitudes. The machining process is stable even with large feature depth. The relationship between the actual depths and the amplitude of z-vibration is plotted in Figure 3.11.

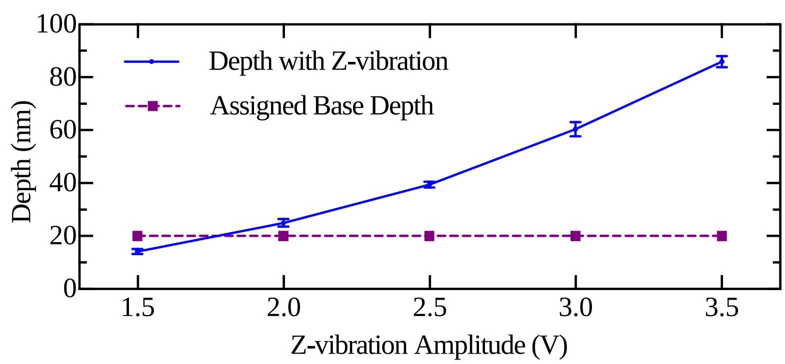

Figure 3.12 Relationship between the final depth and the assigned base depth of pockets when machining speed is set as 0.5 μm/s. Feature depths increase as z-vibrational amplitudes increase from 1.5 V to 3.5 V

The mean depth values of fabricated pockets under increasing z-vibrational amplitudes are 14.2, 25.0, 39.5, 60.4, and 86.0 nm, with standard deviations of 0.9, 1.5, 1.2, 2.7, and 2.1 nm, respectively. These experimental results demonstrate the function of the ultrasonic z-vibration, which is dynamically "freezing" the cantilever. Because of this, the z-vibration helps the AFM tip penetrate into samples. The larger the z-vibrational amplitude, the deeper the penetration, resulting in larger feature depths. However, if the amplitude of ultrasonic z-vibration is not large enough (approximately 1.8V in this case), feature depths will not reach the assigned base depth, meaning that the compliance of the tip is still playing a large ole.

The second set of experiments is designed to explore the relationship between feature depths and assigned base depths with a fixed amplitude of z-vibration. I designed six pocket patterns with increasing design depth to compare the differences. The machining speed is set as 0.5 µm/s for consistency. The amplitude of z-vibration is set as 2.5 V in this set of experiments. Assigned base depths of six pockets are set as 10, 20, 30, 40, 50, and 60 nm. After nanomachining with the help of ultrasonic z-vibration (2.5 V), the mean values of the actual depths are measured as 26.3, 37.6, 45.0, 58.5, 69.4, and 79.4 nm, with standard deviations of 1.6, 2.6, 0.8, 2.7, 2.6, and 1.2 nm. The median absolute deviations are 1, 2.5, 0.1, 0.5, 0.8 and 0.2 nm, as shown in Table 3.4. I measured each pocket five times to get final feature depths.

Table 3.4 Results of pocket depths under different assigned base depths

	1	2	3	4	5	6
Assigned Base Depth (nm)	10.0	20.0	30.0	40.0	50.0	60.0
Meas. 1 (nm)	27.0	41.5	44.8	59.2	69.2	80.7

Table 3.4 Continued

Meas. 2 (nm)	25.3	38.2	44.8	58.8	70.5	77.4
Meas. 3 (nm)	28.0	35.3	46.2	61.9	71.0	79.5
Meas. 4 (nm)	24.1	37.8	44.1	54.5	65.0	79.7
Meas. 5 (nm)	27.1	35.2	44.9	58.3	71.3	79.7
Mean (nm)	26.3	37.6	45.0	58.5	69.4	79.4
SD (nm)	1.6	2.6	0.8	2.7	2.6	1.2
MAD (nm)	1	2.5	0.1	0.5	0.8	0.2
CV	6%	7%	2%	5%	4%	2%

The result shows that with a z-vibrational amplitude of 2.5V there is a constant difference between the feature depth and the assigned base depth. The SD, MAD and CV are fluctuating within a reasonable range, indicating the process is stable. The largest standard deviation of the mean is only 7%. The relationship between the actual depths and the amplitude of z-vibration is plotted in Figure 3.12.

This constant increased depth value is determined by the amplitude of z-vibration. According to the previous results shown in Figure 3.11, the actual depths should be 19.5 nm deeper than designed depth with a small amount of variation, if the amplitude of z-vibration is set as 2.5 V. From the Figure 3.12, actual feature depths are the summation of the assigned base depth and the depth increased by z-vibration (Δd) under a certain level of amplitude. The mean added depth (Δd) in this set of experiments here is 17.7 nm with a standard deviation of

1.79 nm, which is comparable with the result in the first set of experiments when the z-vibrational amplitude is set as 2.5 V.

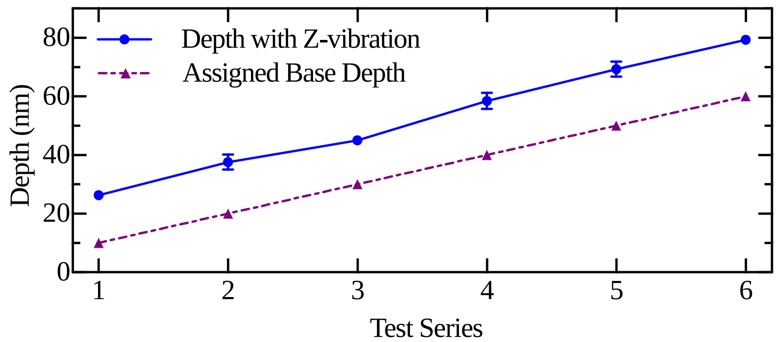

Figure 3.13 Relationship between the actual depth and the assigned base depth when z-vibrational amplitude is 2.5 V and machining speed is 0.5 μm/s. When designed depths increases from 10 to 60 nm, actual depths increases from 26.3 to 79.4 nm. The increased depth values have a mean of 17.7 nm and standard deviation of 1.79 nm

The third set of experiments is designed to explore the relationship between the feature depth and the machining speed. The reason I explore this relationship is that the z-height control during the nanomachining process is not a closed loop control as in traditional CNC machining. Therefore, there is a chance that the final feature depths are actually affected by the machining speed.

I designed five pockets for this set of experiments. Each of them is composed of five machining paths with a same overlap rate larger than 60%. The five machining speeds are 0.1, 0.5, 1, 2, and 5 μm/s. The assigned base depth is 10 nm and the amplitude of ultrasonic z-vibration is set as 2.5 V. After experiments, I measured each pocket four times to get average final feature depths. The actual depths are 29.2, 26.1, 24.8, 22.4, and 16.5 nm, with standard deviation of 0.9, 1.1, 1.7, 1.6 and 2.6 nm respectively, as shown in Table 3.5.

Table 3.5 Results of pocket depths under different machining speeds

	1	2	3	4	5
Speed (µm/s)	0.1	0.5	1	2	5
Meas. 1 (nm)	29.3	27.6	26.9	24.1	14.1
Meas. 2 (nm)	30.3	25.2	23.6	22.9	14.5
Meas. 3 (nm)	28.5	25.5	25.4	20.4	18
Meas. 4 (nm)	28.5	26	23.4	22.1	19.3
Mean (nm)	29.2	26.1	24.8	22.4	16.5
SD (nm)	0.9	1.1	1.7	1.6	2.6
MAD (nm)	0.4	0.4	1	1	1.95
CV	3%	4%	7%	7%	16%

The result shows that under a set z-vibrational amplitude (2.5 V) and assigned base depth (10 nm), the final feature depth decreases as the machining speed increases. The SD, MAD and CV consistently shows an increasing value, indicating that the process is becoming more and more unstable when the machining speed is high. But we still need to notice that the machining speed up to 2 µm/s still has low deviations. The relationship between the actual feature depth and the machining speed is plotted in Figure 3.13.

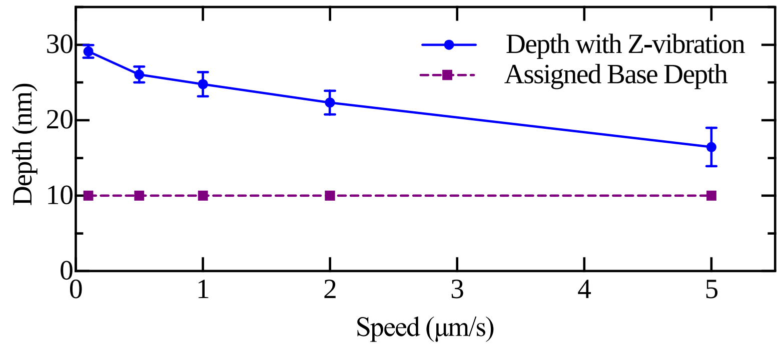

Figure 3.14 Relationship between the actual feature depth and the machining speed when z-vibrational amplitude is set as 2.5 V and the assigned base depths are set as 10 nm for all five pockets. When machining speeds increase from 0.1, to 5 µm/s, feature depths decrease non-linearly, and the variations increase as machining speed increase overall.

The overall relationship is non-linear. However, as the machining speed increases from 0.1 to 0.5 µm/s, the actual depths decrease faster than that of the rest. After 0.5 µm/s, the actual depth decreases in a linear way that when the speed increases 1 µm/s, the depth decreases 2.1 nm. The R^2 of the linear approximation of the last four speed is 0.997. The reason of this relationship is that the machining tool is a free end cantilever, which is not rigidly maintained by close loop control as used in traditional CNC machining processes. However, the decrease of feature depths from 0.5 µm/s to 2 µm/s is not significant, less than 4 nm. That means the machining process is reasonably stable over a large portion of the machining speed range generally used. In practice we can get the characteristics of the process after fixing the machining speed. Overall, the standard deviation of the feature depth increases with the machining speed, which means faster machining speed brings in more uncertainty into the process. Therefore, there is a trade-off between the feature depth precision and fabrication time when choosing machining speed.

Throughout all of the three sets of characterization experiments, results show that the feature depth is the summation of the assigned base depth and the depth change (Δd) associated with the amplitude of the z-vibration. After maintaining a certain machining speed and a certain level of z-vibration, we can characterize the depth change (Δd) and thus able to get desired feature depths by interpolating the characterization results.

3.2.4 Cleaning and Reimaging the Sample after 3D Nanomachining Process

It is a necessary and important step in the 3D nanofabrication process. After nanomachining, debris came out of the surfaces of 3D nanostructures cover the results. It is impossible to get the dimensional information of 3D nanostructures without cleaning the sample. Therefore, the debris have to be removed and cleaned to check the dimensions of 3D nanostructures. I developed a process to remove the debris efficiently and effectively.

The cleaning procedures are as follows. 1) prepare samples covered with a PVA layer (7-15 nm thickness is a good range); 2) after finishing the nanomachining process, peel off the sample from the nanovibrator; 3) fill PVA saturated 99.99% ethanol into a syringe with a 250 um (0.0098”) inner diameter needle; 4) flux the sample by perpendicularly placing the needle close to the sample surface, and pressing the syringe as hard as possible; 5) after the high flow rate fluxing process is finished, immediately put the sample into a ultrasonic bathing using 30% wt acetone aqueous solution; 6) wash the sample with 99.99% ethanol for 10 s to clean residual acetone chemicals, which does not require high pressure and flow rate; and 7) bake the sample on 70 degree Celsius hot plate for 1min.

The PVA water solution is prepared by dissolving the solid powder in the DI water. For the 0.5% PVA water solution, put 0.25 g PVA powder in a conical centrifuge tube, and fill it with DI water to 50 mL. Then put the tube in 80 °C oven for about 24 hours until no solid PVA at the bottom of the tube. Until now, the PVA solution is ready for spin coating. After spin coating, the sample is placed on a 90 °C hot plate for 90 seconds to remove the residual DI water solvent.

The PVA solid powder was purchased from ALDRICH, 363146-25G, with molecular weight of 85,000-124,000. The syringe used is Micro-Mate interchangeable glass 1/5 cc syringes with 1/5 cc graduations. The 0.0098" (250 μm) inner diameter needle used is from IntelliSpense.

As for the water-soluble material chosen as the sacrificial layer that spin-coated on the PMMA surfaces, it is important to have the characteristic of uniform coating on the PMMA surface using water as solvent. Organic solvent cannot be used as the solvent of water-soluble chemical since the solvent will dissolve the PMMA layer, which makes no polymer covering on silicon surfaces. Another important characteristic is that the water-soluble material should not solve in water too quick, since it takes time for the ultrasonic bathing really have an impact on dislocating the debris. PEO and PVA are two materials I have tried to coat on PMMA surfaces. PEO is not able to form a uniform layer on PMMA surfaces as shown in Figure 3.14. The non-uniformly coating makes the sample with a layer of uncontrollable thickness and large variance. PVA DI water solution, as an alternative material, can reliably be coated on PMMA layer with relatively uniform thickness. Figure 3.14 (a) and (b) shows the PEO and PVA coating on the PMMA film, respectively. It demonstrates that the PVA has better uniformity than PEO coating. The area covered by the red circle on the picture is magnified in Figure 3.14 (c). Figure 3.14 (d) shows the original PMMA sample, on which we can see a yellowish color reflected from the PMMA layer without the PVA covering. In order to measure the thickness of the PVA layer, the edge is measured in AFM to get the height difference between the PVA covered PMMA and original PMMA.

Figure 3.15 shows the thickness measurement of the PVA film using 0.5% PVA DI water solution spin-coated on PMMA with 3000 RPM. I calibrated the thicknesses of PVA layers by measured the height difference between the boundary of PVA-coated and PVA-washed area in AFM by dissolving part of the PVA layer by DI water. If 1% PVA water solution is used, the thickness of the PVA layer is larger than 30 nm thickness under 3000 rpm spinning speed. If 0.5% PVA water solution is used, the thickness of the PVA layer is about 15-20 nm thickness under 3000 rpm spinning speed. But if 0.5% PVA water solution is used, the thickness of the PVA layer is about 7-15 nm thickness under 4000 rpm spinning speed. Therefore, depends on the application, the thickness of PVA layer on PMMA is tunable. Usually, I use 15-20 nm PMMA layer.

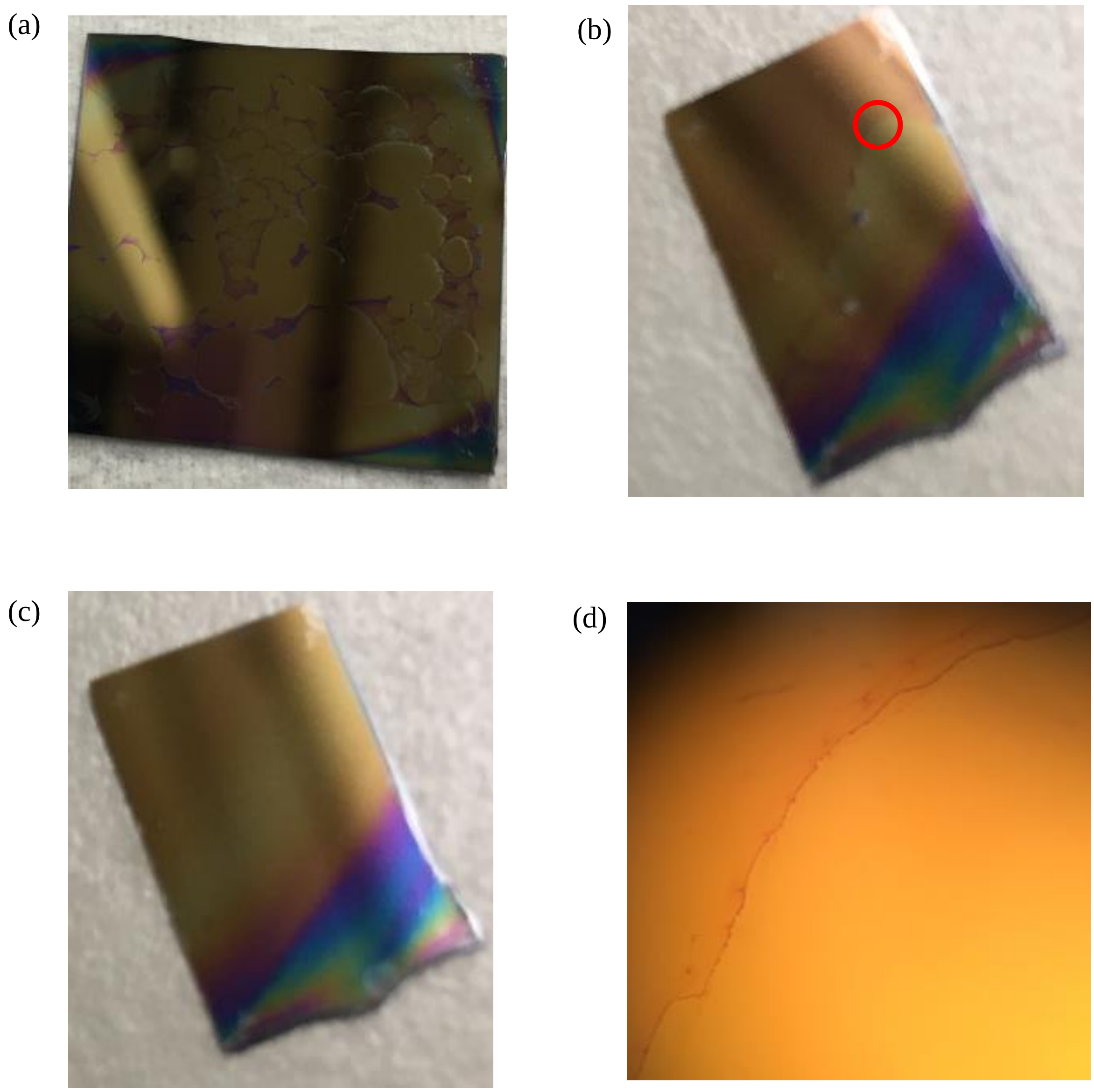

Figure 3.15 (a) PEO coated PMMA film sample. The result shows that the PEO DI water solution could not uniformly coated on the PMMA sample surfaces. (b) PVA coated on PMMA sample. (c) Original PMMA sample without PVA layer. (d) The magnified area circled in (b). It shows an area partially covered by a PVA layer.

(a)

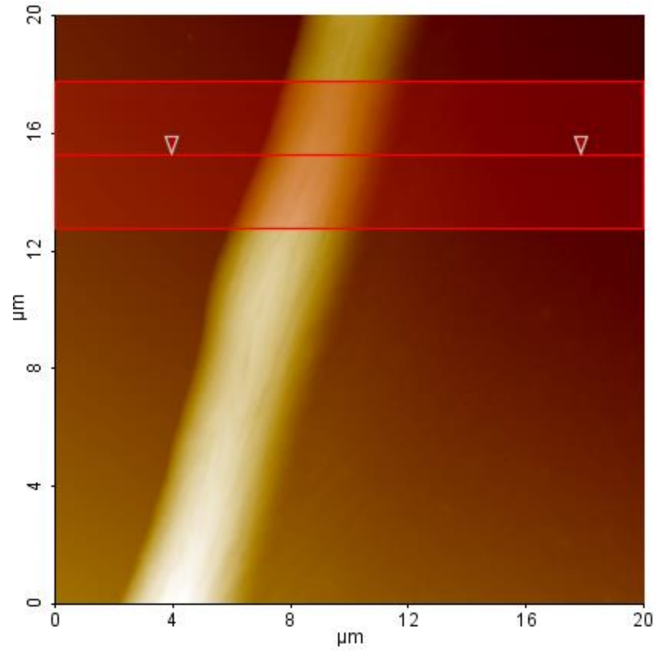

(b)

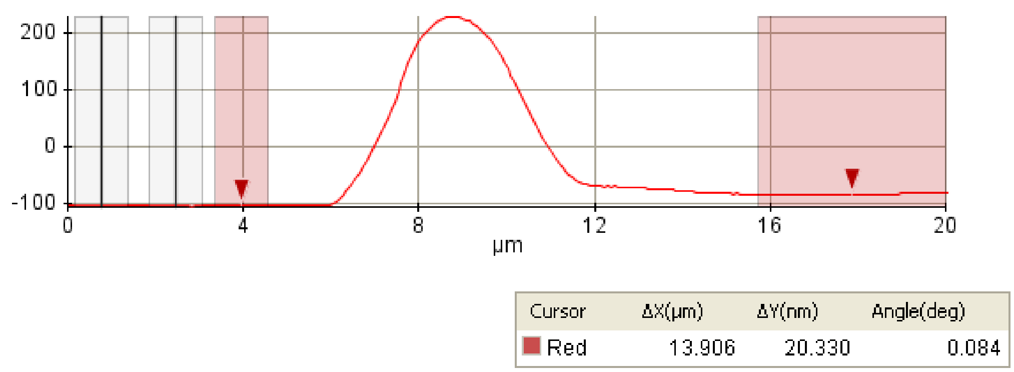

Figure 3.16 (a) is an AFM image of an area partially covered by a thin layer of PVA. (b) The cross sectional profile of the thickness measurement. The thickness here is 20 nm.

The third step is to fill a syringe with a 250-μm diameter needle with PVA saturated 99.99% ethanol. The reason of using PVA saturated ethanol is to fully utilize the ethanol flow to “push away” debris without dissolving the PVA layer. PVA is slightly soluble in ethanol but not soluble in other organic solvent like acetone. About 10^6 volume of ethanol can solve 1 volume of PVA [158]. In the thickness measurement, assuming 20 nm PVA on 6×6 mm^2 sample. PVA volume is 720×10^{-6} mm^3. So ethanol with only a volume of 720 mm^3 (0.72 cc) can solve the PVA film. I demonstrated this calculation by fluxing the PVA coated sample with 5cc 99.99% ethanol. The PVA layer was dissolved.

The capability of “pushing away” debris is shown in Figure 3.16. A 3D nanostructure is fabricated on PMMA surface, which penetrated through the PVA water soluble layer on the PMMA. Figure 3.16 (a) shows the result right after the 3D nanomachining process before implementing the fluxing process. We can clearly see the debris accumulated around the pattern. The fluxing direction is indicated on the plot. Figure 3.16 (b) shows the result of using 99.99% ethanol other than PVA saturated 99.99% ethanol. Comparing these two plots, we can see the function of the water soluble layer and the capability of fluxing. The left and upper edge of the pattern is effectively cleaned with the help of fluxing and PVA layer. However, the bottom right debris are pushed towards the center of the pattern. This set of results show the “pushing away” capability of the fluxing process.

In the fluxing process, the flow rate and liquid pressure applied on debris played an essential role. The diameter of the needle is chosen as 250 μm as an experimental result. I have tried a needle with 50 μm opening diameter, which has a weaker fluid pressure and flow rate if the same force applied on the piston. Weak fluid flow cannot flux away the accumulated debris.

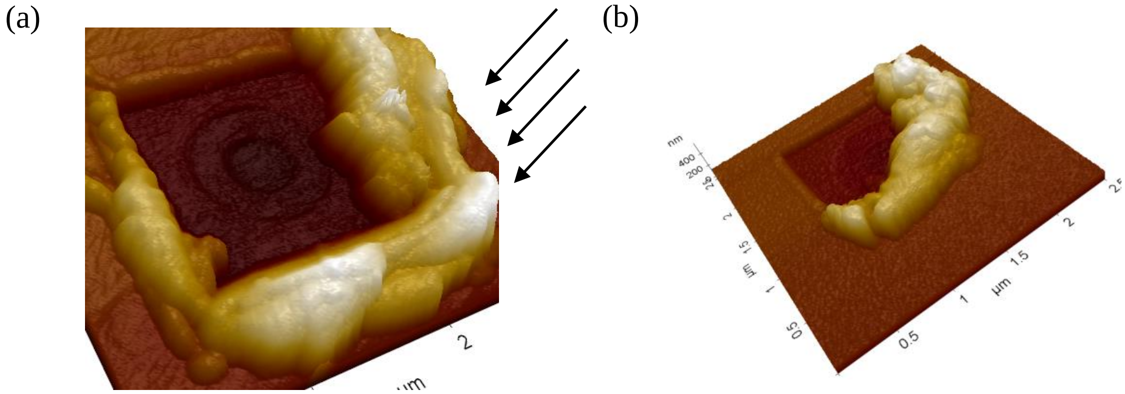

Figure 3.17 (a) 3D nanostructure right after nanomachining. (b) The same pattern after fluxing in the direction indicating on (a), which is about 45° incident angle between the syringe and the sample.

The fourth step is fluxing the sample by perpendicularly placing the needle to the sample surface, and pressing the syringe as hard as possible as shown in Figure 3.17 (a). After squeezing out all the PVA saturated ethanol in the syringe. It came to the fifth step of ultrasonic bathing is shown in Figure 3.17 (b). The sample is immediately moved to the 30% wt aqueous acetone for 2min ultrasonic bathing. These two steps should be executed in consequence immediately to ensure the functionality of the water-soluble layer and the fluxing. Figure 3.17 (a) shows the preparation before pushing the piston and generating the high flow rate ethanol.

The needle is close to the sample. The sample surface is perpendicular to the ground and the syringe is parallel to the ground and perpendicular to the sample surface.

(a)

(b)

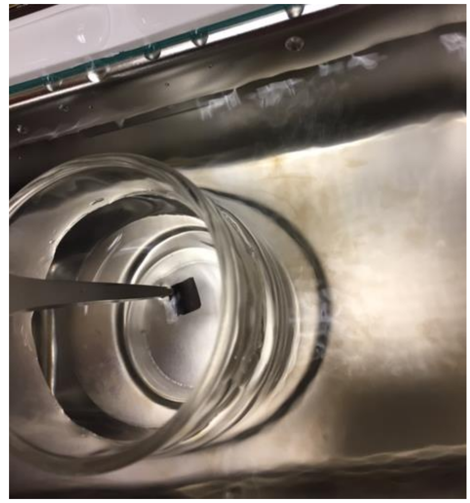

Figure 3.18 (a) Preparation for the high flow rate fluxing. The sample surface is perpendicular to the ground and the syringe is parallel to the ground. (b) After fluxing, the sample is immediately moved to the 30% wt aqueous acetone for 2min ultrasonic bathing.

The concentration of the aqueous solution of acetone is critical in the process. If it is too high, such as pure acetone, the whole PMMA film is solved immediately in the acetone or acetone solution. But if it is too low, extension of ultrasonic agitation does not help to remove the debris that cover on the nanostructures. The 30% wt aqueous solution of acetone is suitable for removing debris while not damaging machined features after carefully calibration.

After cleaning process, the sample needs to be aligned with the original direction in order to implement the reimaging procedures easily. The procedures of alignment are as follows. First, scratching two reference trenches perpendicular to each other using a tweezer. Second, after the nanofabrication process, getting the screenshot of the reference trenches as well as the locations of the pattern using a screen ruler. Third, fixing the cleaned sample back to the top of the nanovibrator, making sure that the orientation of the samples are the same with the original one. The screenshot can be used in this procedure. Finally, imaging a relative larger area with a low resolution to get a rough location of the cleaned pattern. And imaging the final pattern again with a reasonable size and resolution.

3.2.5 Overall Procedures of the Developed 3D Nanofabrication

The procedures of the 3D nanofabrication on PMMA film includes six steps as follows. 1) image a clean area under contact mode; 2) design patterns or loading bitmap images for the structure to be machined; 3) select constant height control mode for AFM in nanolithography software and import the image acquired from the first step in the lithography software as the reference background; 4) applying ultrasonic vibration assisted nanomachining processes for the designed patterns; 5) clean the sample with the aforementioned process; and 6) reimage the 3D nanostructures as mentioned previously. The cleaning process is necessary in order to remove the debris from the machining process and achieve clear and accurate results. After fabricating 3D nanostructures on PMMA films using ultrasonic vibration assisted nanomachining process, other techniques, such as RIE process and nanoimprint lithography techniques, can be utilized to transfer 3D nanostructures from PMMA surfaces onto a silicon substrate and on other materials. For RIE, Semigroup RIE system is used in our experiments to obtain 3D nanostructure on silicon substrate. Results and etching recipe are shown in Chapter 4. For 3D nanomolding and nanoimprint, the result is shown in Chapter 5.

3.3 Chapter Summary

This chapter describes the experimental setup of the 3D nanofabrication process. Schematics of the system and details of the components are discussed. Based on the experimental setup and the function of it, 3D nanofabrication processes are developed under setpoint force control mode and z-height control mode. After that, cleaning and reimaging processes are defined. Finally, the overall procedures of the fabrication processes are listed and explained.

CHAPTER 4 FABRICATION AND TRANSFER OF 3D NANOSTRUCTURES

4.1 3D Nanostructures fabricated under Setpoint Force Control

From the previous pilot experiments, it is possible to fabricate 3D nanostructures since the depths of machining paths are able to be regulated. From previous results of our research group, machining trench depths increase with the setpoint forces applying on the sample surfaces [19]. In order to control the depths, various setpoint forces are used to achieve different depths. Besides the setpoint force, other related parameters are also tuned to optimize the 3D nanomachining process. 3D nanostructures are fabricated in both vector mode and raster scan mode.

4.1.1 Design of Patterns in Vector and Raster Scan Modes

Prior to the 3D nanomachining process, patterns are needed to be designed by users and are recognized by the AFM-based nanomachining system. There are two ways to design system recognizable patterns. The first one is combining vectors together to form a pattern. The depths of pattern formed by combined vectors are achieved by setting the setpoint force values for each vector. The second is using bitmap images in grayscale. Complex geometry can be easily designed in this way and the depths are controlled by simply designating the grayscale of the corresponding part in the pattern. These two approaches of designing patterns represent two ways to define the feature geometry in xy-plane, implemented in two lithography-working modes: vector mode and raster scan modes.

In vector mode, dots, lines, rectangles, ellipses, polygons and polylines are six basic vectors for users to design and combine together, as shown in Figure 4.1. Figure 4.1 (b) shows the theoretical results after nanofabrication process. The xy-vibration is able to enlarge the widths of machining paths to about 100 nm, which gives a quantitative basis to design distances between two lines to achieve an overlap between machining paths. Combining and aligning designed vectors can make sure that the whole area can be covered by machining paths.

(a) (b)

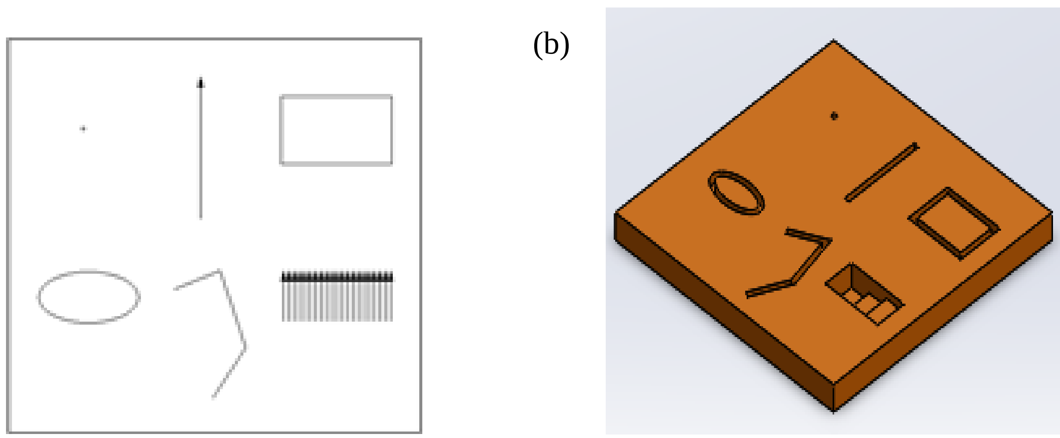

Figure 4.1 (a) Patterns designed in vector mode with an example of a three layers 3D nanostructure. (b) Theoretical results after fabrication in vector mode.

Distances between each two adjacent lines needs to be controlled after considering the width of trench resulting from each line (from virtual tool diameter) and the overlap percentage between adjacent lines. The width of each line is determined by the diameter of the virtual tool, which is equal to the sumof the tip diameter and the xy-vibration amplitude, and can be characterization experimentally. Overlap percentage is related to the radial depth of cut, and will affect the surface finish of the final features. A large overlap percentage (for example, 80% overlap percentage) results in a small radial depth of cut, which in general produces smoother part surface. But it takes longer to finish the whole structure.

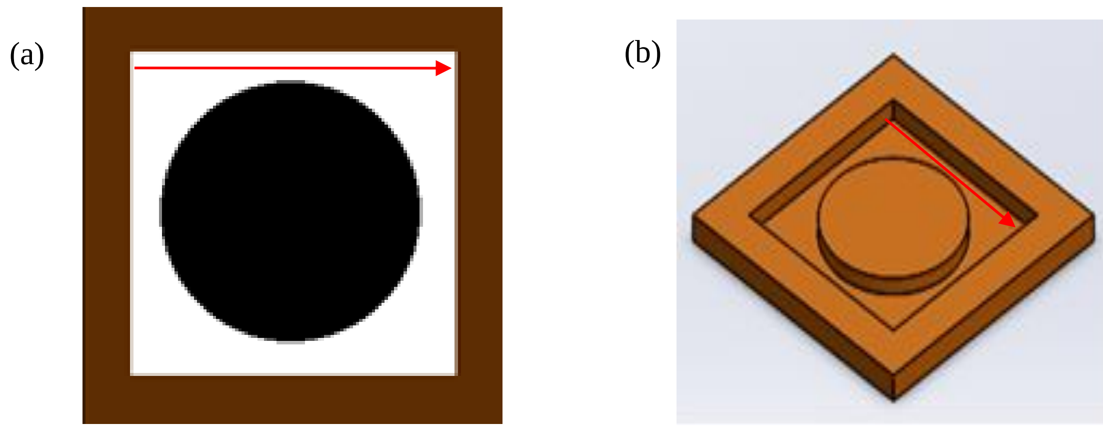

Figure 4.2 (a) Schematic of fabricating a 3D nanostructure in raster scan mode with a protruding circle represented by gray scale bitmap image. Red line shows the scan direction. (b) Theoretical result after fabrication in raster scan mode. Red line shows the scan direction.

In raster scan mode, the desired features are depicted in grayscale bitmap images. The grayscale of the image represent the setpoint force values during nanomachining processes. The brightest area (white color) has the largest setpoint force, while the darkest area (black color) is loaded with the smallest setpoint force. The force values of other areas with gray colors are linearly interpolated by gray scale values between the two extreme force values. Figure 4.2 (a) illustrates the schematic of fabricating a 3D nanostructure in raster scan mode with a protruding circle represented by gray scale bitmap image. The red line shows the scan direction. After fabrication, theoretical result in raster scan mode is shown in Figure 4.2 (b).

The tool paths in the nanomachining process start from the upper left corner laterally to the right side pixel-by-pixel in bitmap images. After finishing one line, the AFM tip lifts up and moves to the beginning of the second line, which is the left side of the path. Then the AFM tip indents into the sample and starts the second nanomachining path. The total number of paths of the entire nanomachining process is determined by the number of pixels of the grayscale bitmap image. The pixel number in row as an input parameter is set to control the number of machining paths since the lateral direction is the only fabrication direction under this mode. The pixel number in column determine the in-plane resolution of the setpoint force changing position. The entire machining process ends at the bottom-right corner of the bitmap image.

The designed patterns need to be recognized by AFM nanolithography software. The users' interface is shown in Figure 4.3. Under setpoint force control mode, desired patterns are designed (patterns created by combining vectors) or imported (patterns depicted by grayscale bitmap images) into the nanolithography software. Figure 4.3 shows a two layers concave nanostructure with 60 pixels in row and 60 pixels in column. Usually, the AFM is used as a metrology tool for nanoscale imaging. When used for nanolithography, the AFM first scans an image on the selected area as the workspace for future lithography tasks. The background image is the surface topographic image acquired from contact mode providing a reference surfaces for the machining process. And nanolithography functions can be activated for feature fabrication by choosing different working modes, designing objects, selecting force values and machining speed. The "ScanRate" is the machining speed during nanofabrication processes.

“Servo” is on representing the force feedback control is on. The values of “Begin (Min) nN” and “End (Max) nN” are the max and min values of setpoint forces. Under the control of the lithographic software, the AFM tip follows the vector-based trajectory (i.e. toolpath) one by one according to the specified sequence until all of them are machined, either in the vector mode or the raster scan mode.

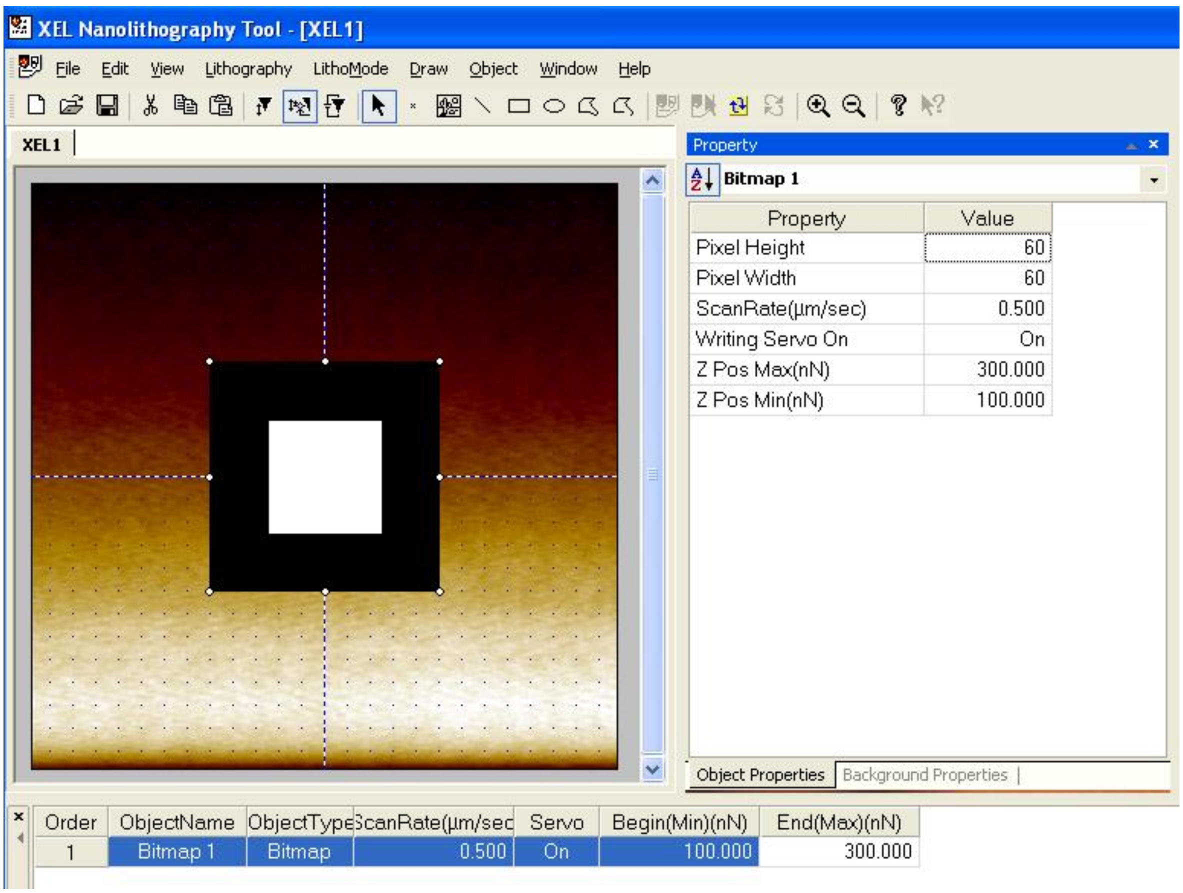

Figure 4.3 Setpoint force control mode nanolithography parameter control interface.

4.1.2 3D Nanofabrication Process and Results

After implementing the 3D nanofabrication process using ultrasonic vibration assisted nanomachining, 3D nanostructures can be successfully fabricated in both vector mode and the raster scan mode.

In the vector mode, in order to fabricate multi-level stair-like nanostructures, a number of parallel lines are designed for each layer to remove material at each specific height level, as shown in Figure 4.4 (e). Lines are arranged from the left to the right and distributed uniformly. In the experiments, three layers of patterns were designed, each of which is composed by a set of parallel vector lines. The feature contains 30 lines for the first layer, 20 lines for the second layer and 10 lines for the third layer, with the line spacing of 50 nm. After characterizing the diameter of virtual tool experimentally when the driving voltage of xy-vibration is 30mV, we know the diameter of virtual tool is around 100nm at the trench depth of 10 nm. The distance between every two adjacent lines is set as 50 nm. A 50% overlap percentage was selected to achieve reasonable surface finish. During the nanomachining process, AFM tip follows the prescribed lines one by one same to the designed sequence. When the tip makes transitions between lines, the interaction force applied on the sample is the background force (1 nN) set by the user that would not machine the PMMA. Besides the overlap percentage and setpoint force, other parameters like the machining speed and amplitude of z-vibration also affect the fabrication results of the nanostructure. In experiments, 1 μm/s machining speed is chosen, which corresponds to 0.5 nm feed per xy-vibrational rotation and 3 V driving voltage applying on z-piezo to help achieve a certain depth.

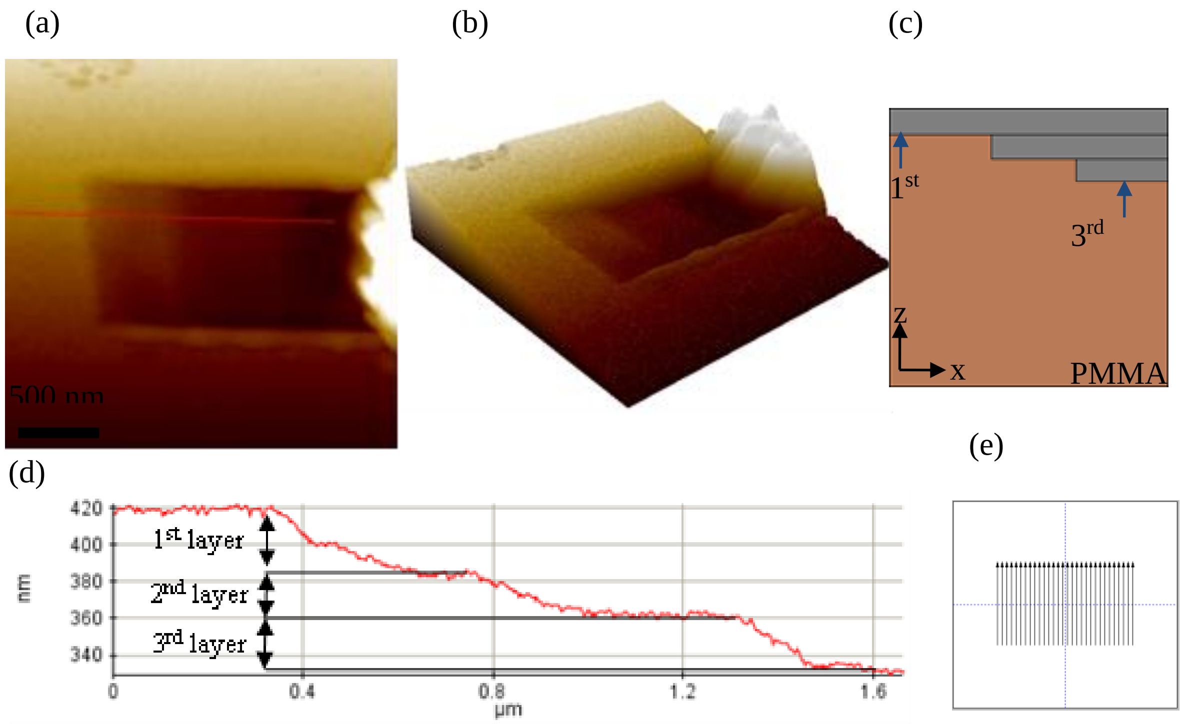

Figure 4.4 (a) AFM image of a three-level nanostructure fabricated in vector mode. (b) 3D view of this nanostructure. (c) Schematic 3D nanofabrication process of a three-level nanostructure in vector mode fabricated layer-by-layer. (d) Cross sectional profile of this three-level nanostructure. (e) Designed patterns in vector lines (toolpath).

3D nanostructures were fabricated using layer-by-layer nanomachining method in the vector mode. The overall size of the pattern is 1.5 µm × 1 µm, which has three steps with 0.5 um width for each. The fabrication procedures are shown as follows (Figure 4.4 (c)): Machining the first layer with (the driving voltage of xy-vibration is 30 mV with the resulting diameter of virtual tool is around 100 nm); after that, machining the area covered by vectors which indicating the second layer of the pattern; repeating procedures mentioned above until all the layers are finished. After machining each layer, samples can either be inspected after finishing each layer or after finishing the entire 3D nanostructure. Figure 4.4 (e) shows machining tool paths for the pattern, which is a set of parallel lines corresponding to the traces of AFM tip.

The setpoint force was 50 nN and the machining speed was set as 1 μm/s. The overlap percentage is 50% and the driving voltage for xy-vibration was 30 mV and for z-vibration was 0.5 V. The fabricated three-level nanostructure in vector mode is shown in Figure 4.4 (a). Figure 4.4 (b) shows the 3D view of the result. The result from Figure 4.4 (d) clearly shows three steps with the depths of each level at 35 nm, 23nm and 27 nm respectively. Depth of the first layer is what had shown in the calibration process before fabrication. However, depths of the second and the third layer are a little less than that of the first one. This may be caused by the interaction between the AFM tip and the debris when the second layer was machined, which prevented desired depths in results.

The nanomachining process in vector mode can create sparse patterns with high efficiency. Prescribed sparse patterns can be fabricated without scanning through all the areas as in the raster scan mode. All the users need to do is to put vectors in desired locations. It is too difficult, however, to design complex 3D nanostructures in this vector mode, since all the vectors are required to be arranged and combined manually. For example, the staircase structure can be designed by arranging parallel vectors together, which is not that difficult. But designing a circle or other irregular features are too complicated and time-consuming. Therefore, we continue to investigate 3D nanofabrication process in raster scan mode.

In raster scan mode, pattern are designed in the form of bitmap images whose depths are controlled by the gray scale value, representing corresponding setpoint force at each pixel.

As for the feature replication, it is necessary to calibrate amplitude of xy-vibration carefully in order to obtain a desired pixel dimension in the bitmap image. In experiments, the overlap percentage between two adjacent pixels need to be around 80% to achieve structures with good uniformity and surface finish. The overlap percentage requirement is larger than that in the vector mode. The difference is mainly caused by the perpendicular machining directions when machining using vectors with directions along the cantilever and bitmap image. In vector mode, previous three layer staircase structure is designed by combining vectors pointing from bottom to the top, which is the direction along the length direction of the cantilever. In the raster scan mode, the cantilever can only scanned in the lateral direction, which has a lower stiffness due to torsional motion of the cantilever.

The layer-by-layer machining process is trying to keep the setpoint force constantly to get features with same depths for each layer. The feature on each layer is machined by the constant force, which makes it easy to control the process and the resulting depths of features. The limitations, however, of machining features layer-by-layer are its repetitive machining and low speed. More than one layers have to be designed for fabricating a single nanostructure, which decreases the machining efficiency, especially when machining a relative large area. Besides, for the setpoint force control system, there are many sources of disturbances which may further degrade the surface finish of layers, such as the rough machined surface, the interaction between AFM tip and the debris after machining the previous layer and the environmental noises. As a result, the prescribed area that is machined multiple times using layer-by-layer technique tends to have a larger surface roughness after accumulating all these factors.

Therefore, we further investigated one pass nanomachining with depth regulated by setpoint force in the raster scan mode. A similar 3D nanostructure as a bitmap image with 6 height levels was designed. The shallowest and the deepest levels are colored as black and white. Other intermediate layers are colored with linear interpolated gray, which represents a gradually increased setpoint force as well as the increasing machining depths. The bitmap image representing the 6 layers nanostructure is shown in the Figure 4.5 (e) and the schematic fabrication process of the six layers 3D nanostructure is shown in Figure 4.5 (a). The number of pixels for this image is set as 150×150 to achieve overlap percentage larger than 80%. The frame size of the 3D nanostructure is set as 1.6 × 1.6 µm. The width of each step in the structure was set as 265nm. The setpoint forces set for the six layers were gradually increasing from 150 nN, 180, 210, 240, 270 to 300 nN from the darkest color, shallowest layer, to the brightest color, deepest color. Besides the setpoint force and overlap percentage, other parameters are also specified. The machining speed was set as 1 µm/s. The driving voltages of xy and z-vibration were set as 30 mV and 3 V, respectively. Figure 4.5 (b) and (c) show the fabricated six layers result and the 3D view of it. It is clearly seen from Figure 4.5 (f) that six height levels were successfully machined on the PMMA surfaces. The fabricated depths for each layer are around 9 nm. According to the calibration results, the depths between two adjacent steps should increase by 8 nm. Practical results show that height varies along each step in the nanostructure.

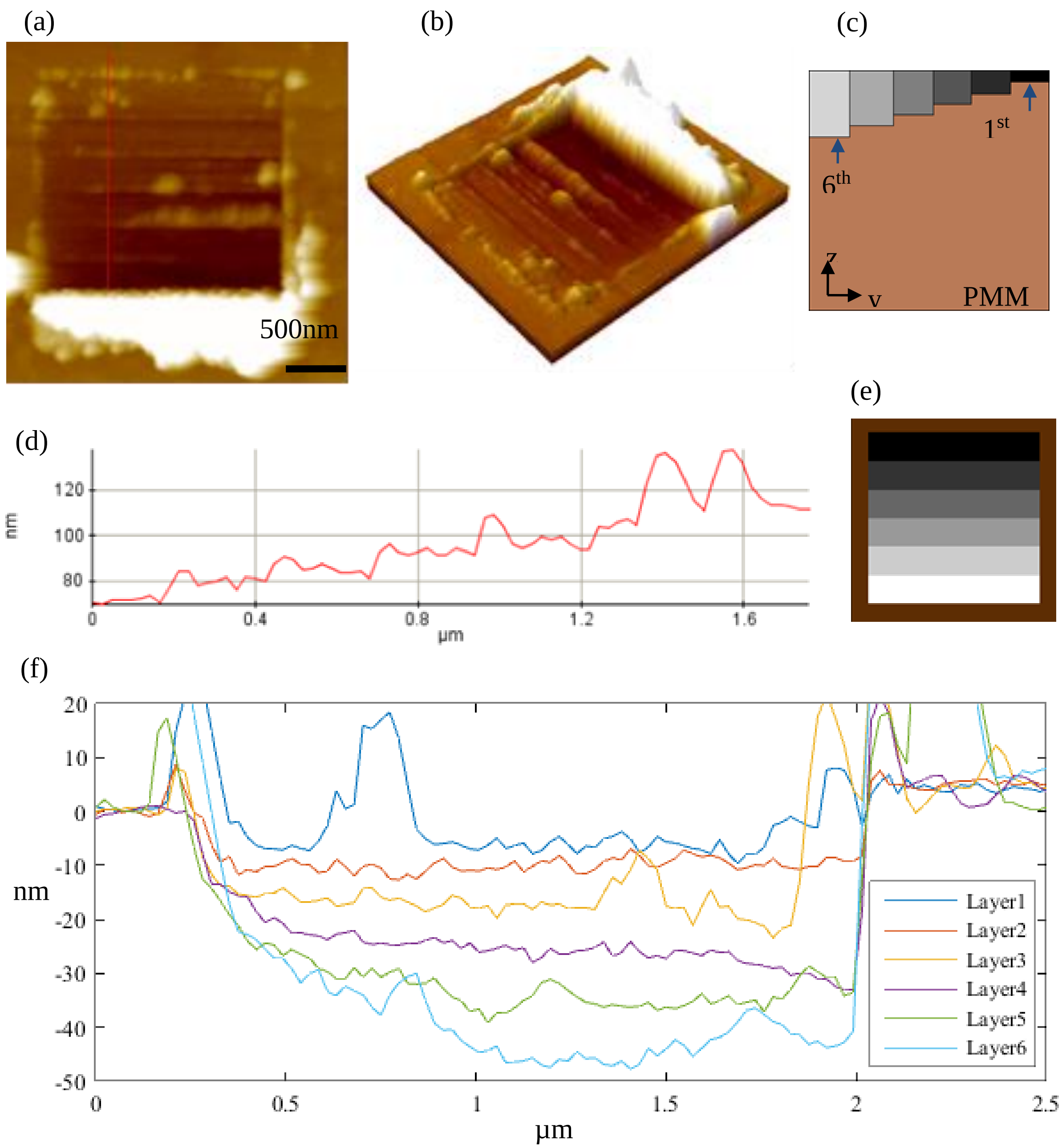

Figure 4.5 (a) AFM image of the fabricated 3D nanostructure. (b) 3D view of the nanostructure. (c) Schematic of one pass nanomachining with depth regulated by the setpoint force in raster scan mode. (d) Cross sectional profile of the nanostructure. (e) Bitmap images designed for the 6 layers nanostructure. (f) Cross-sectional profiles for each layer in the nanostructure.

Surface roughness (Ra) of all steps in the structure from the first step to the sixth are 0.8 nm, 1.0 nm, 1.3 nm, 0.9 nm, 1.1 nm and 1.9 nm. From the results (Figure 4.5), it can be seen that the depth at the left side is not that deep than that at the right side. The larger the setpoint force is, the more height difference along one step. The reason may be that the AFM tip did not fully penetrate to the depth it could when the machining speed is a little higher than the optimal speed. Figure 4.5 shows that layers 4, 5 and 6 requires increasing time to allow the tip fully indent into the PMMA since the relative flat area are around the location of 0.5, 0.8 and 1.1 μm. Taking into account the nanomachining start point and 1 μm/s speed, it needs 0.2, 0.5 and 0.8 s to fully penetrate to the depth it could for the layers 4, 5 and 6, respectively.

Other 3D nanostructures with complex contours were also designed and fabricated to further demonstrate the capability of this one pass machining with force regulation in the raster scan mode. A concave circle in a square was designed and fabricated. The bitmap image is shown in Figure 4.6 (a). The schematic of force applied on the sample surface according to the gray scale is shown in Figure 4.6 (b). Setpoint force of 300 nN and 150 nN were applied on white and black regions of the bitmap image, respectively. They were dynamically changed when the tip came across two pixels with different color, representing different gray scale values. The fabricated result which shows a concave circle pattern at the center of a pocket is shown in Figure 4.6 (c). Figure 4.6 (d) shows the cross-sectional profiles of the square pocket and the structure with concave circle. The depth of the pocket is around 10 nm and the depth of the circle is around 30 nm. The machining speed is 1 μm/s, the pixels are 150×150, the driving voltage for z-vibration is 6 V with 600 kHz and the driving voltage for xy-vibration is

30 mV with 2 kHz. The fabricated results replicated the patterns from the bitmap image very well, which demonstrate the capability of 3D nanofabrication by regulating setpoint force applied on samples in the raster scan mode.

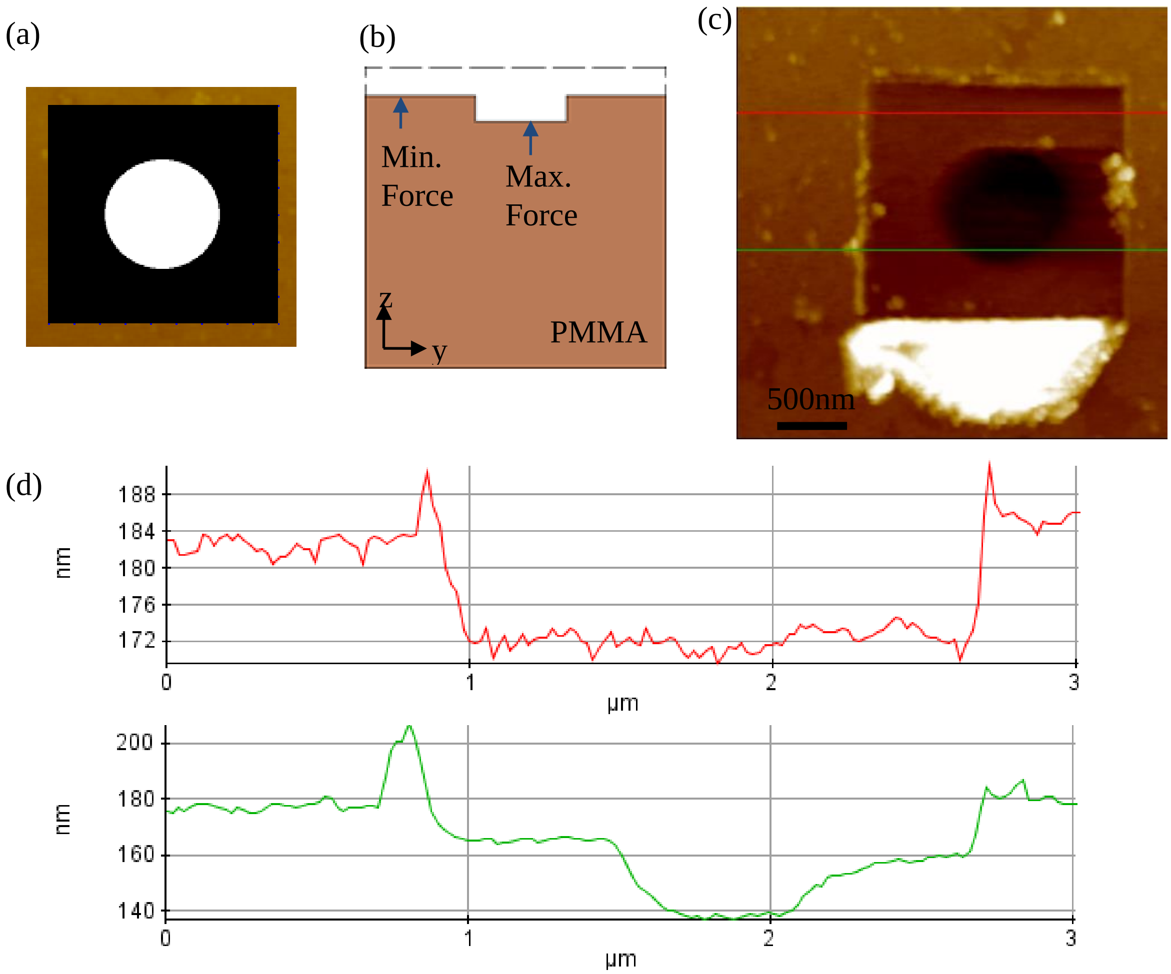

Figure 4.6 (a) A bitmap image designed for the 3D nanostructure with a concave circle in a square pocket. (b) Schematic of setpoint force applied on PMMA according to the gray scale. (c) Fabricated results according to the bitmap image. (d) Cross sectional profiles of the pocket surface and the concave circle in 3D nanostructure.

4.1.3 Analysis of the Process and Results

The setpoint force mode is a close-loop control mode by detecting the deflected laser beam from the back of the AFM cantilever as the detection and feedback signal. The controller adjusts the height of the AFM cantilever to maintain the desired contact force between the tip and the sample, which is indicated by the cantilever deflection and measured by detecting the reflected laser position through position-sensitive quadrupole photodetector. Also, the sample surface is not absolute parallel to the xy-plane. Despite this the novel 3D nanofabrication process using ultrasonic vibration assisted nanomachining under setpoint force control mode is still able to work on the sample surfaces and fabricate 3D nanostructures that are parallel to the sample surfaces.

During nanomachining processes, overlap percentage is one of critical factors to achieve good results and surface finish. Gap between center lines of two machining paths is larger than the diameter of the virtual tool if the overlap percentage is negative, which left a small un-machined areas that are not touched by AFM tip during machining processes. Therefore, a flat pocket surface cannot be achieved and rough surface with plowing-like structures are left on sample surfaces. But if the overlap percentage is too large (>60%), the area being machining will be overlapped in a large percentage with the previously machined places. A wedge shape nanostructure will be produced instead of a flat structure at each layer in multiple layers 3D nanostructures due to an area is machined several times. The reason comes from the fact that depths of 3D nanostructures are controlled by the setpoint force, not the absolute height of the tip. The height of the AFM cantilever and tip is adjusted up and down by control system in AFM. Using the same setpoint force, the feature depth can be affected by the different tip-sample interaction from the different overlap percentage of neighboring features.

Other input parameters also affect the machining result, such as the amplitude of z-vibration and machining speed. Increasing the amplitude of z-vibration will increase the depth of trenches for each machining paths, thus increase the dimension of final 3D nanostructure in z direction. Decreasing machining speed and increasing setpoint force can also increase the feature depth due to larger volume of material can be removed per unit time.

Both of the layer-by-layer machining and one pass machining can be successfully used to fabricate multi-layer nanostructures. Both of them can be implemented easily with gray scale bitmap images. The alignment error in layer-by-layer machining is not an issue in one pass machining as only one bitmap image is used and AFM tip machined the corresponding area only once. The limitations of the one pass machining are as follows. The difficulty in precisely control the feature dimension, as the gray-scale value directly represents the setpoint force, not the feature depth. The relationship between the setpoint force and the feature depth needs to be characterized experimentally, which is not a linear relationship when a large force range is crossed. At the same time, the response time of the setpoint force change from the AFM control system could be another limitation. It would limit the machining speed as well as the feature fidelity when the setpoint force changes quickly and frequently in very complex structures. Those limitations in the setpoint force control lead me to another approach of nanomachining, which is direct z-height control as follows.

4.2 3D Nanostructures fabricated under Direct Z-Height Control

In order to fabricate nanostructures with more accurate dimensions, a more reliable controlling approach in terms of depths fabrication should be employed. Besides the force controlling mechanism, which relies on the interaction force between samples and AFM tips, direct z-height control is another controlling approach that can be utilized in the nanofabrication process. The capability of z-height control mode for AFM-based 3D nanofabrication is investigated and demonstrated. Under this mode, the absolute z-height of the AFM cantilever is directly specified and controlled by the z-scanner. If the cantilever is rigid enough, the height of the AFM tip can be designed directly for machining features with designed depth. This approach is similar with the traditional CNC machining process, which controls the position of machining tools during fabrication processes.

4.2.1 Design of Pattern in Vector and Raster Scan Modes

Prior to the nanofabrication process, patterns should be designed by users and also be recognized by the AFM-based nanomachining system. Similar with pattern design under setpoint force control model, vectors and bitmap images can be used to design patterns. These two ways of designing features represent two approaches to define the feature geometry in xy-plane, implemented in two lithography-working modes: vector mode and raster scan modes.

In vector mode, dots, lines, rectangles, ellipses, polygons and polylines are six basic vectors for users to choose, design and arrange, which is similar with that in the setpoint force mode. Because of the xy-vibration assistance, widths of machining paths are enlarged to about 100nm, which gives a quantitative basis of calculation for the distances between two vectors to achieve a certain amount of overlap between machining paths. Combining and aligning designed vectors which represent machining paths to make sure that a certain area can be covered by machining paths. And if the depth properties indicated by vectors are different, 3D nanostructures can be fabricated after AFM tip finishing machining the whole area vector by vector. Figure 4.7 (a) and (b) give an example that uses vectors forming toolpaths to produce

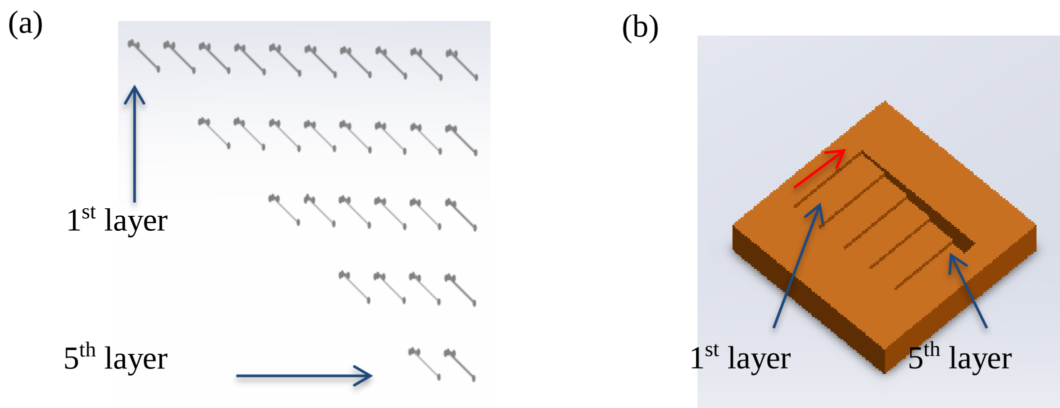

Figure 4.7 (a) Schematic of a five layers 3D nanostructure in vector mode. (b) Theoretical result after fabrication in vector mode. Red line shows the machining direction of single vectors.

3D nanostructure with five stairs. Five layers of vectors are combined together and aligned with each other as the toolpath to machine the 3D nanostructure (Figure 4.7 (a)). This is the layer-by-layer design technique, which requires tip machines five layers for five times in total, each layer a time with a constant depth penetration. The theoretical result of 3D nanostructure after machining is shown in Figure 4.7 (b). The machining paths follow directions of vectors, and here is the bottom to the top. The red line illustrates the directions of single machining paths. Besides layer-by-layer machining technique, it is also applicable to machine the whole nanostructure by machining the whole plane area once without back and forth. Using this technique, only one layer vectors are needed. However, the design depths of vectors representing for the deeper layer (right part in Figure 4.7 (b)) is larger than the shallower layers (left part in Figure 4.7 (b)).

In raster scan mode, the features are designed and depths on features are designed using bitmap images. The grey scale of the bitmap image represents different z-height of AFM cantilever, which is assigned for each pixel in the bitmap image. The brightest color (white) represents the maximum depth, and the darkest color (black) represents the maximum depth. The depth values between the maximum and the minimum are linearly interpolated by the grayscale value, which is the color on the image. Therefore, by filling colors as an appropriate grayscale and setting proper values in bitmap images, heights of the feature can be precisely specified. Figure 4.8 (a) and (b) show the bitmap image of a desired 3D nanostructure and the corresponding theoretical nanostructure after nanomachining process. In this mode, pixels set by users in bitmap images define the resolution of the designed and would affect fabricated feature for machining processes. The number of pixels in column determines the overlap percentage between two adjacent machining paths when the virtual tool size is known. The pixels in rows determine the in-plane feature resolution of the tip height control. Complex structures can be designed much easier than in vector mode.

(a) 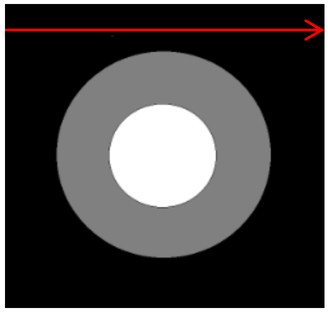 (b) 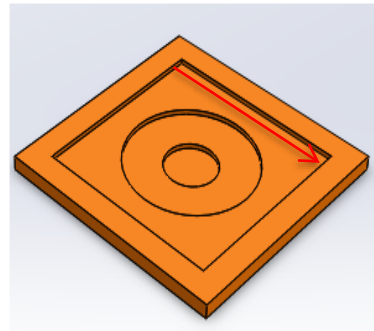

Figure 4.8 (a) Schematic of raster scan mode using a 3D nanostructure represented by a grey scale bitmap image. (b) Theoretical result in raster scan mode with depth represented by the grey scale. Red lines show the rapid direction of nanomachining.

The AFM nanolithography software interface is shown in Figure 4.9. Under z-height control mode, a desired pattern can be imported into the nanolithography software. Figure 4.9 shows a three layer concave nanostructure with 70 pixels in row and 70 pixels in column. The “ScanRate” is the machining speed. The values of “Z Pos Max” and “Z Pos Min” are the max and min absolute values of depths based on a reference point. The background image is the surface topographic image acquired from contact mode.

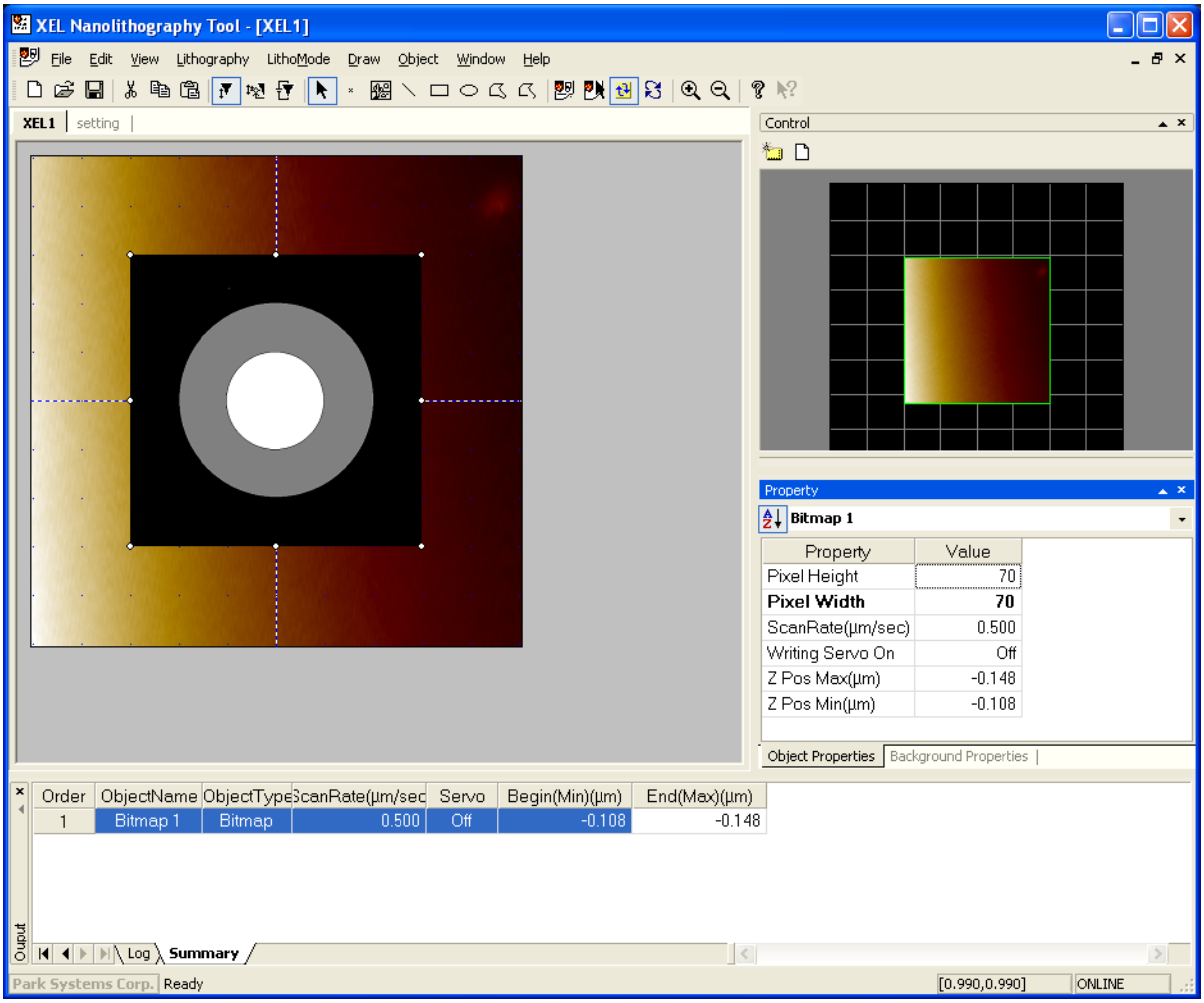

Figure 4.9 Z-height control mode interface of nanolithography parameter design.

3D nanofabrication processes are controlled through the lithography software. The designed patterns need to be recognized by AFM nanolithography software. In the software vectors and features are allowed to be designed precisely in nanometer resolution. Under z-height control mode, desired patterns are designed (patterns created by combining vectors) or imported (patterns depicted by grayscale bitmap images) into the nanolithography software.

In vector mode, the tip follows the vector-based trajectory (i.e. toolpath) one by one according to the specified sequence until all of them are machined. The z-height of the feature is controlled by setting two absolute height values for each vector, the values of the heights from the starting point and the ending point. If heights for the start point and the end point are different, the tip height changes continuously from the starting point to the end during machining process.

In raster scan mode, bitmap images with grayscale values are used. The AFM tip scans the image pixel-by-pixel from the left to the right and from the top to the bottom. The AFM tip height changes according to the grayscale of the pixel during machining processes continuously. After finishing one line, the tip lifts up and moves to the left side of the second line below it. The entire machining process will finish at the bottom-right corner of the feature. The tip trajectories are parallel lines with directions from the left to the right as illustrated by red lines in Figure 4.8.

4.2.2 3D Nanofabrication Process and Results

After employing the 3D nanofabrication process under z-height mode, 3D nanostructures are fabricated. Results in both vector mode and raster scan mode demonstrate the capability of this 3D nanofabrication process.

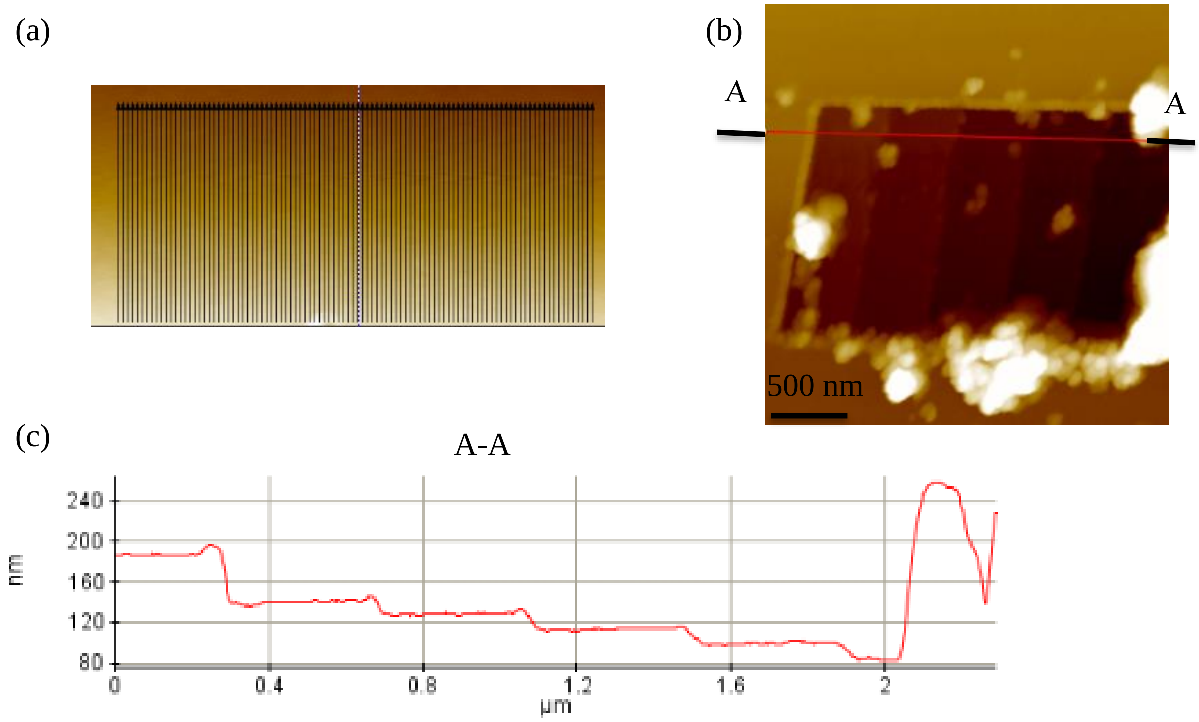

Figure 4.10 (a) Vectors combined for a five layer 3D nanostructure in lithographic software. (b) Result of a 3D nanostructure with five steps after nanomachining. (c) Cross sectional profile of the feature.

In vector mode, a stair-like 3D nanostructure with five steps is machined, which has designed depths of 20 nm for each step. The parameters used in this machining process are as listed in Table 4.1.

Table 4.1 AFM-based nanomachining system input parameters

	xy-vibration amplitude (mV)	Xy-vibration frequency (Hz)	Machining speed (µm/s)	Overlap percentage
Value	30	2k	0.5	>60

Layer by layer technique is applied to fabricate at each height level. The fabrication process starts from the first step, in which the depth is designed as 35 nm from the PMMA surface. The extra 15 nm depth is designed for the first layer to compensate for any surface non-flatness and tilting. After finishing the first layer, the rest of the layers are machined one by one in sequence with tip height reduced 20 nm for each subsequent layer but with gradually shrinking area to fabricated each and every step in the structure. The schematic of the design as illustrated in Figure 4.10 (a) shows that 100 parallel lines are designed for the first layer, in order to cover the entire machining area with 2 μm in length. Distances between every two adjacent lines are designed as 20 nm, which depends on the size of the virtual tool under specific xy-vibration driving voltage and the overlap percentage that can provide good machining performance. If the overlap rate is too large, more lines need to be combined to machine the same area, which increases the machining time and tip wear. But if the overlap rate is too small, machined surface quality may not be satisfactory due to plowing features and un-machined area. There are 100, 80, 60, 40, 20 lines designed for the five-layer 3D nanostructure from the top layer to the bottom.

The five-level staircase nanostructure was successfully fabricated and can be clearly imaged after cleaning process, as shown in Figure 4.10 (b). Actual depths of each layer from the top to the bottom are 45 nm, 15 nm, 16 nm, 15 nm and 15 nm respectively, as shown in Figure 4.10 (c). The first layer can be treated as an initial calibrating layer to remove the non-flatness and non-parallelism between the sample surface and xy-plane of the AFM. For the remaining layers, the resulting height is 5 nm less than the designed height. The difference in height comes from the non-rigid cantilever. Since the spring constant of the cantilever is not infinitely large, the tip-sample interaction deflects the cantilever from the design displacement from the z-scanner. As a result, the actual feature depth is a little less than the designed height. The height difference between the actual value and the designing value can be compensated for by selecting a larger depth in design. The cross sectional profile in Figure 4.10 (c) shows uniform and flat five stairs with average surface roughness of 0.5 nm. The walls between two steps are not perfectly perpendicular to the steps because of round shape of the tip and the virtual tool, which leads to a slightly sloped wall between two layers.

In raster scan mode, the 3D fabrication capability was further evaluated. A 3D nanostructure with two deep circles and a shallow square was designed, as shown in Figure 4.11 (b) and (d). The schematic of fabrication process is illustrated in Figure 4.11 (b). The tip machines the area from the top-left corner to the right and gradually scans down as process proceeds. Wherever there is a color change, the height of the tip changes accordingly. Depths designed for the layers with black, 50% gray, and white color are 15 nm, 45 nm and 75 nm respectively. Since the lateral dimensions of the pocket are 1.5 μm and the size for each pixel is selected 20 nm, the bitmap image has 75 pixels in each row and column. Similar to the vector scan mode, the pixel value needs to be selected carefully to achieve the good machining performance with minimum cycle time. The scanning speed is set as 0.5 μm/s, which is the same as the machining speed in vector mode. After machining and washing away the debris processes, Three-layer 3D nanostructures were successfully fabricated and imaged, as shown in Figure 4.11 (a) and (c). Actual depths for the layers with black, 50% gray, white color are

12 nm, 42 nm and 74 nm respectively. Actual heights are only around 2-3 nm less than the designed heights. The nanomachining approach reproduces the 3D nanostructrues from the bitmap image with very good fidelity.

Comapring the vector mode and the raster scan mode in z-height controlled 3D nanomachining processes, the vector mode is more efficient for sparse pattern fabrication, and the raster scan mode is capable of fabricating very complicated structures. Users can conveniently design the trajectory (i.e. toolpath) of the tip under the vector mode and arrange vectors together to get sparse nanostructures without scanning through all areas. However, it is much easier to design and fabricate complex 3D nanostructures using bitmap images in raster scan mode. For example, the stair-like nanostructure in Figure 4.10 (b) can be conveniently fabricated using the vector mode, but it is very difficult for users to design and manually arrange vectors in order to create a circle. Another concern between two modes is that the spring constant of the cantilever is not the same when machining in different direction. However, with the help of xy-vibration, cantilever with nominal stiffness of 48N/m is stiff enough in raster scan mode. As shown in Figure 4.11, the depths achieved in raster scan mode are very close to the designing depths. Therefore, raster scan mode is used to further investigate the capabilities of the 3D nanofabrication approach for complex structure fabrication.

Complex nanostructures with continuous change of contours are further investigated. The complexity is represented by bitmap images, as shown in Figure 4.12 and Figure 4.13, were used to investigate the capability of nanomachining approach on complex contours. The logo of the Edward P. Fitts Department of Industrial and Systems Engineering “ise”

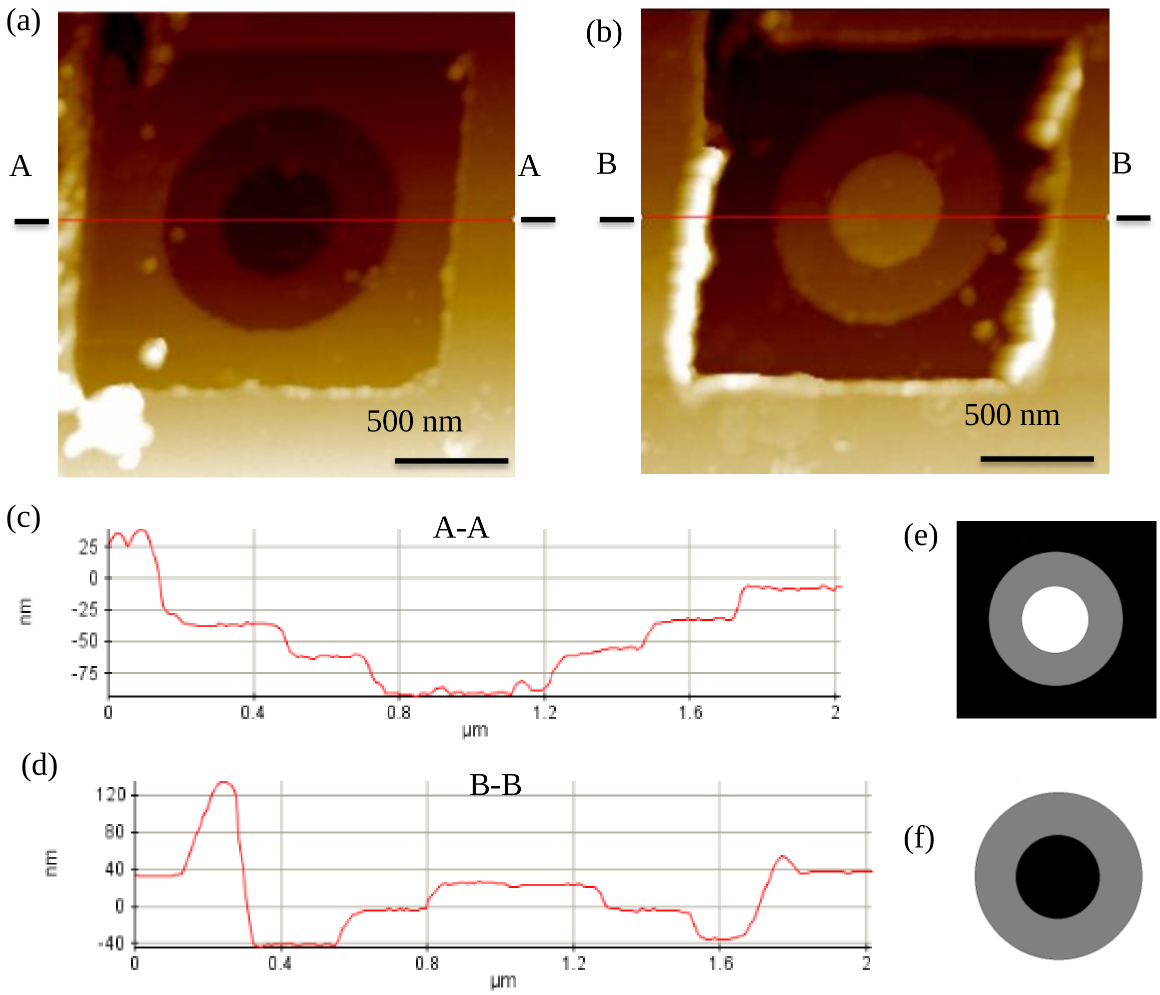

Figure 4.11 **(**a) Three-layer nanostructure with two circular cavities. (b) Three-layer nanostructure with two circular protrusions. (c) Cross sectional profile of 3D nanostructure with two circular cavities. (d) Cross sectional profile of nanostructure with two circular protrusions. Bitmap images designed for 3D nanostructure with (e) two concave circles and (f) two convex circles.

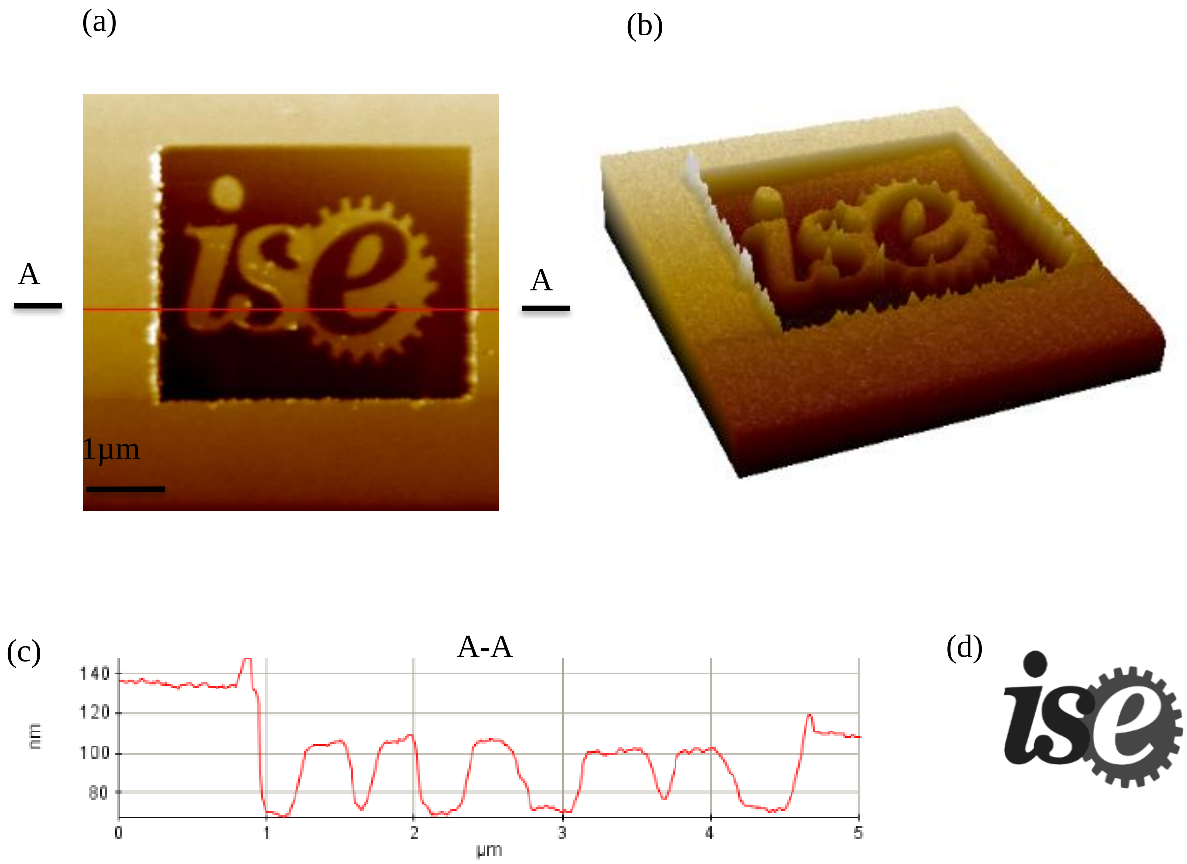

Figure 4.12 (a) 3D nanostructure of the logo “ise”. (b) 3D view of “ise”. (c) Cross sectional profile of “ise” letters. (d) Bitmap images of “ise”.

the logo of National Science Foundation “NSF” were designed into bitmap images and fabricated by z-height control mode, shown in Figure 4.12 (d) and Figure 4.12 (d).

In the “ise” bitmap image, shown in Figure 4.12 (d), the letter “i” and “s” are filled with black color, corresponding to the smallest tip moving distance from the reference point. The letter “e” is filled 73% degree of gray, corresponding to the 73% AFM moving distance of the largest setting height value. Height from bottom to letter "i" and "s" is designed as 35 nm and height difference between "is" and "e" is designed as $35 \times 0.27 = 9.45$ nm. The overall pocket that contains the "ise" logo is 3.6×3 µm and the density of designed pixels is 80/µm.

The nanostructure from the 3D nanomachining successfully replicated the designed bitmap images onto PMMA film. Figure 4.12 (a) and (b) show the result after nanofabrication of the logo "ise". High-resolution features, such as the gear teeth with width of around 200 nm were successfully produced. From the cross-sectional profile of "ise", as shown in Figure 4.12 (c), height of "is" is 39.5 nm and height difference between "is" and "e" is 6.5 nm. The dimensions are close to the set values.

In the logo of "NSF", three letters "NSF" are black, the circle under NSF is 67% degree of gray and the outside ring is 33% degree of gray. Height from bottom to "NSF" is designed as 45 nm. Therefore, the setting height from "NSF" to the circle is designed as 15 nm. Height from the circle to the outside ring is designed as 15 nm. The overall size of the pocket that contains the logo "NSF" is 3.6×3.6 µm. Density of designing pixels is 80/µm.

Figure 4.13 (a) shows the result after nanofabrication of the logo "NSF". Heights of the outside ring, the circle and the "NSF" are around 9 nm, 20 nm and 34 nm respectively. 3D views of the logo "NSF" is shown in Figure 4.13 (b).

From these results above, we can see that the dimensions are close to the designed values and that 3D patterns are fabricated precisely. It demonstrated the capability of fabricating the 3D nanostructure with complex geometry using the nanomachining approach by z-height control mode.

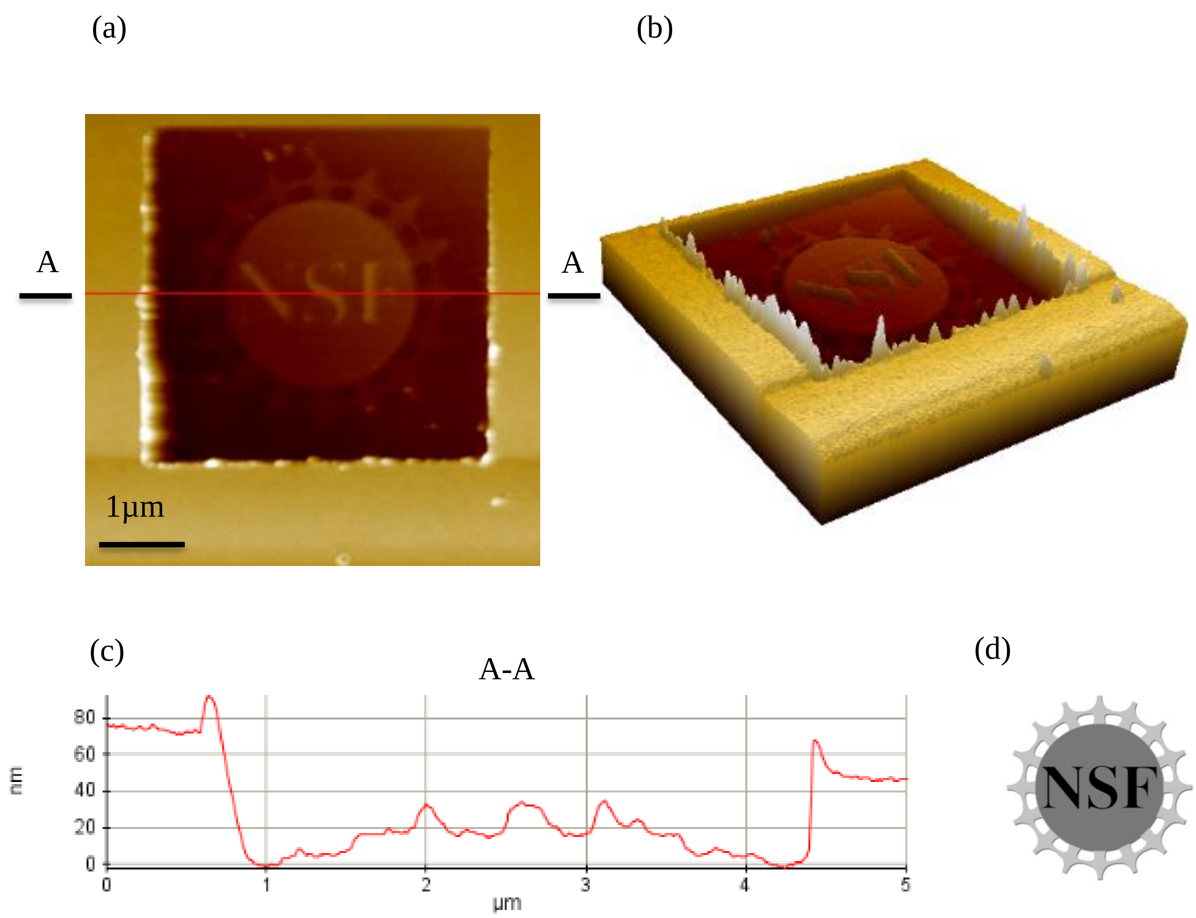

Figure 4.13 (a) 3D nanostructure of “NSF” logo. (b) 3D view of “NSF” logo. (c) Cross sectional profile of “NSF” logo. (d) Bitmap image of “NSF” logo.

Moreover, nanostructures with complex contours as well as continuous height changes are designed and fabricated by nanomachining in raster scan mode. Nanocone, nanopyramid, 3D profiles of Steve Jobs are fabricated by z-height control mode using ultrasonic assisted nanomachining process. These results further demonstrated the capability of the novel 3D nanofabrication process.

Figure 4.14 (d) shows the bitmap image of a cone shape nanostructure. It is filled with continuously increasing grayscale from the outside board to the inner point. The darkest point corresponds to the shallowest depth the AFM tip will engage during nanomachining process.

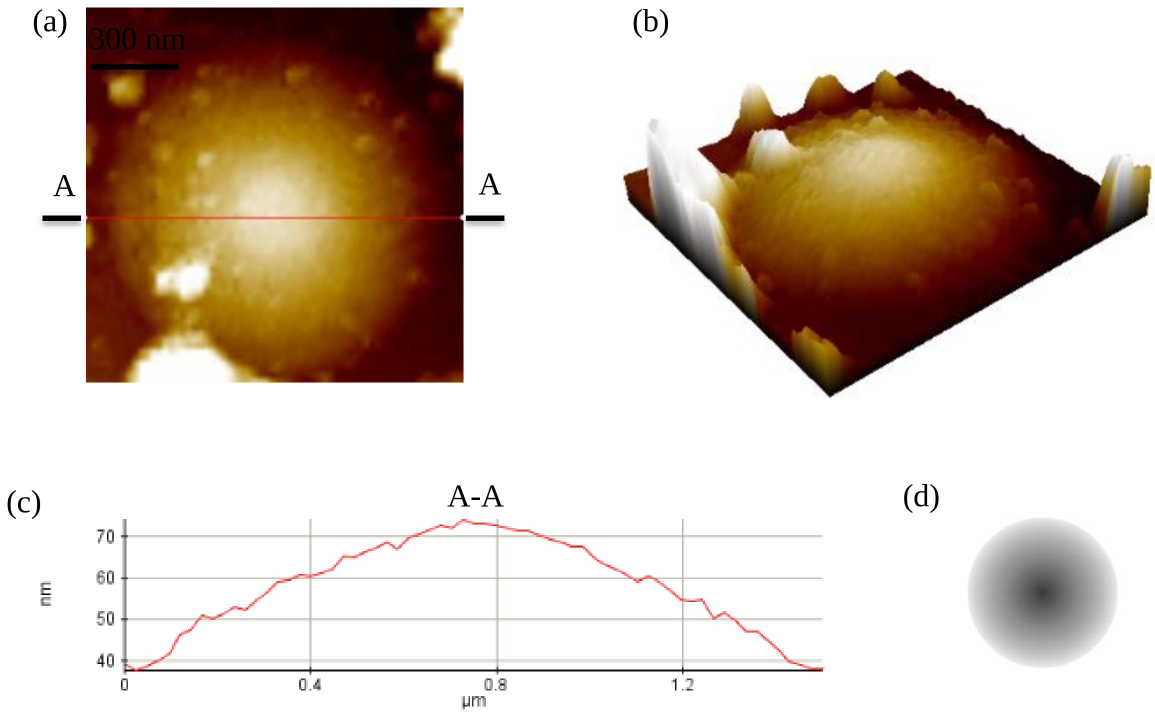

Figure 4.14 (a) Fabricated nanocone structure and its (b) 3D view. (c) Cross sectional profile of the nanocone. (d) Bitmap image of the nanocone.

The color of the darkest point is design as full black. The height difference between the black and white color is set as 40 nm. Density of designed pixels is 80/µm. After implementing the nanofabrication process, a cone shape 3D nanostructure is created. Figure 4.14 (a) shows the result after fabrication. The result clearly shows the shape of the nanocone structure with high fidelity although there are some debris covering a portion of the area around the structure.

Figure 4.14 (b) is the 3D view of the nanocone structure. Cross-sectional profile of the nanocone structure is shown in Figure 4.14 (c). It shows that the actual height after fabrication is 36 nm.

Figure 4.15 (d) shows the bitmap image of a pyramid shape nanostructure. The bottom of the pyramid nanostructure is a small area of flat surface with a margin, which

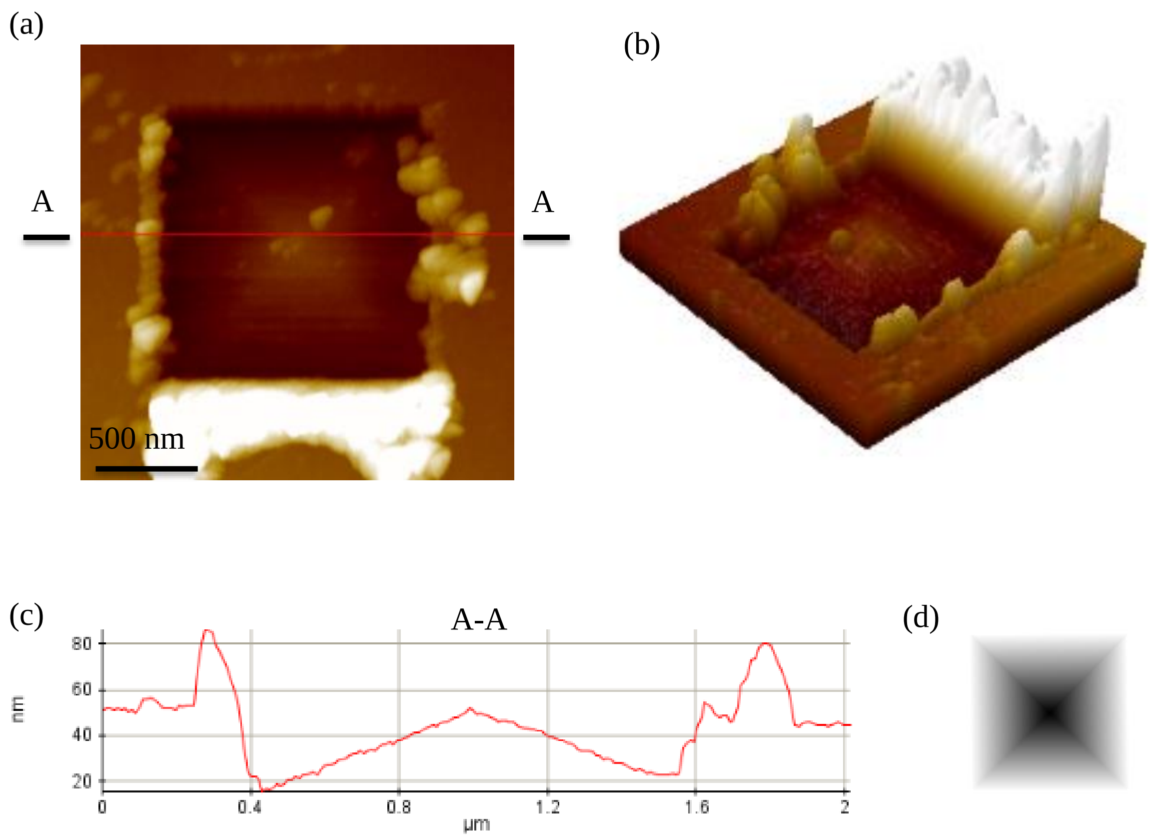

Figure 4.15 (a) The fabricated pyramid nanostructure and its (b) 3D view. (c) Cross sectional profile of the nanopyramid. (d) Bitmap image of the pyramid nanostructure.

makes sure that the wall of debris does not cover the nanopyramid structure. The color of the bottom area is design as full white. The machining parameters are maintaining the same except for choosing a reasonable pixel number, which is a tradeoff between the resolution of nanofabrication and the machining time. Similarly, the bitmap image of the cone structure is also designed and filled with continuous changed grayscale from full black to full white indicating the continuous nanomachining processes. Figure 4.15 (a) and (b) show the pyramid result and 3D view after fabrication. Cross-sectional profile of the nanopyramid structure is shown in Figure 4.15 (c). The actual height after fabrication is 36 nm.

Additionally, a 3D profile of Steve Jobs was fabricated. The original profile of Steve Jobs is the cover picture of his biography written by Walter Isaacson [154], shown in Figure 4.16 (d).

This bitmap image is set a height value of 40 nm between the between black and white color. Density of designing pixels is 80/μm. Figure 4.16 (a) and (b) show the profile and corresponding 3D view after fabrication, respectively. Cross-sectional profile of the profile from the forehead across the nose to his hand is shown in Figure 4.16 (c). The actual height between the highest and the lowest area after fabrication is 36 nm.

Results of 3D nanopyramid, nanocone and Steve Jobs' profile are successfully fabricated. Shapes and dimensions were fabricated in close correspondence to the designed values. All the results strongly demonstrate the capability of the nanomachining approach in z-height control mode for 3D nanostructures fabrication.

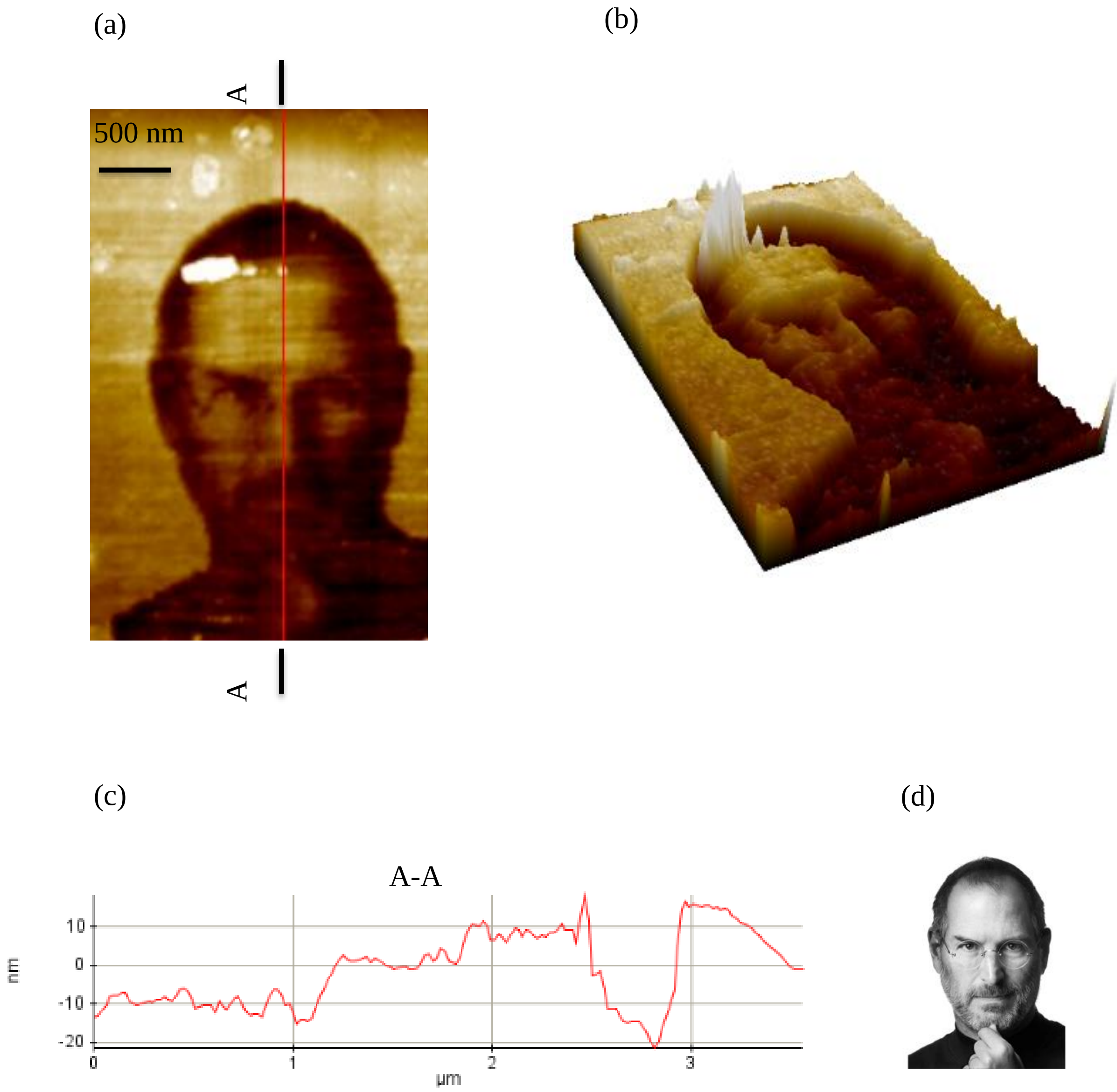

Figure 4.16 (a) 3D nanostructure of Steve Jobs' profile. (b) 3D view of the nanostructure. (c) Cross sectional profile and (d) Bitmap image of Steve Jobs' profile.

The Steve Jobs's profile with continuous high variations is the representative result of the most complex 3D structure that can be produced by this process. In order to understand the capability of this process, we compare the final 3D nanostructure of Jobs' profile with the original grayscale profile. Cross-sectional profiles extracted from both images at the same location are overlapped together to compare the differences. Six comparisons are completed in total. As shown in Figure 4.17 (a) and (b), the original grayscale image and the final 3D nanostructure are covered three horizontal and three vertical lines. The locations are 1/4, 1/2, and 3/4 from effective boards (upper or left) of rectangular frame that includes patterns. The cross-sectional profiles from the same location are plotted in the same frame with dashed (original) and solid (3D nanostructure) lines. Figure 4.17 (c) and (d) and Figure 4.18 give the comparison of all six locations. Figure 4.17 (c) compare two vertical left lines (1/4 location), and it shows that the overall trend is consistent. But the sharp wall between 3-3.5 μm is not maintained as in the original. In addition, some sharp features are not replicated very well. This is because of the shape of the 3D virtual tool. The AFM tip could be considered as a sphere when the machining depth is smaller than 15 nm. However, the AFM tip outside wall has a half cone angle of at least 10°. Besides, the high-frequency xy in-plane vibration increases the tool diameter and at the same time decrease the capability of producing fine features with larger than 60% overlap percentage. Figure 4.17 (d) and all plots in Figure 4.18 show a favorable overall shape comparison between original profile and the produced feature, but the same challenges persist. The 100 nm width and 15 nm protruding features showing in the dashed lines were not produced because of the internal limitation in this machining process.

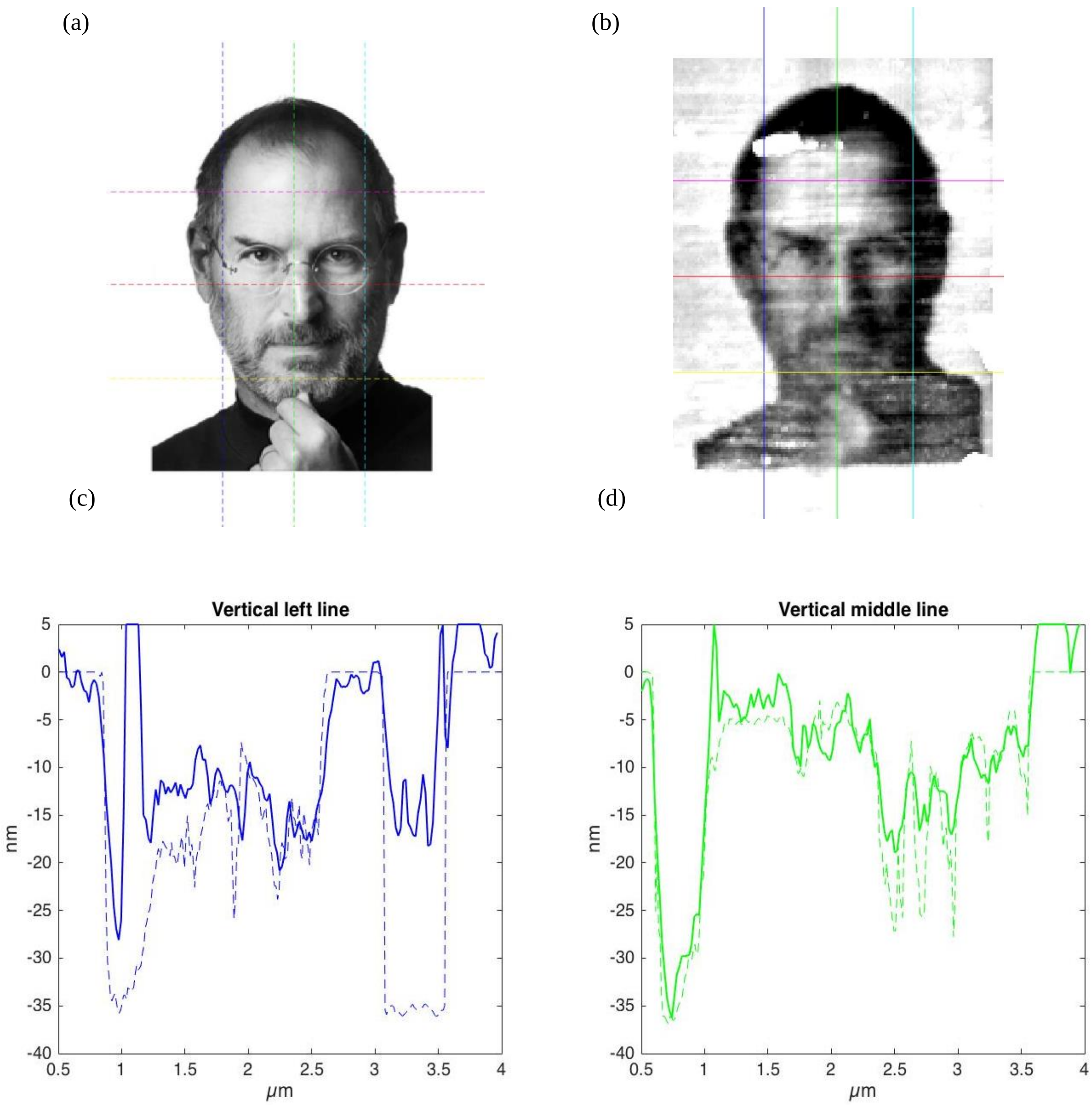

Figure 4.17 (a) Original grayscale bitmap image of Steve Jobs' profile. (b) 3D nanostructure after fabrication using the bitmap image (a). (c) Comparison of cross sectional profiles of vertical left lines at 1/4 location. (d) Comparison of cross sectional profiles of vertical middle lines at 1/2 location.

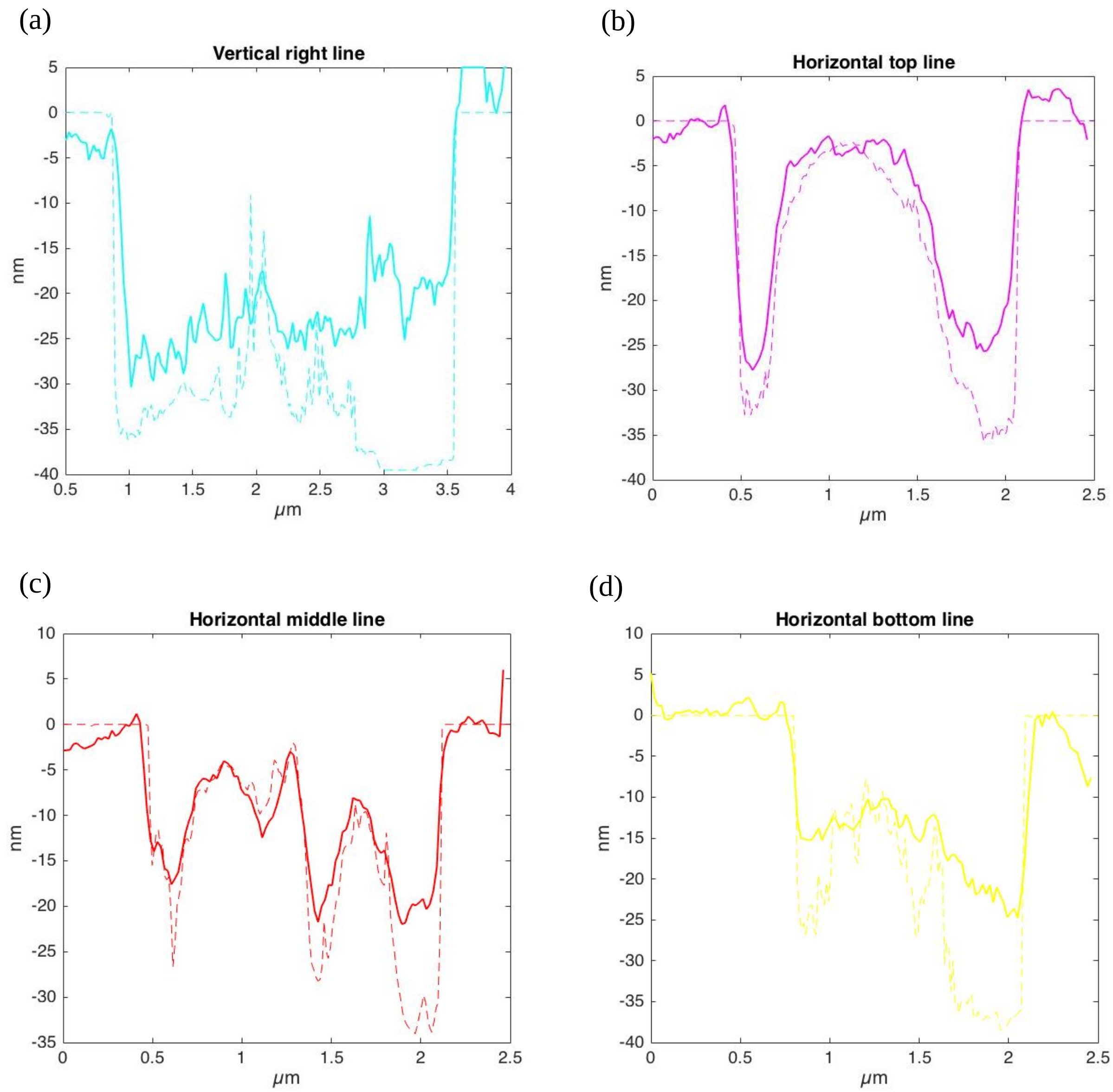

Figure 4.18 Comparison of cross sectional profiles of (a) vertical right lines at 3/4 location from the left board, (b) horizontal top lines at 1/4 location from the upper board, (c) horizontal middle lines at 1/2 location from the upper board, and (d) horizontal bottom lines at 3/4 location from the upper board.

4.3 Comparing 3D Nanomachining Processes by Two Control Modes

From the above 3D nanostructures fabricated by setpoint force mode and z-height control mode, differences between two control mechanisms and the capabilities of nanofabrication are compared and discussed here.

First, I fabricated 3D nanostructures by setpoint force control. This is a closed loop control mode detecting and maintaining the setpoint force as a constant value. Advantages and disadvantages exist using this control mechanism. It allows the user to directly and easily set the force applied on sample surfaces during machining process, which usually helps define the depths of trenches. Usually, the sample surfaces are not flat without any tilting. Nanofabrication processes by setpoint force control can produce 3D nanostructures that are parallel to the sample surfaces. Moreover, users know and set the values of the normal force applied on sample surfaces.

Theoretically, setpoint forces could be used to get feature depths at a certain machining speed; even surfaces have a certain tilting angle. However, even though we can directly set the setpoint force applying during nanomachining processes, it is still not easy to control the depths of designed 3D nanostructures. There are factors making the force control not easy to achieve high quality features or even have adversely affect the machining process, including the non-linear relationship between the setpoint force and the feature depths, the overlap percentage, the debris formed during machining process, and the original surface waviness. The first reason is that it is not a linear relationship between the achieving depths of pockets and the setpoint force. In this case, it is not easy for the user to interpolate the numerical value to get the desired depth values. Second, the debris formed during machining process interacts with the tip, giving feedback force information that actually partially applied on the debris other than PMMA surfaces. Therefore, the setpoint force applied on PMMA surface will be disturbed by debris and become unstable, which makes the depths control unstable. In addition, there is a certain waviness along the surfaces of spin-coated samples. Ideally, if the setpoint force applied on PMMA is maintained as a constant value, changes of feature depths caused by constant setpoint force should also be a constant value. That is to say that the final feature depths should be the original surface minus a constant value. Therefore, the waviness of original PMMA surfaces will be all reflected on surfaces of resulting nanostructures. At the same time, surface roughness will be even worse when using the layer-by-layer nanomachining technique, because the waviness and other disturbances such as environmental noises will be accumulated. Even in design stage, overlap percentage between neighboring features (as a common practice in conventional scale CNC machining process) is a critical input parameter and it is not easy to find an appropriate range. If the overlap percentage is too large (>60%), the newly machined features are overlapped a lot with previously fabricated areas. The overlapped area can be machined two or more times under the same setpoint force, the wedges instead of several layers are fabricated. If the overlap percentage is too small, there are ploughed area with protruding structures that not covered by the virtual machining tool and paths.

Besides the setpoint force mode, z-height control mode is another control mode useful in regulating the depths of 3D nanostructures. In this mode, the absolute z-location of the cantilever is directly specified by the user and controlled by the z-scanner. Assuming the cantilever is infinite rigid, the location of the cantilever can be selected directly for machining features with designed depths, which is similar with traditional CNC machining process. Therefore, the 3D nanostructures fabricated by z-height control mode has higher surface finish since the noises affect little when I directly control the absolute z-height of the AFM tip.

In order to demonstrate the superiority of the z-height control over the setpoint force control, three layers nanostructures are fabricated, as shown in Figure 4.19. Two patterns are fabricated under each of two controls to compare the differences. Figure 4.19 (a, b), and Figure 4.19 (c, d) show two results under each of setpoint force and z-height controls, respectively. Within the two results of each control, one is fabricated in combined vectors and the machining paths are designed layer-by-layer from left to right, as shown in Figure 4.19 (a, c). The other is fabricated based on self-designed bitmap images, as shown in Figure 4.19 (b, d). The depths of each layer for four patterns I was trying to achieve from Figure 4.19 (a) to (d) are 15, 25, 25, 15 nm, respectively. The y=0 dotted lines are starting references of AFM tip height in all cross-sectional profiles, which is also the surfaces of original samples. In Figure 4.19 (a), although initial areas of each layer have depths close to 15 nm, depths of each layer decrease rapidly. The reason may be that setpoint forces on PMMA surfaces was disturbed by the debris accumulated in the machining. The value of setpoint force is small, so when the AFM tip has any contact with debris, the actual force applied on original sample surfaces are reduced, resulting random actual force applied on samples. Figure 4.19 (b) shows the second pattern with carefully tuned machining parameters. Although the feature depths are close to 25 nm under larger setpoint force and this feature has much clearer three steps than that in Figure 4.19 (a), it still has obvious non-uniform surfaces along with either length or width direction of each layer, as shown in Figure 4.19 (f) and (j). The maximum peak to valley values of the feature surfaces of Figure 4.19 (i) and (j) are 21.3 and 14.5 nm, respectively. This are almost the values of desired feature depths.

By directly set absolute locations of the tip without relying on the setpoint force, the nanomachining process are stable and at the same time easier to implement than that under setpoint force mode. Figure 4.19 (c) and (d) show the results under height control. Layer depths of the third pattern are 22, 22 and 25 nm, as shown in Figure 4.19 (g). Layer depths of the fourth pattern are 15, 15 and 17 nm, as shown in Figure 4.19 (h). The maximum peak to valley values along the feature surfaces are 8.7 and 6.4 nm, respectively. This two maximum peak to valley values are much smaller than that of patterns fabricated under setpoint force control. The surface roughnesses (Ra) of them are 1.2 and 0.9 nm, respectively. The maximum peak to valley values and the surface roughness (Ra) clearly demonstrate the superiority of the z-height control mode over setpoint force mode in 3D nanostructures fabrication.

Besides vertical dimensions, I also investigated lateral dimensions of these comparable results fabricated under height control. The bitmap image covered areas for all four patterns are 1.6×1.6 μm. The location with deeper features involve more AFM tip body shape in the machining process, and resulting wider features. That is because the nominal half cone angle given by the manufacturer is 25°–30°. So the actual designed lateral dimensions for pattern three and four are 1.730×1.730 μm and 1.710×1.710 μm, not the bitmap covering area 1.6×1.6

μm, if assuming 100 nm virtual tool diameter when feature depth is 10 nm. For the third and fourth patterns, calculating in a similar way, the fabricated lateral dimensions are 1.726×1.722 μm and 1.703×1.701 μm, respectively. Considering the dimensional variations of tips, the actual lateral dimensions of features are successfully fabricated as designed.

Under z-height control mode, the nanomachining processes are not severely affected by those factors adversely affecting the process in setpoint force control. The AFM tip locations is maintainted at the desired location with the help of ultrasonic vibration in material removing processes. So the surface waviness will not be reflected on final surfaces of features. Also because the tip location is regulated in height control, when a flat surface feature is in fabricating, the overlapped areas will not be machined multiple times as in force control. Therefore, vertical dimensions will be more uniform than that of force control. Moreover, loosely packed debris has little impact on the tip location and the final pattern surfaces since the tip is rigid and stable enough to even remove materials. Lastly, unlike the non-linear relationship between the setpoint force and the actual depth, the difference between actual depths and assigned base depth is a constant value, which is determined by z-vibration at a certain level. As a result, fabricated actual 3D nanostructures could achieve desired depths in precise by linearly interpolating the characterization results.

This is not to say that the z-height control nanomachining has no limitations. The overall control of the absolute location of the AFM tip is open loop. Z-piezo drifting is a factor that affects the dimension of the overall nanostructures. AFM system needs to be warmed up in an appropriate way for a relatively long time before the machining process.

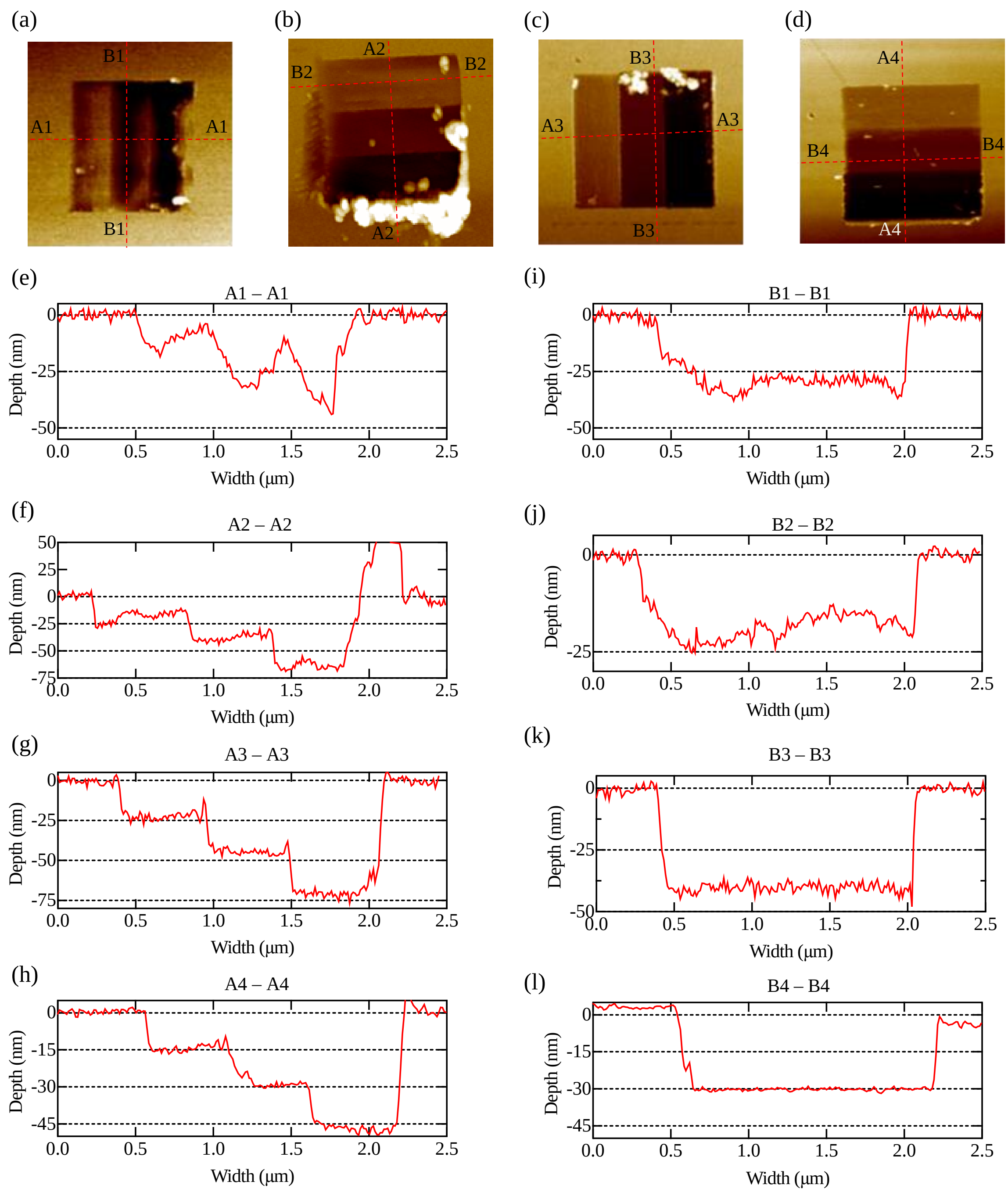

Figure 4.19 Nanostructures fabricated under (a) setpoint force control mode using combined vectors layer-by-layer, (b) under setpoint force control using a bitmap image, (c) under height control using combined vectors layer-by-layer, (d) under direct height control using a bitmap image. (e) - (l) are cross-sectional profiles corresponding to the AFM images above.

Otherwise, 3D nanostructures may not be fully fabricated if the drifting is too much. Also, the absolute z-height control approach requires the sample surfaces as not tilting as possible. When the sample is not absolute zero-tilting, the amount of material that needs to be machined away from the reference point is more than that in the near area. If the tilting angle is too large, the machining capability and the quality of the 3D nanostructures are degraded. Therefore, the tilting angle is usually controlled and adjusted as 0.58°. That means height increases or decreases a few nanometers across one micrometer.

Overall, the results fabricated above show that it is capable to fabricate complex 3D nanostructures such as several layers of staircases and arbitrary contour shapes with several height levels under both of the two control mechanism. And the results fabricated by z-height control mechanism are more precise and have better surface finishes than that by the setpoint force control mechanism.

4.4 Transferring 3D Nanostructures from PMMA to Silicon

Previous 3D nanostructures are fabricated on PMMA films spin-coated on silicon substrate. PMMA as a polymer material would not wear the AFM tip too much. Therefore, the fidelity of 3D nanostructures are maintained well during machining processes. Besides on PMMA, 3D nanostructures on silicon are also needed, motivated by many applications. For example, masters of nanoimprint lithography on silicon last longer than that on PMMA films, which suffers from polymer degradation. Additionally, 3D nanostructures on silicon can be used to fabricate MEMS/NEMS devices and micro/nano fluidic devices. However, 3D structures transfered in nanoscale have rarely been investigated, although 2D patterns transfer have been researched and applied on devices fabrication for a long time. Therefore, Reactive Ion Etching (RIE) process is utilized to transfer 3D nanostructures from PMMA films on silicon substrates. The RIE recipe is calibrated to use SF_6 and O_2 to etch the PMMA and silicon substrates. Selectivity and the corresponding etching parameters are further tuned to decrease the depths of 3D nanostructures on silicon surfaces and reduce the surface roughness.

4.4.1 Recipe Calibration of Transferring 3D Nanostructures

Reactive ion etching (RIE) process is an etching technology that utilizing plasma to etch material in an anisotropic way. Plasma is created by applying a radio frequency (RF) electromagnetic field between two electrodes that placed in a vacuum chamber. Under the process combining mechanical sputtering and chemical reaction, silicon is etched away. RIE has been used to transfer 2D patterns on various substrates but rarely applied for 3D nanostructures. In order to achieve effective etching, different gases are required for different substrates. SF_6 has been widely used to etch silicon and O_2 is a good choice to get rid of PMMA. Therefore, SF_6 and O_2 were chosen as etching gases in RIE for 3D nanostructures transfer in the following experiments.

Figure 4.17 illustrates the transferring of 3D nanostructures from PMMA film to silicon substrate. At the beginning, only PMMA is etched by O_2 to remove the residual layer that covers on the silicon surfaces after fabricating 3D nanostructures. After removing all PMMA residual layer, SF_6 is involved in the etching process to etch silicon surface. As etching continues, structures on PMMA films are gradually transferred on silicon and PMMA films gradually etched away. In the final stage, all the PMMA covering on silicon is removed and the 3D structures on PMMA will be transferred on silicon. One observation in the process is that there is a natural silicon oxide layer with thickness less than 2 nm on silicon substrates, which can be considered as a buffering layer that would not affect the overall shape of the final structures on silicon too much as long as the etching time is long enough.

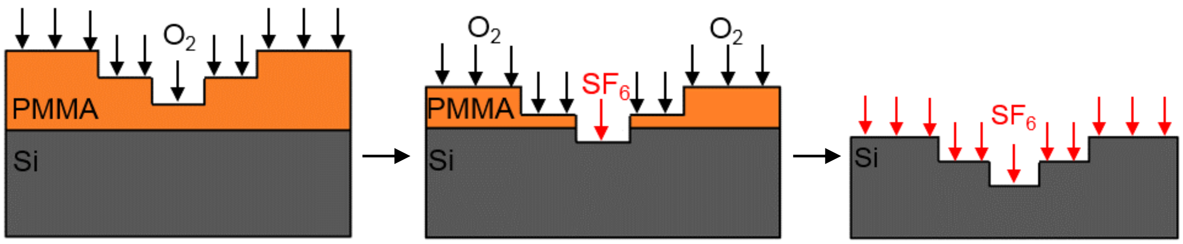

Figure 4.20 Schematics of transfer process of 3D nanostructures from PMMA film to silicon substrate.

In order to control the depths of 3D structures on silicon substrates, etching rates and selectivity should be controlled. Etching rate represents how fast the materials are removed in RIE processes. Etching rate equals the thickness change over etching time. Selectivity is the etching rates ratio of the target material over the mask material. Here is the etching rate of silicon over the etching rate of PMMA. Recipe that used in RIE process should be calibrated to get appropriate etching rates and selectivity. The calibration process is as follows. 1). Spin coating a 100 nm PMMA film on silicon substrates; 2). Scratching the PMMA to get a trench; 3). Etching the sample with a certain recipe for time t. 4). Scratching the remaining PMMA on the same sample but another place to get a new trench. 5). Measuring the depths of the new trench d. 6).Measuring the depths of the original trench D. Therefore, the PMMA etching rate is (d-100)/t. The silicon etching rate is (D-d)/t while selectivity is (D-d)/(d-100).

Factors that affect etching rate and selectivity are power, chamber pressure and gas flow rate. Increasing power always increases the etching rate. Chamber pressure dose not linearly affect the etching rate but should be remained in an appropriate range around 30-70 mtorr. Larger flowrate of O_2 corresponds higher PMMA etching rate and larger flowrate of SF_6 corresponds higher Si etching rate. In order to transfer the 3D nanostructure from PMMA to silicon, an appropriate RIE recipe is critical. Many researchers proposed different approaches to search optimal parameters in RIE processes. Factorial experimental design and fractional Taguchi experimental design are two common approaches. Because of the historical data from the clean room in our university, etching power of 24 W is an experience value the user can adopt. The parameters searching process is simplified to tune the flow rate of the etching gas SF_6 and O_2 in the etching chamber. By measuring the differences between thicknesses after etching and before etching for both two materials, selectivity can be calculated by dividing those two values.

After carefully tuning the parameters of these factors, RIE recipe that can successfully transfer 3D structures and magnify the depth of nanostructures is acquired. The recipe is as follows: Power 24 W; SF_6 18 sccm; O_2 5 sccm; Pressure 40 mtorr. After measurement and calculation, the etching rate of PMMA is 0.77 nm/s. Silicon etching rate is 1.12 nm/s and the selectivity is 1.45, indicating that when 1 nm PMMA is etched away, 1.45 nm silicon is etched at the same time.

4.4.2 Transferring 3D Structures with Magnified Depths

The equipment used is a Semigroup Reactive Ion Etcher. After 3 minutes etching, the PMMA film was completely etched, and 3D nanostructures can be fully transferred on the silicon surface.

RIE etching experiments are performed using a three-step stair-like 3D nanostructure on PMMA, as shown in Figure 4.18 (a). Before RIE etching, depths each step were 9nm, 29nm and 30nm respectively, as shown in Figure 4.18 (c). After RIE etching, the stair-like 3D nanostructures with three steps were successfully transferred onto the silicon substrate, as shown in Figure 4.18 (b). The entire structure on silicon is clean and clear. PMMA debris residue that was not washed away during cleaning process was etched out during the RIE process. Depths of each layer on silicon are around 20 nm, 58nm and 64nm, as shown in Figure 4.18 (d). The surface roughness (Ra) is measured around 7nm. We also tried to transfer relatively complex nanostructures with discrete height levels to silicon substrate. A three-level square cavity structure was fabricated using our nanomachining approach, as shown in Figure 4.19 (a), and then was transferred onto the silicon surfaces by RIE etching, as shown in Figure 4.19 (c). Height differences are about 20nm for each designed levels. Nanostructure transferring process on silicon was successfully implemented with selectivity greater than 1.

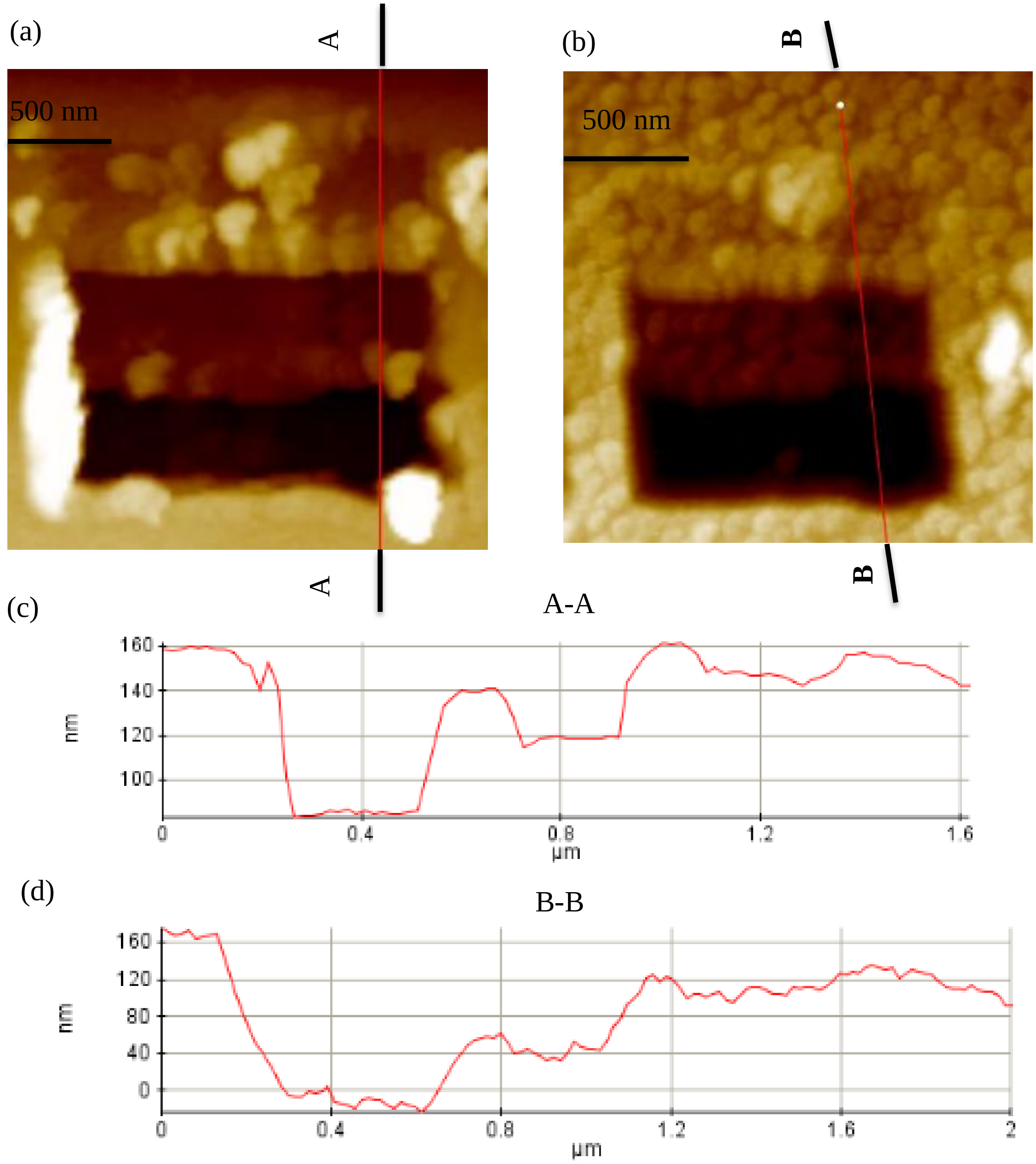

Figure 4.21 (a) A three-step stair nanostructure on PMMA film. (b) The stair nanostructures on silicon substrate after RIE. (c, d) Cross sectional profile of the stair structure on PMMA and silicon, respectively.

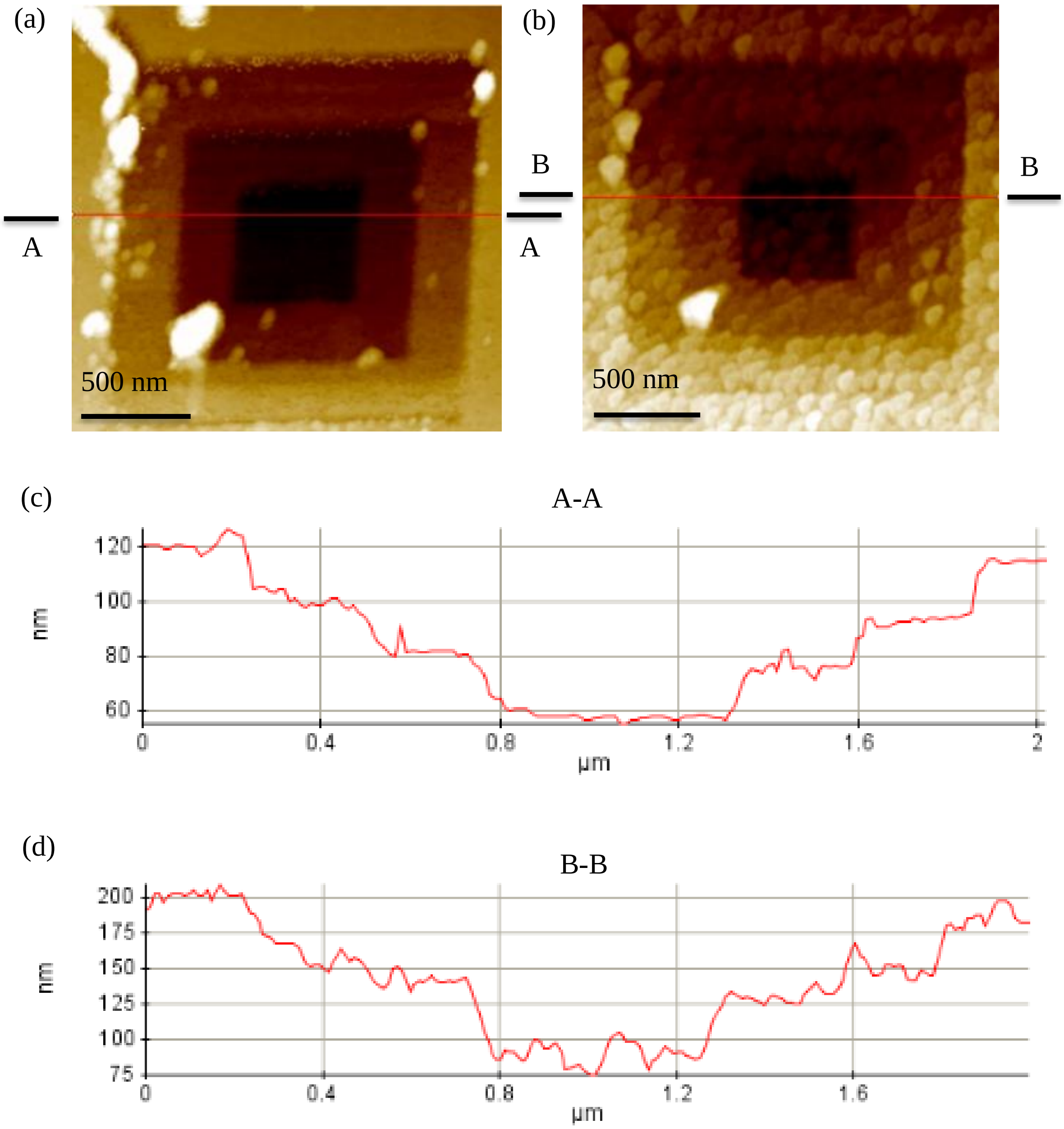

Figure 4.22 (a) Nanostructures with three levels of square cavities on PMMA. (b) Nanostructures with three levels of square cavities on silicon after RIE. (c, d) Cross sectional profile of three levels of square cavities on PMMA and silicon.

4.4.3 Transferring 3D Structures with Shrunk Depths

Increase height differences between layers and decrease selectivity to limit the surface roughness transfer from PMMA to silicon. In order to decrease the selectivity, flow rate of O_2 should be increased. With more O_2, the etching rate of PMMA is increased, which helps decrease the selectivity. With smaller selectivity, roughness on PMMA will not be magnified or will even be suppressed during the etching process. Therefore, surface roughness can be reduced. The entire recipe after increasing O_2 flow rate to 9 sccm is as follows: plasma power is 24 W, flow rate of SF_6 and O_2 are 18 sccm and 9 sccm, respectively. Pressure in the chamber is set to be 40 mtorr. The selectivity of PMMA to silicon is about 0.35 using this recipe, indicating that when 1 nm PMMA is etched away, 0.35 nm silicon is etched at the same time. After 3 minutes etching, the PMMA film was completely etched, and 3D nanostructures are successfully transferred onto the silicon surface.

Figure 4.20 (a) shows a three-step stair-like 3D nanostructure on PMMA is fabricated before RIE etching with depths of 48 nm, 77 nm and 104 nm, respectively. Figure 4.20 (b) shows the nanostructure on silicon after RIE etching, whose depths are 13 nm, 27 nm and 40 nm, respectively. Figure 4.21 (a) and (b) show a three-layer nanostructure with two circular cavities on PMMA and on silicon, respectively. Depths on PMMA are 40 nm, 64 nm and 89 nm, respectively. Depths on silicon are 12 nm, 22 nm and 35 nm, respectively. Figure 4.21 (c) and (d) show the cross sectional profiles on PMMA and silicon. By measuring the Ra of the first layer, I have the original surface roughness (Ra) value of 1.6 nm. By measure the same location of the structure after RIE, I got the surface roughness (Ra) value on silicon of 2.2 nm.

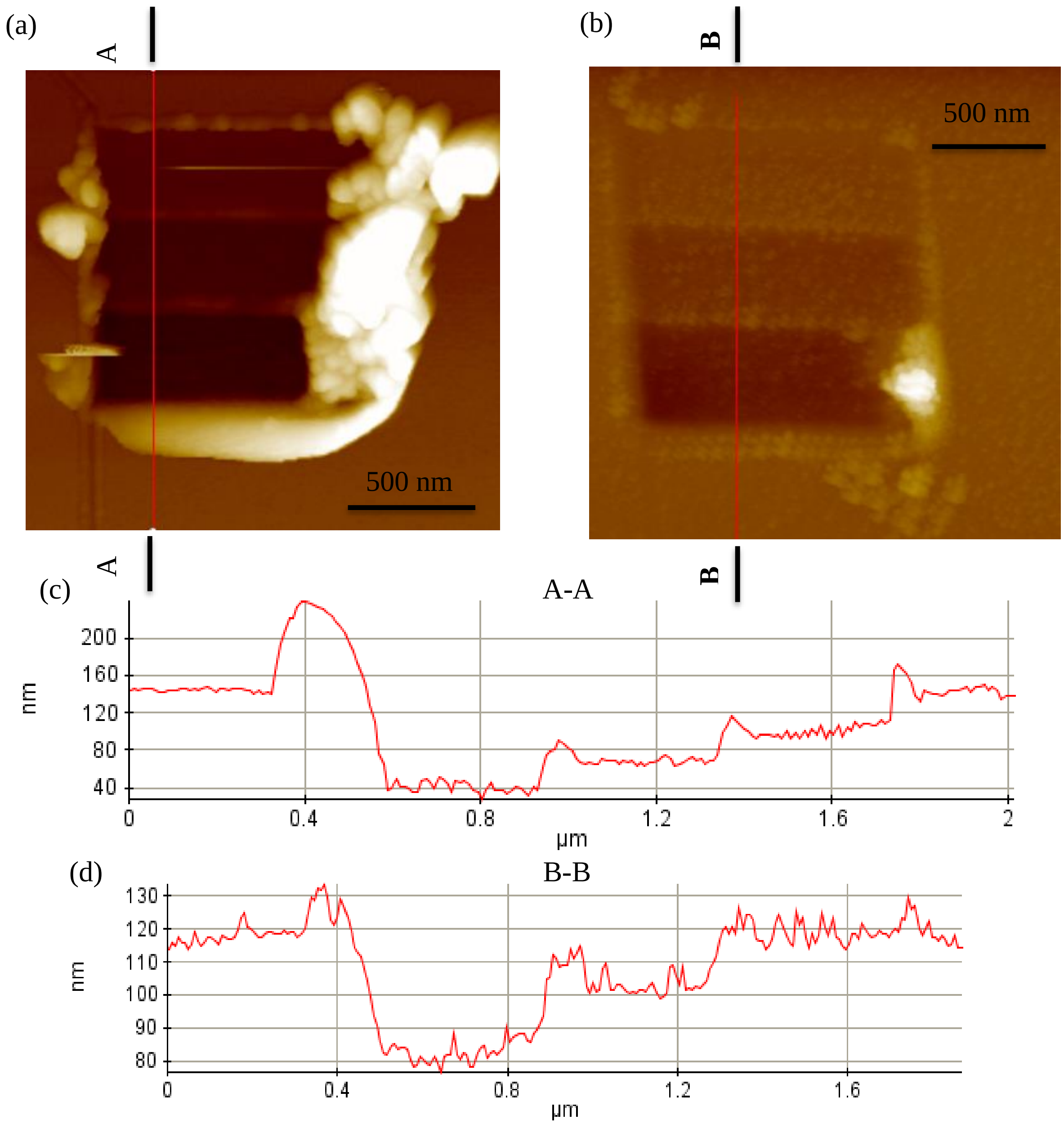

Figure 4.23 (a) A three-step stair nanostructure on PMMA film. (b) The stair nanostructure on silicon substrate after RIE. (c, d) Cross sectional profile of the stair structure on PMMA and silicon.

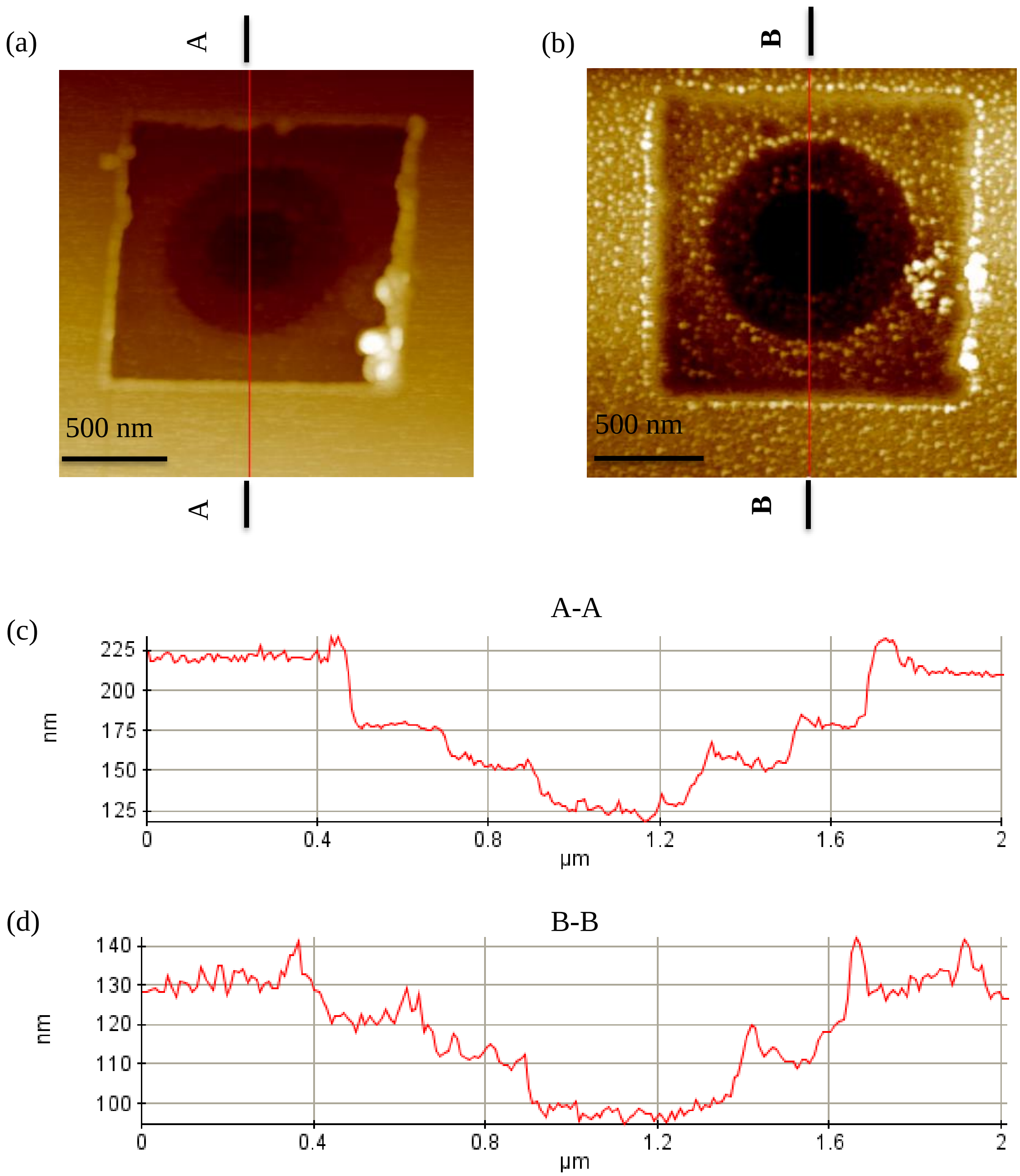

Figure 4.24 (a) Three-layer nanostructure with two circular cavities on PMMA. (b) The three-layer nanostructure with two circular cavities on silicon after RIE. (c, d) Cross sectional profiles of the three-layer nanostructure with two circular cavities on PMMA and silicon.

4.4.4 Conclusions of Transferring 3D Structures

The above results demonstrate good fidelity of transferring 3D nanostructures from PMMA to silicon surfaces. Depths and surface roughness of 3D nanostructures on silicon are controllable by selecting a corresponding recipe and tuning the flow rate of O_2. In transferring nanometer scale 3D structures, it is recommended that using relative small power (20 to 40 W) so that the process has slower reaction rate, which is easier for users to control. We can either magnify or shrink the depths of 3D nanostructures from PMMA surfaces on to silicon surfaces. By increasing the oxygen flow rate in RIE process, the height of nanostructures is decreased due to a greater PMMA consuming rate. By decreasing the oxygen flow rate in RIE process, the height of nanostructures can be increased due to a smaller PMMA consuming rate. After identifying a region of recipe for RIE etching including the selectivity of 1, increasing the O_2 flow rate helps decrease the selectivity of RIE etching process, resulting a smaller depths nanostructure with smoother surface, and vice versa.

4.5 Chapter Summary

The results of fabricating 3D nanostructures using ultrasonic assisted nanomachining in both setpoint force mode and z-height control mode are shown and discussed. 3D nanostructures with complex contours and discrete and continuous height changes are fabricated and cleaned. The advantages and disadvantages are compared between these two control mechanisms. Furthermore, the 3D nanostructures were further transferred from PMMA surfaces onto silicon surfaces with tunable selectivity and controllable surface finishes.

CHAPTER 5 APPLICATIONS BASED ON THE PROCESSES

Previously, 3D nanofabrication processes are developed based on the novel ultrasonic vibration assisted 3D nanomachining. Applications based on the nanofabrication processes will be discussed in this chapter. I present applications of implementing low-cost and high-throughput 3D nanofabrication processes by combining complementary soft lithography techniques. In addition, I fabricated SERS substrates that can greatly enhance the intensity of Raman scattering used for chemical detection.

5.1 Fabrication of Masters in Soft Lithography

Low throughput is always a limitation in AFM-based nanolithography processes, especially in the 3D nanofabrication processes discussed before. In this section, soft lithography techniques are combined with the 3D nanomachining processes to fabricate 3D nanostructures.

Soft lithography is a micro/nano scale patterning technique that is able to generate 2D/3D nanostructures on flat or even curved surfaces with low cost and high throughput. An elastomeric stamp, usually PDMS, is used in printing and molding processes. Masters, however, are required as original molds to duplicate reversed patterns on PMDS. Usually, researchers adopted two main nanofabrication techniques to fabricate masters: photolithography and e-beam lithography. However, these two methods have their own limitations in fabricating 3D nanostructures. Photolithography is a widespread technique of fabricating 2D patterns. However, there are some limitations to apply this technique. First, photomasks are required to project light onto photosensitive resists coating on substrates.

Although photomasks can be designed and purchased commercially, the time, cost of design, fabrication, and mailing of the photomasks is significant, which prohibit a low-cost and rapid prototyping of test structures. Second, the cost of the masks used in photolithography, the process itself and the clean room requirement limits the accessibility for some researchers. Moreover, it is extremely difficult to produce 3D structures, not mention in nanoscale. As for e-beam lithography, although it is able to fabricate 3D nanostructures with high versatility, the extremely high cost of the equipment and maintenance limits a large number of users.

Ultrasonic assisted nanomachining processes discussed previously are low-cost, user-friendly and flexible approaches that can be used in fabricating masters for soft lithography. Combined with RIE techniques, the 3D nanostructures fabricated on PMMA surfaces can be transferred onto silicon substrates with magnified or shrunk vertical dimensions. This results a rigid master with longer lifetime on silicon surfaces. As a maskless lithographic nanofabrication process, it is easy to fabricate and tune the dimensions of complex 2D/3D relief nanopatterns on polymer films. Therefore, it helps further reduce the cost of soft lithography since no masks is required in photolithography and no capital intensive e-beam lithography machine is needed.

The schematic illustration of two soft lithography processes is shown in Figure 5.1. The first step is to design bitmap image patterns and apply the ultrasonic vibration assisted nanomachining process on PMMA films. The nanostructures fabricated on PMMA film can be either two-dimensional or three dimensional, depending on the functionality the application requires. If the patterns are two dimensional, the microcontact printing (μCP) process can be

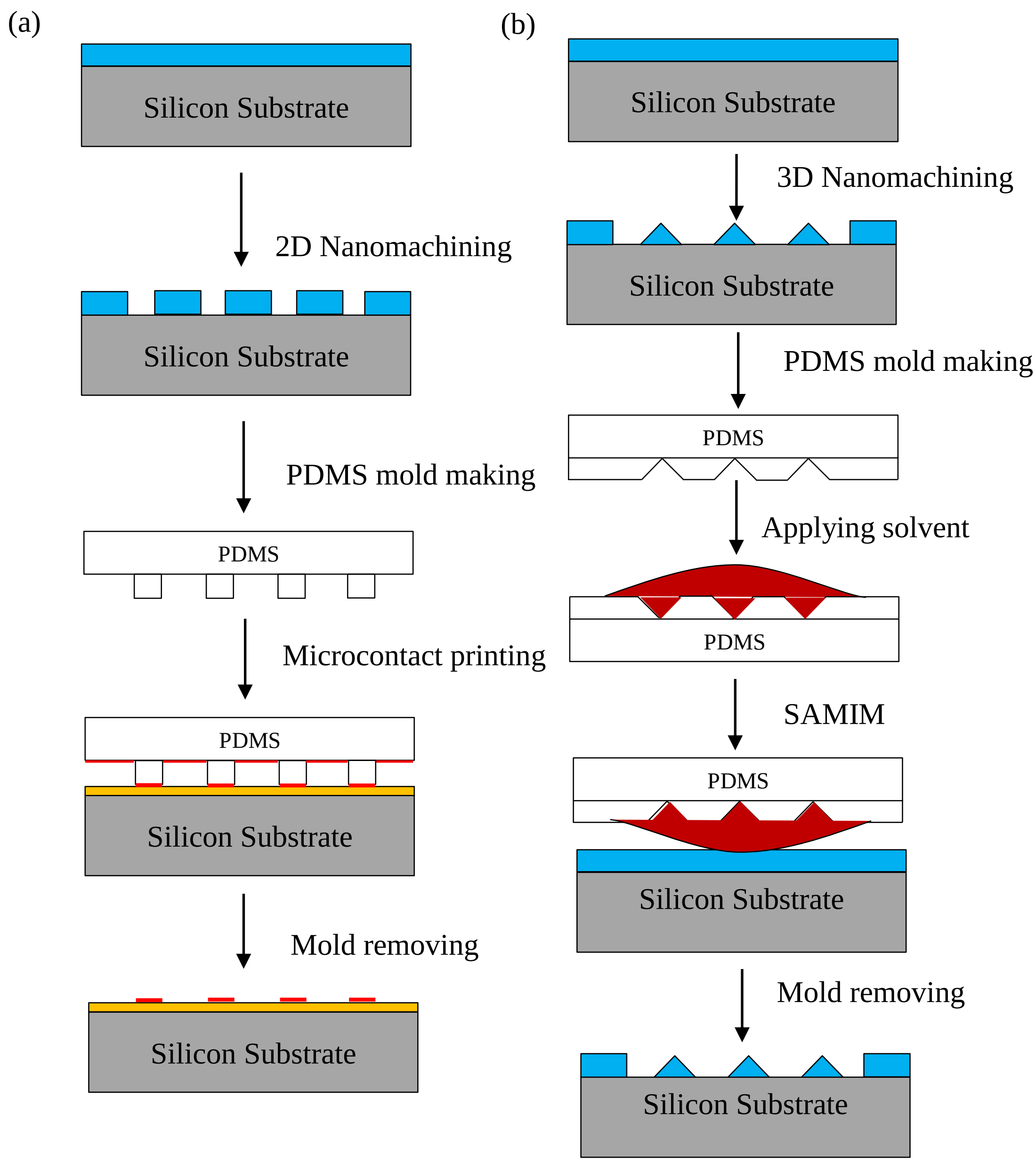

Figure 5.1 Schematic illustration of (a) microcontact printing (μCP) process and (b) solvent-assisted microcontact molding (SAMIM) process

adopted to mass-produce the pattern by immersing the PDMS mold into self-assembled monolayer (SAM) to form a pattern defined by previous steps. If the patterns are three dimensional, solvent-assisted microcontact molding (SAMIM) process can be adopted as the low-cost and high-throughput technique. By removing the excess prepolymer dropped on the PDMS mold, three-dimensional nanostructures forms on the cavities of the PDMS mold. After placing the fulfilled PDMS mold on a substrate, three-dimensional nanostructures are produced on substrates for further processes or for functional purpose.

I fabricated 3D nanopatterns by ultrasonic vibration assisted nanomachining processes and then PDMS molds are fabricated to get the reverse pattern of the 3D nanopatterns. After that, I transfered the reverse pattern of 3-layer circles on PDMS onto new PMMA surfaces using the 3D Nanopatterning technique SAMIM.

3D nanostructures such as 3-layer circles and "ise" logos are fabricated. After effectively cleaning the 3D nanostructures after machining, I am able to combine the nanoimprint lithography techniques in the nanofabrication. Reversed structures can be fabricated on PDMS (Dow Corning Sylgard 184) by molding processes. The procedures of making the PDMS molds are as follows. First, weighting 1 g curing agent and 10 g base in a small clean cup and fully mixing them. Make sure the base and curing agent are 10: 1 ratio. The weight can be doubled to make sure that the thickness of the stamp is in the range of 0.5-1.0 cm. Second, pouring the well-mixed material in a small petri dish with the patterned sample double side taped on the bottom. Third, degassing the PDMS for 20 min in a vacuum desiccator (SP SCIENCEWARE, Inside Dia.: 6-3/4"/17.145 cm). At the same time, using a glass slide with suitable size as the holder of the mold. Fourth, curing the PDMS on the hotplate for 7 hours with 80 °C curing temperature. Then, putting it in a freezer for a few minutes, which will shrink the PDMS slightly and will be easier for me to demold without degrade the structures on PDMS. Finally, carefully separate the PDMS from a side of the mold wall so the rest of it could be pulled gently and perpendicularly out of the petri dish. If trimming after the pull out is needed, carefully cut or trim the final PDMS mold.

Figure 5.2 shows four identical 3-layer patterns on PMMA, fabricated by the previous developed nanomachining process under z-height control. After nanoimprint lithography, the reverse protruding 3D nanostructures are fabricated. The overall depths of the nanostructures are about 87 nm. Patterns on PDMS have the height of 82-83 nm, as shown in Figure 5.3. Besides the 3-layer pattern, three "ise" logos are fabricated on PMMA with different base depth, as shown in Figure 5.4 (a). The reversed patterns are successfully molded on PDMS, as shown in Figure 5.4 (b). These results fully demonstrated the capability and flexibility of 3D nanofabrication after combining the developed 3D nanofabrication processes with the molding processes using PDMS. The fidelity of the PDMS molds play an important role in the following steps as shown in Figure 5.1. As shown in Figure 5.3, the connecting line with 10 nm depth and 200 nm width is reflected on the PDMS mold, which demonstrated the fidelity of the mold. A good characteristic of nanomachining using AFM is that the shape of the AFM tips are the contours of the walls in the pattern on PMMA. The angle brought up by the AFM tips make the demolding process smooth. E-beam lithography doesn't have this superior releasing angle since there is a forward scattering effect.

(a)

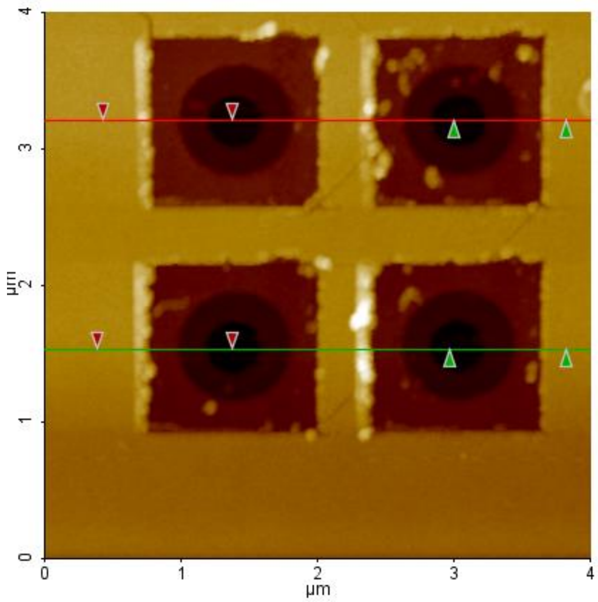

(b)

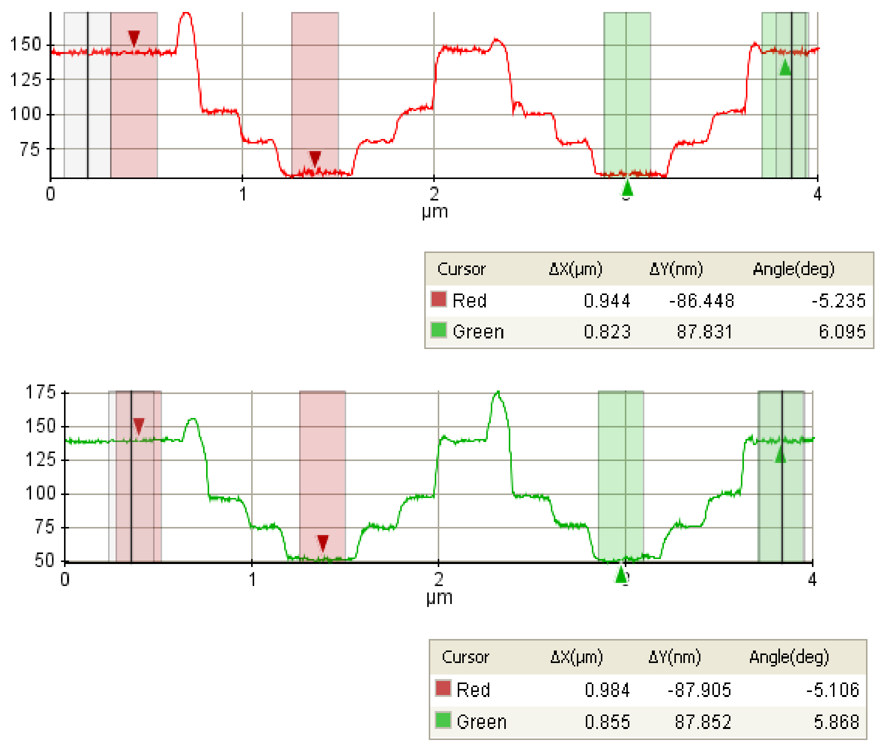

Figure 5.2 (a) AFM images and (b) cross-sectional profiles of nanostructures fabricate on the PMMA surface using the fabrication technique I developed before.

(a)

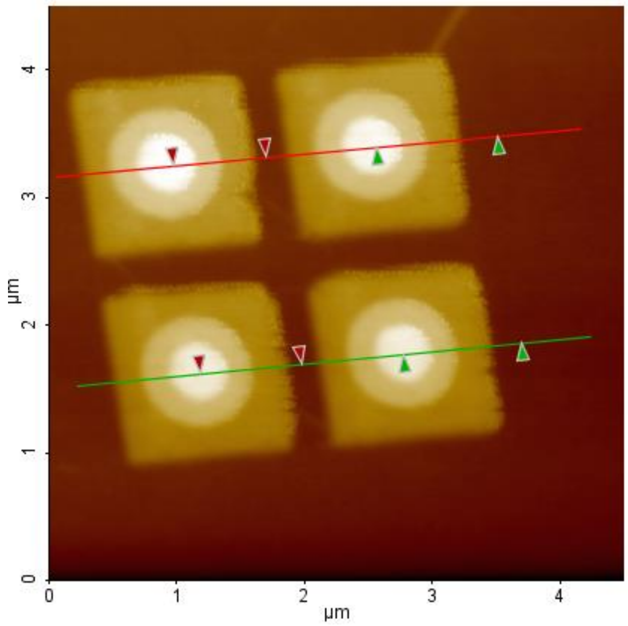

(b)

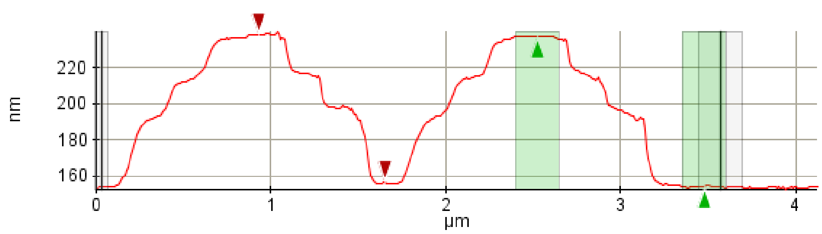

Cursor	ΔX(µm)	ΔY(nm)	Angle(deg)
Red	0.722	-81.946	-6.472
Green	0.955	-83.196	-4.980

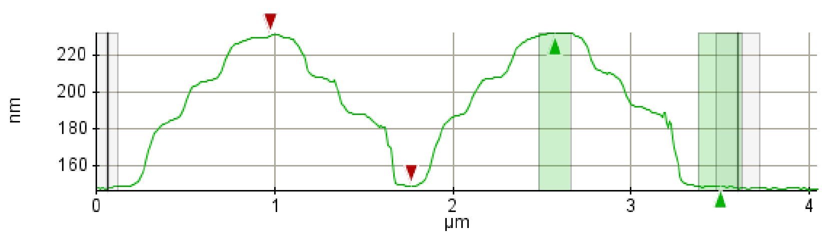

Cursor	ΔX(µm)	ΔY(nm)	Angle(deg)
Red	0.790	-81.871	-5.917
Green	0.928	-83.344	-5.130

Figure 5.3 (a) AFM images and (b) cross-sectional profiles of reversed protruding nanostructures after molding process using PDMS.

(a)

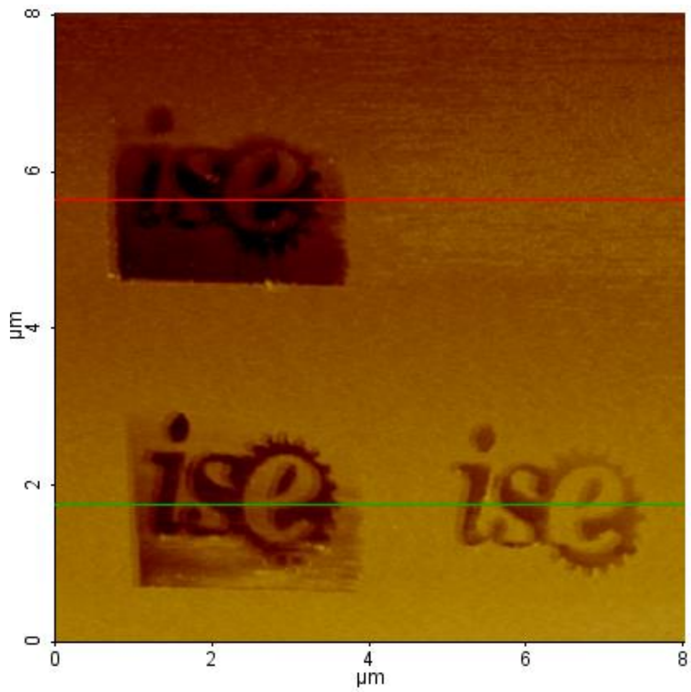

(b)

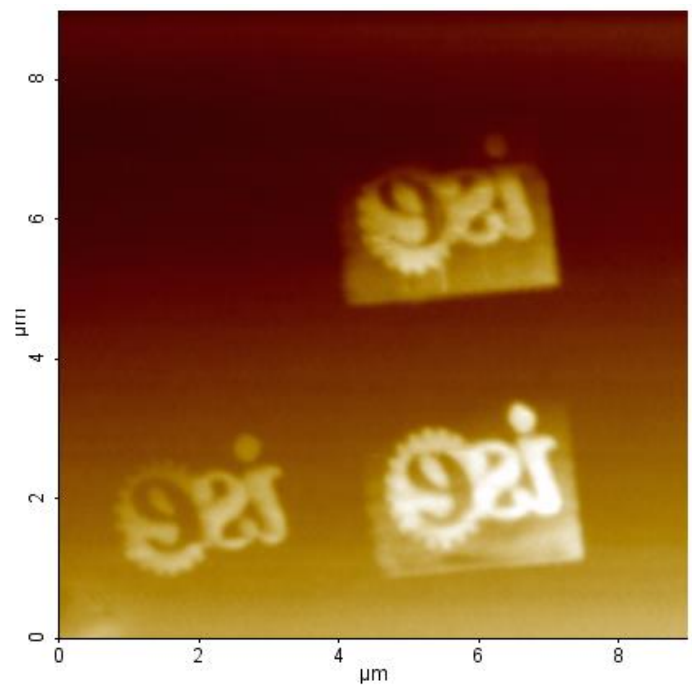

Figure 5.4 Nanostructures of “ise” fabricated by (a) the AFM-based nanomachining process and by (b) PDMS reverse molding process.

I am also curious about the reusability of the PMMA mold. I consecutively molded the patterned PMMA sample, shown in Figure 5.2, for three times. All AFM images after three molding processes are shown in Figure 5.5. Including the original pattern, four cross-sectional profiles are overlapped together to compare the fidelity of the PMMA nanostructures after multiple moldings. As we can see from the overlapped cross-sectional profiles, shown in Figure 5.5, the sharp corners of each layer on the 3D nanopatterns are getting blunt as more reversed PDMS are fabricated. That means more residual PDMS sticks on the PMMA pattern as more moldings are finished.

After successfully fabricated the PDMS mold, many following techniques can be applied. I chose to apply SAMIM. The procedures are as follows. First, drop acetone to the patterned surface of the PDMS mold fabricated before and contact it with the PMMA substrate films for 5 min. In this process, the acetone will not spread on PDMS until it contact with the PMMA. Second, remove the residual acetone completely by baking the sample on a hotplate at 60 °C for 5 minutes. In this process, the PMMA underneath is dissolved in the acetone and the gel-like PMMA in acetone will conform the 3D shape on the PDMS mold. After removing the acetone solvent, the reversed pattern is formed on the new PMMA surfaces. Figure 5.6 (a) shows the optical image of the PMMA surfaces after the SAMIM process. If the amount of acetone is not enough, the PMMA will not be effectively solved. Figure 5.6 (b) shows the result after SAMIM process on PMMA. It replicates the overall shape from the PDMS, but the cross-sectional profile gives the overall depth around 30 nm, shown in Figure 5.6 (c). The surfaces of each layer is not flat as the pattern on PDMS. There are rooms to improve this process.

(a) (b) (c)

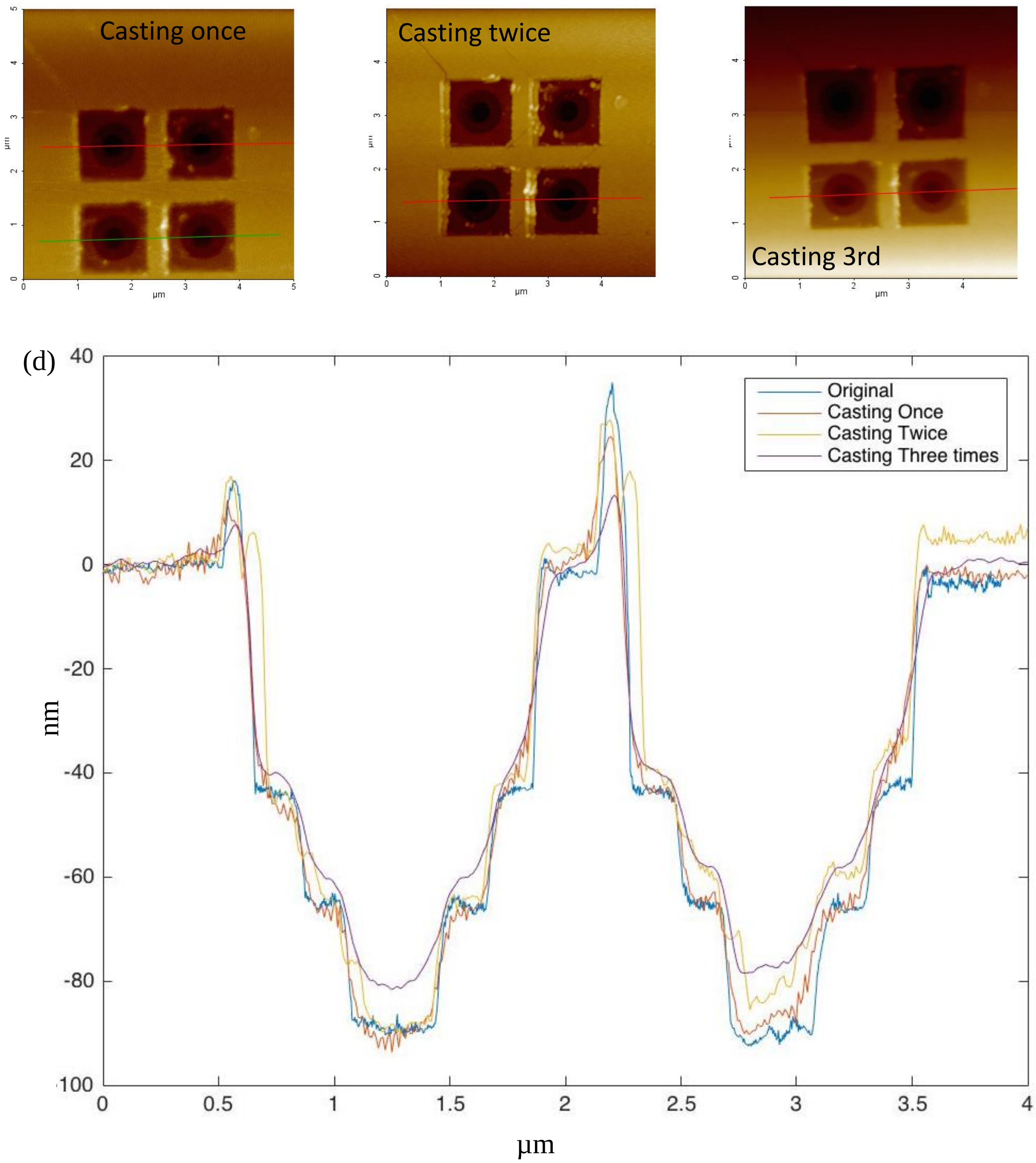

Figure 5.5 Patterned PMMA after molding process (a) once, (b) twice, and (c) three times. (d) Cross-sectional profiles of the original PMMA pattern without molding and molding one to three times.

(a)

(b)

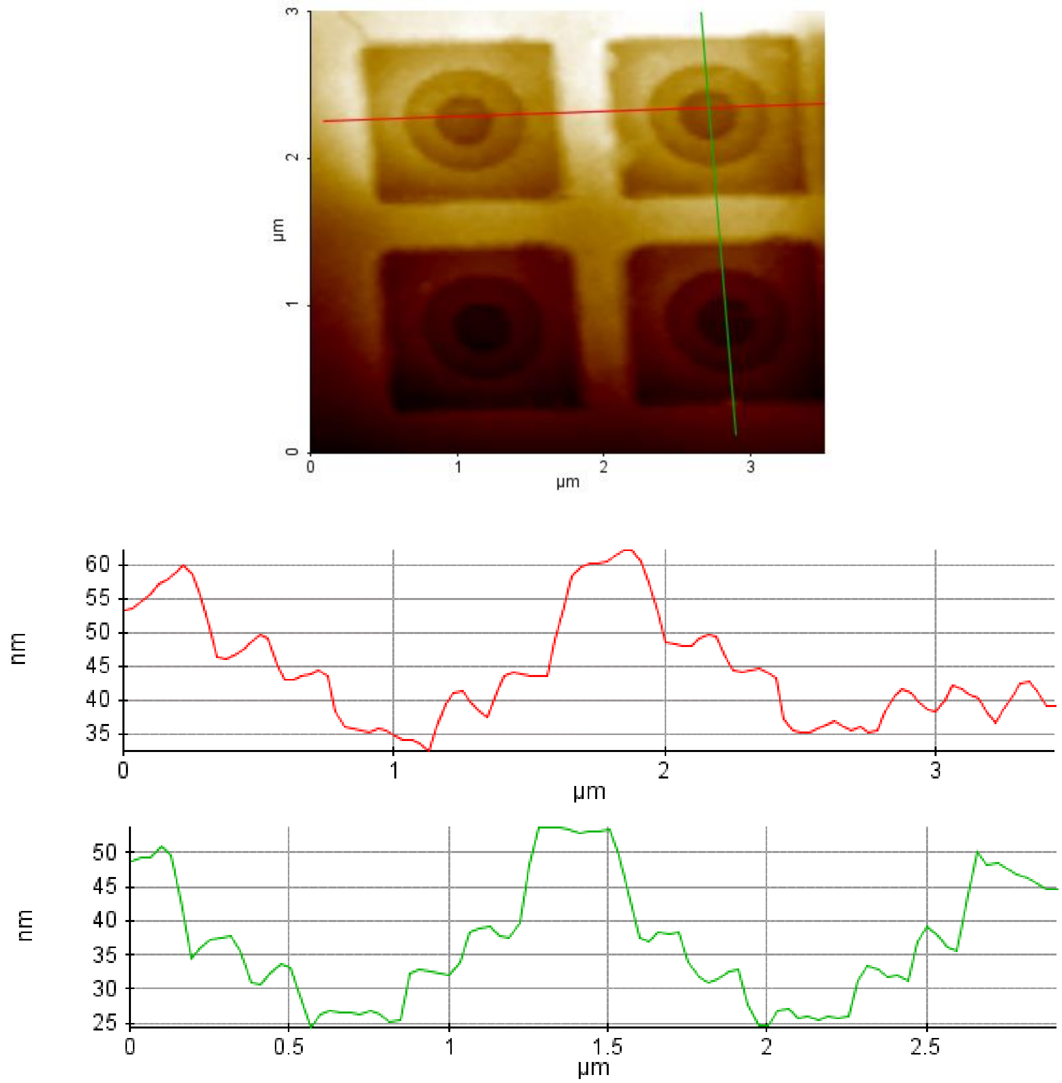

Figure 5.6 (a) AFM image of patterned PMMA surface using SAMIM. (b) Cross-sectional profile of the result on the PMMA surface.

5.2 Fabrication and Detection of SERS Substrates

SERS is surface enhanced Raman spectroscopy, a surface-sensitive detection technique that enhances Raman scattering using metal substrates with featured structures. It dramatically increases the scattering signals of the analytes with enhancement factors (EFs) of 10^4-10^8 over traditional Raman scattering due to electromagnetic and chemical mechanisms. In order to utilize SERS, low-cost and high-throughput fabrication of SERS substrates with reproducibility and large Raman enhancement is a prerequisite. Although high EFs have been observed from substrates with different structures such as nanosphere, nanorods and nanohole, SERS requires substrates with structures that are easily tuned as well as reproduced, which requires nanofabrication approaches for precise, repeatable, low-cost and high-throughput metallic nanostructures. However, SERS substrates reported in literature are fabricated by several complex processes, which are not cost-effective and time-consuming. The novel nanomachining processes we present previously demonstrated that it is possible to fabricate trenches with controllable widths and depths. Squares with tunable size and periodicity is able to increase the intensity of the Raman scattering.

In this subsection, I will first describe the experimental details and procedures. After that, I will show the fabricated patterns on PMMA and results after coating. After fabricating the SERS substrates, enhancement factors will be calculated to demonstrate their functionality. Different patterns will be compared in terms of the intensity of Raman scattering.

Figure 5.7 shows the flow chart for fabricating SERS substrates and detecting probe molecules. Following this chart, the SERS substrates could be fabricated and the intensity of

Raman scattering will be detected and calculated. The detailed procedures are described as follows. First, getting an 80 nm PMMA thin layer on silicon substrate. The PMMA used here is 950 A2 PMMA under 4000 RPM. After spinning coating, I need to remove the remaining solvent by baking the sample on 180 °C hot plate for 90s. The reason of getting 80 nm other than 200 nm PMMA is to reduce the thickness of residual layer after the nanomachining process and thus make the following RIE process easier. After coating the PMMA, a water-soluble PVA layer as described in Chapter 3 is deposited to help remove the debris created in the nanomachining process. Second, Fabricating desired nanostructures on PMMA layer.

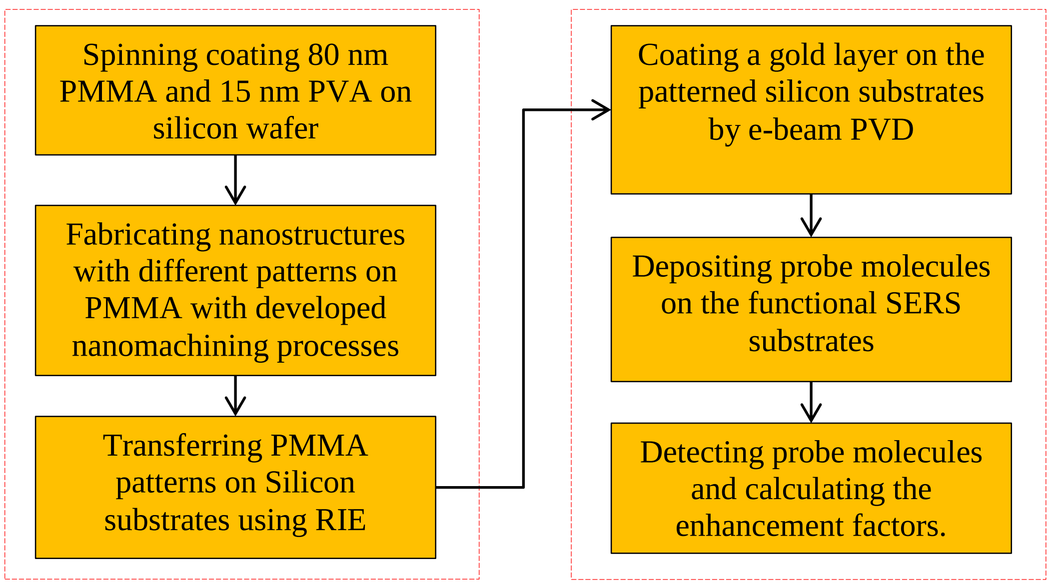

Figure 5.7 Flow chart for fabricating SERS substrates and detecting probe molecules

Third, transferring the pattern on PMMA onto silicon surface using a recipe that could magnify the depth as much as possible. After calibration, I got a recipe that is able to achieve 10:1

silicon to PMMA selectivity. That means the depth on PMMA could be magnified 10 times. The recipe is 40 W power, 150 mtorr chamber pressure, 30 sccm SF6, 20 sccm CHF3. The RIE equipment I used is Oxford Plasmalab 80 Plus. Under this recipe, the PMMA etch rate is 8 nm/min and the silicon etch rate is around 80 nm/min. Fifth, after getting a silicon pattern, I could use PDMS molding technique to get a reverse pattern as SERS substrate after coating a gold layer, or directly deposit a gold film on the pattern. Usually, I use 2-20nm adhesive layer, Chromium or Titanium, between the silicon and the gold. The thickness of the deposited gold film is 80 nm. At this stage, the SERS substrate is successfully fabricated and ready to use. The last two procedures are depositing molecules on the SERS substrates and detecting the intensity of Raman Scattering from the chemical bonds of the probing molecules after exposing under an incident laser using a Raman microscope. The wavelength of the laser is 633 nm.

Three sets of experiments are conducted to investigate the function of patterns for the Raman scattering intensity. The first set of experiment is to investigate the SERS substrates of the gold-coated PMMA nanostructures with less than 100 nm feature depths. The second set is to investigate the SERS substrates of the gold-coated silicon structures. The structures are transferred from PMMA with a 10 times larger depths. The last set is to investigate the SERS substrates of gold-coated PDMS patterns, which are reversed silicon patterns in the second set of experiments.

5.2.1 SERS Substrates of Gold-Coated Patterned PMMA

The first set of experiments is to compare the flat gold surface, the gold-coated PMMA surface patterned by parallel lines, and the gold-coated PMMA surface patterned by grids nanostructures. After physical vapor deposition, the surface roughness (Ra) of the flat surface is 6 nm, and the cross-sectional profiles are shown in Figure 5.8 (c). Figure 5.8 (a) shows the AFM images of the flat, line patterned, and grids patterned gold surfaces. The cross-sectional profiles and images of the patterns before and after gold coating are shown in Figure 5.9 and 5.10. The lines and grids have designed depth of 80 nm, although some of the features are covered by debris on purpose. The pitch value is 910 nm, meaning the distance between two adjacent lines is 910 nm. The trench is composed of 5 lines with designed 250 nm width and 80 nm depth.

After fabricated the SERS substrates by coating 80 nm gold on the patterned PMMA, the probing molecules of Rhodamine B is dispensed on the surface. The Rhodamine B with 10 uM concentration is solved in water. A drop of the liquid about 25 uL is placed on the effective area of the sample. After the solvent evaporated after 2 hours, the sample is detected in a Raman microscope (HORIBA HR). The intensity of the 633 nm laser is set as 1mW. The laser spot size is about 5 µm. The integration time is 10s. The optical lens used has the magnification ability of 100x.

The raw Raman scattering signals after detection on the flat, line patterned, and grids patterned gold surfaces are shown in Figure 5.11.It shows the comparison of all three signals on grids patterned Au (the blue line), lines patterned Au (the green lines), and flat Au (the red line). To quantify the results, I measured the ratio of signal intensity at 1190 cm^{-1}. The peak counts of gold-coated grids-patterned PMMA and gold-coated line-patterned PMMA are 1097 and 331, respectively. Almost no signal on the bare flat gold-coated PMMA surfaces.

Therefore, the grids pattern enhanced the signal intensity by a factor of 3.3 compared with the gold-coated line-patterned PMMA surface. These results demonstrate the effectiveness of the fabricated SERS substrates using the novel 3D nanomachining process.

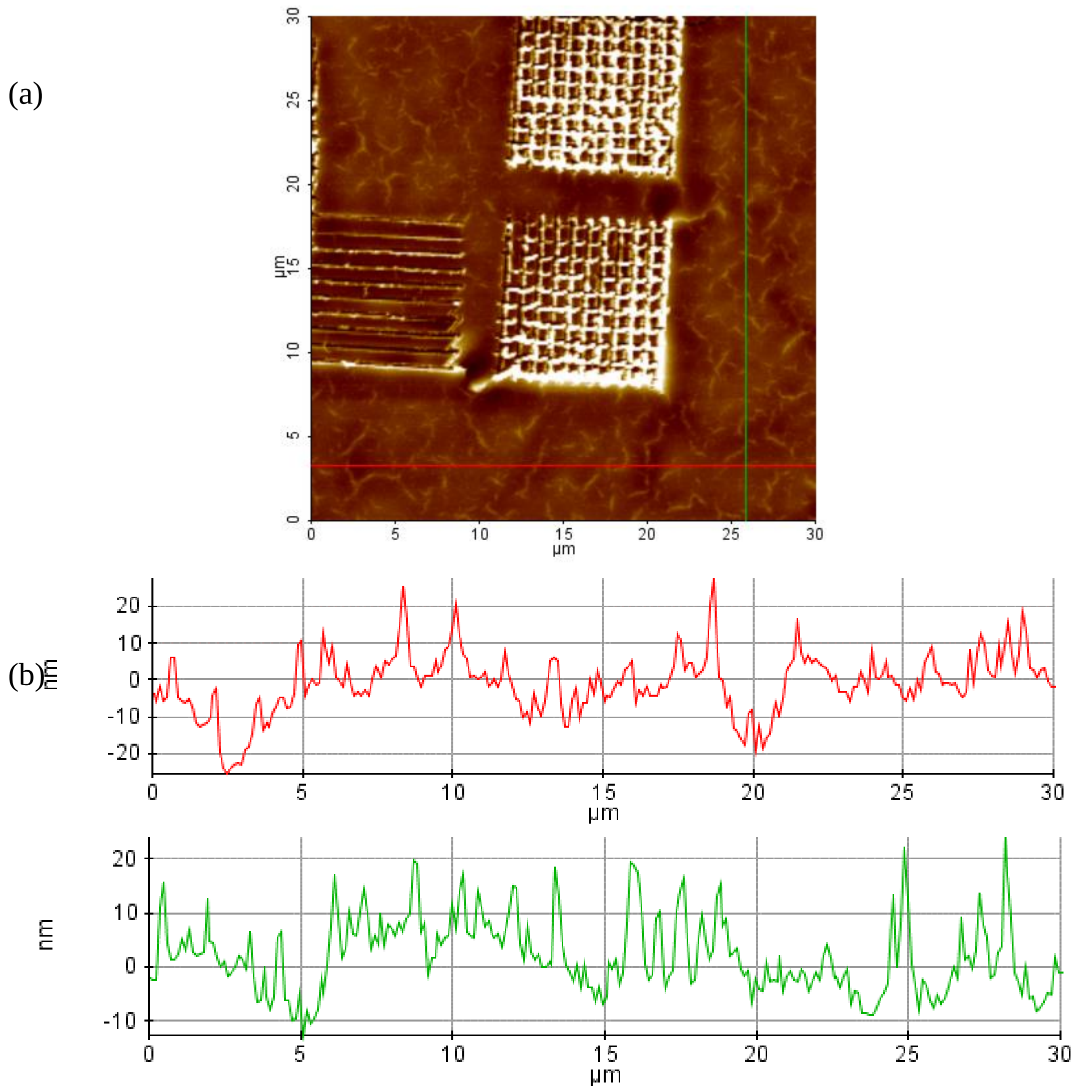

Line	Rpv(nm)	Rq(nm)	Ra(nm)	Rz(nm)
Red	52.836	8.335	6.152	42.534
Green	36.593	7.011	5.634	30.881

Figure 5.8 (a) The Au coated patterns results checked in AFM. (b) Surface roughness and cross-sectional profiles of Au films on silicon.

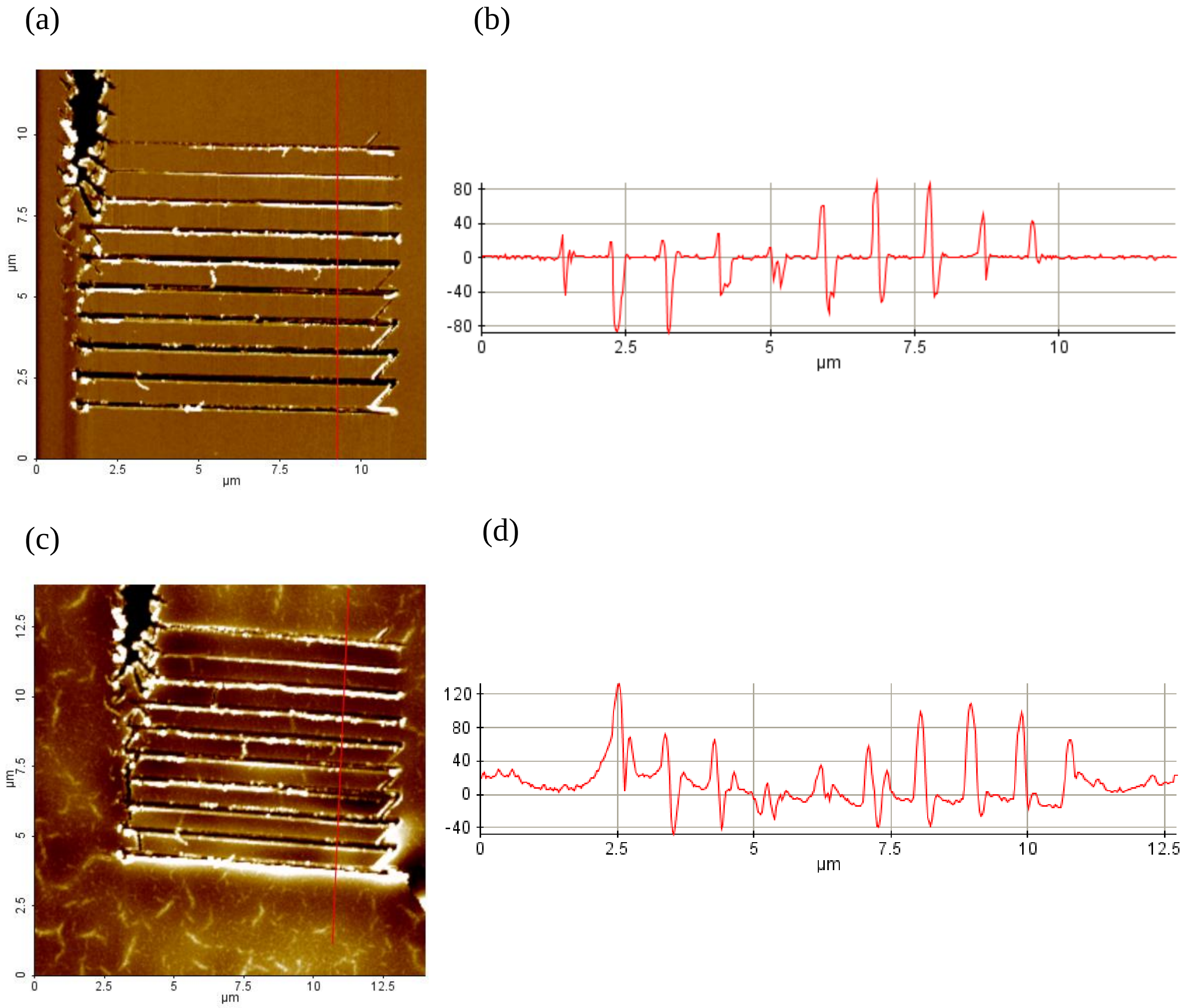

Figure 5.9 (a) Line patterns on PMMA and its (b) cross-sectional profile. (c) The line pattern coated with an 80 nm Au film and its (d) cross-sectional profile.

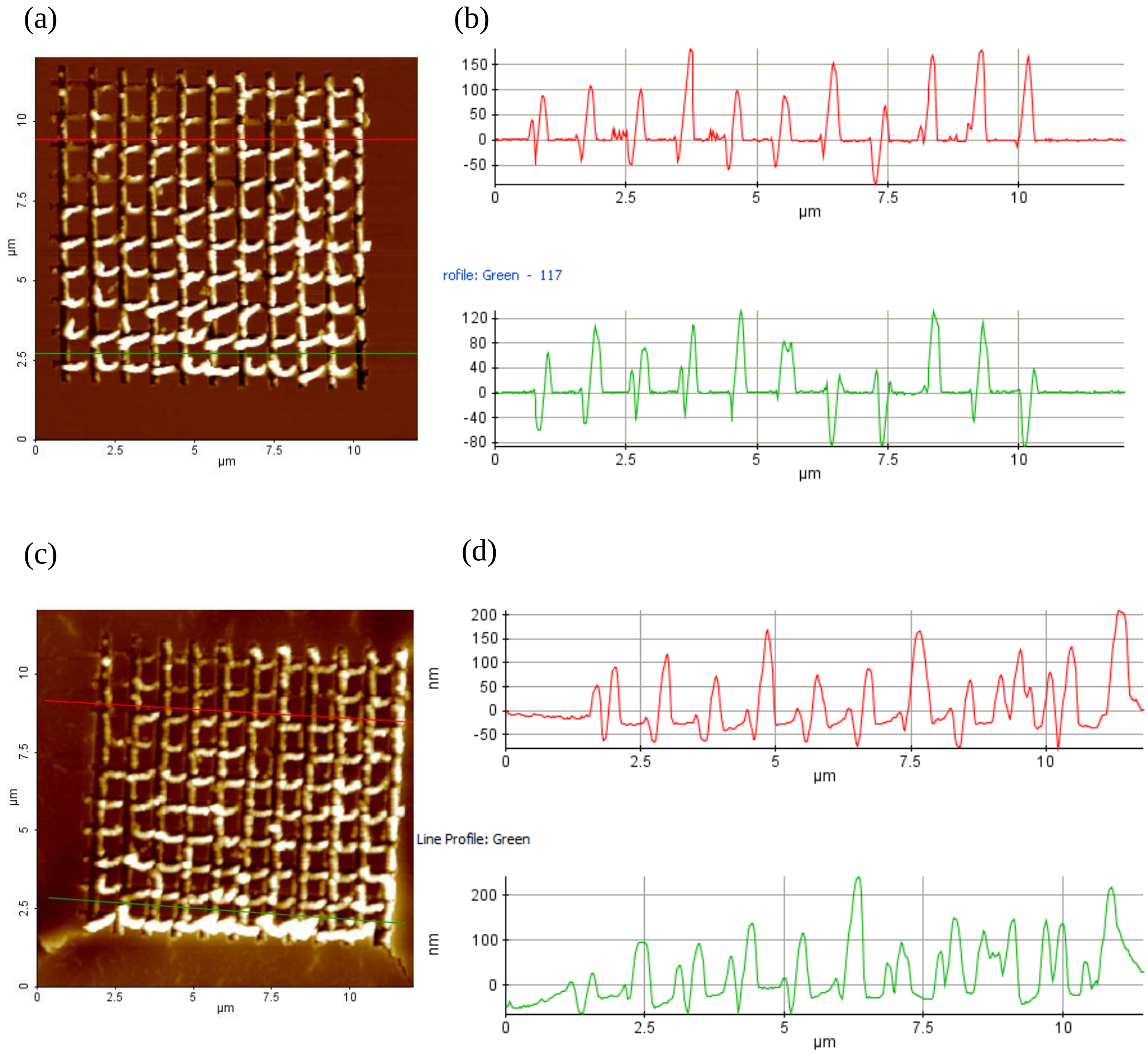

Figure 5.10 (a) Grids pattern on PMMA and its (b) cross-sectional profile. (c) The grids pattern coated with an 80 nm Au film and its (d) cross-sectional profile.

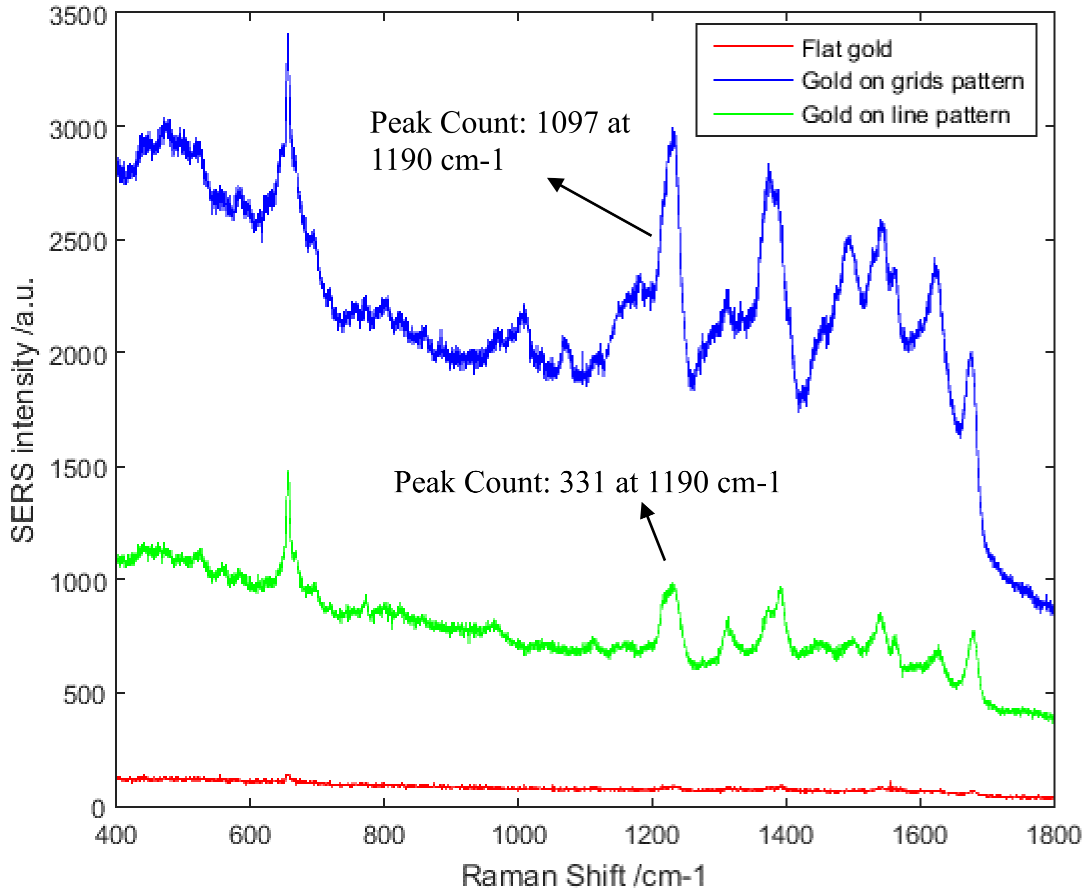

Figure 5.11 SERS signal of grids pattern on Au (Blue) vs. lines pattern on Au (Green) vs. no pattern on Au (Red) using Rhodamine B as probing molecules.

After this set of comparison experiments, another gold-coated grids-patterned PMMA with the same dimension was fabricated to demonstrate the consistency of the effectiveness as a SERS substrate. Figure 5.12 (a) shows the SERS substrate after nanomachining and PVD gold coating. The peak count at 1190 cm^{-1} of patterned area is 730. The results demonstrated that the patterned area has an enhancement effect of signal intensity.

(a)

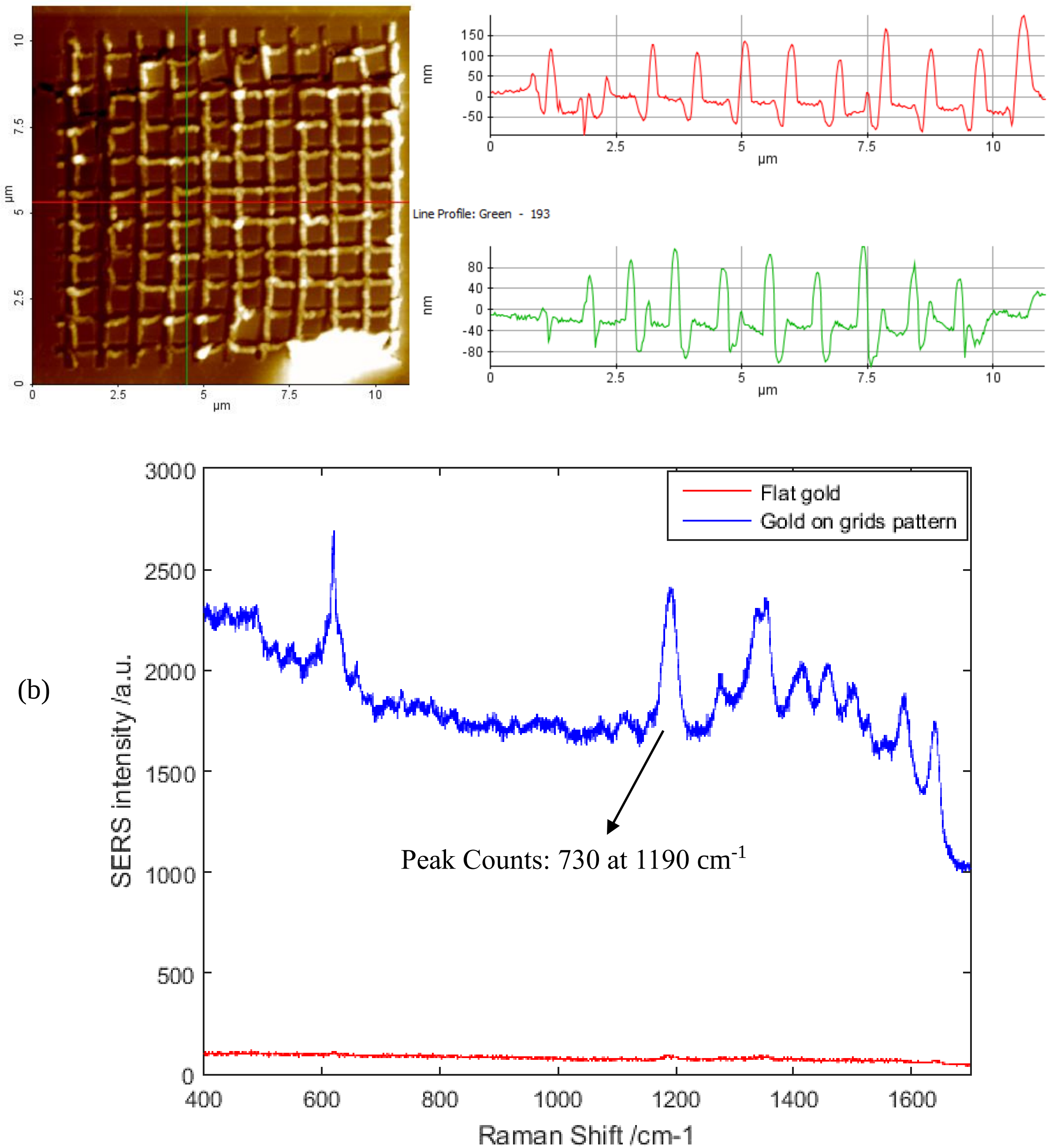

(b)

Figure 5.12 (a) rids pattern after gold coating AFM image and cross-sectional profiles. (b) SERS signal from gold-coated grids pattern (blue line) and gold-coated flat PMMA (red line) using Rhodamine B as probing molecules.

5.2.2 SERS Substrates of Gold-Coated Patterned Silicon

After investigating the effect of SERS substrates using PMMA with gold coating, the results show that the grid pattern is better than the line patterns. Therefore, I fabricated four grids patterns and transferred them onto silicon using RIE. The recipe I developed for RIE could achieve a 10:1 selectivity of silicon to PMMA. These four patterns are shown one by one from Figure 5.13 to Figure 5.16 consecutively. In these four figures, (a) shows the PMMA pattern and its cross-sectional profiles after nanomachining and cleaning process, (b) shows the silicon pattern and its cross-sectional profiles after RIE, (c) shows the gold-coated silicon pattern after PVD, and (d) shows the three-dimensional image of the gold-coated silicon pattern. The cross-sectional profiles after coating 80 nm on silicon are similar with that of no coating, so they are not shown in these four figures.

The first pattern has gradually increasing feature depths from 40 to 80 nm from the top left corner to the bottom right. The designed pattern has the same pitch with that in the previous subsection. The tapered pillars have the top widths around 660 nm, since the pitch value between two adjacent parallel lines is 910 nm. The trench is composed of 5 lines with designed 250 nm width and 80 nm depth.

In the RIE process, the first stage is shifting stage. In this stage, the PMMA pattern down before there are any reaction between the reactive gases and the silicon substrates. The second stage is selecting stage. The PMMA acts as the protection layer of the silicon from active free radicals. After RIE, the bottom right area on the silicon forms pins and the top left area maintains the tapered pillar shape. The reason may be that the PMMA in the second stage are consumed and gradually lose the protection capability from outside to the center of the covering area, which can be seen from the top left area that the trench became wider after RIE. After fully removing the PMMA protection layer, the silicon tapered pillars have the same height as the original surfaces. If the RIE continues, tapered silicon pillars are etched without protection and became shorter than the original surfaces.

This also explains the pin arrays forms on the second pattern. The pitch value of the second pattern is 0.6 times that of the first pattern, and other designs are all the same. That means the tapered PMMA pillars have the width around 396 nm on the top. These four PMMA patterns are fabricated on PMMA with the same thicknesses around 80 nm. Therefore, the etching continues as the PMMA are all consumed and forms the pin arrays with smaller height than that in the first pattern.

Comparing the third pattern with the first pattern, the pitch values are the same. The only difference is the depth. With thicker residual layers, the second selecting stage last shorter than that of the first pattern, which means the depth is shallower and the top of tapered pillars are maintained as squares. The fourth pattern has the 0.8 times of the pitch values of the first pattern, the depths are around 40 nm. And the patterns on the silicon are still tapered pillars.

After fabricating the SERS patterns above, probing molecules are dispensed on them to investigate the effectiveness in terms of signal magnification. Figure 5.17 (a) – (d) shows the results of Raman scattering intensity on these four patterns correspondingly. The signals of SERS substrates are collected after dropping 10 µL R6G with the concentration of 10 µM on a 6×6 mm^2 sample with four patterns (blue lines) and flat gold without any patterns (red lines).

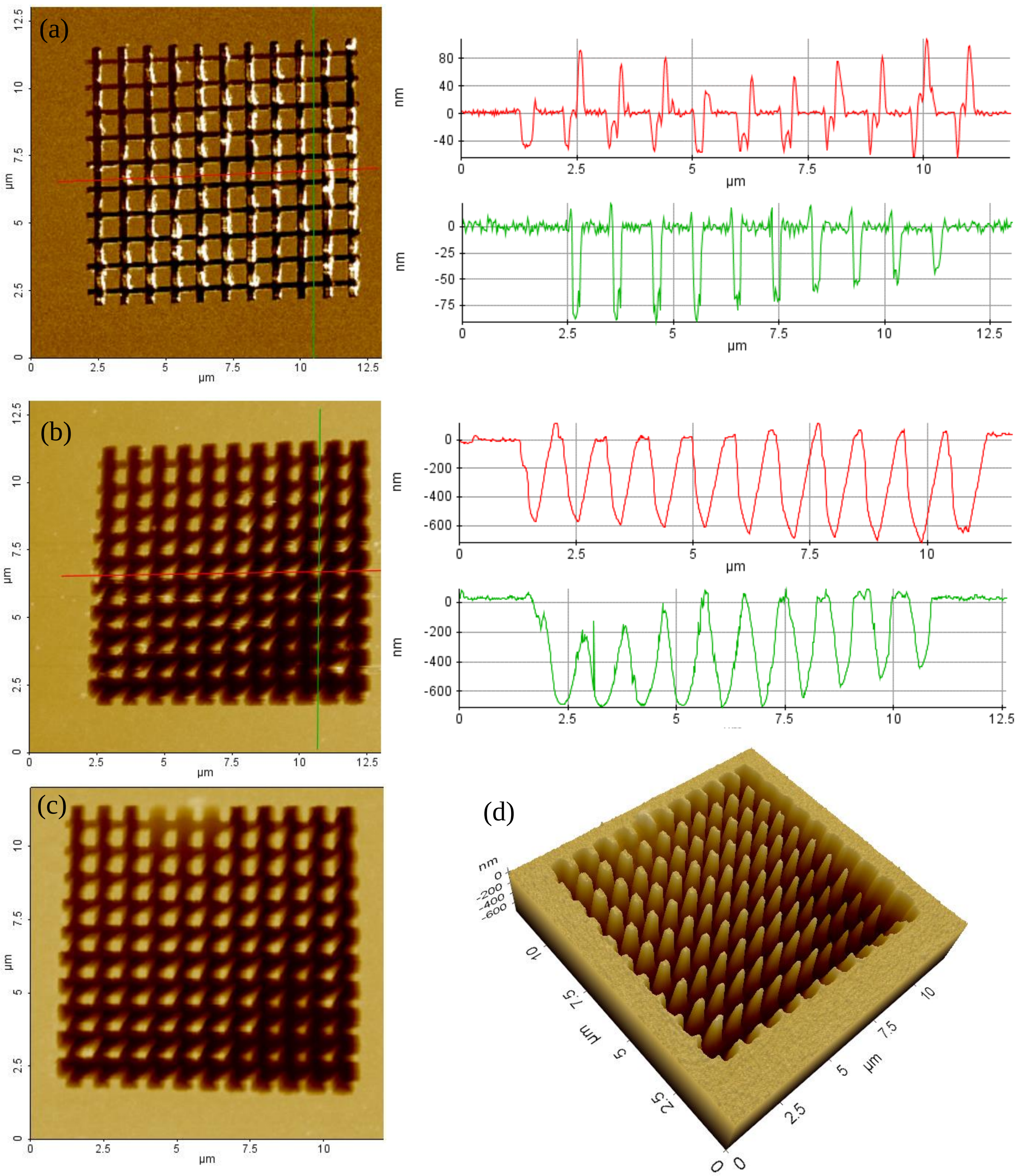

Figure 5.13 (a) 10×10 µm^2 PMMA pattern and its cross-sectional profiles after nanomachining. (b) Silicon pattern and its cross-sectional profiles after RIE. (c) Gold-coated silicon pattern after PVD. (d) Three-dimensional image of the gold-coated silicon pattern.

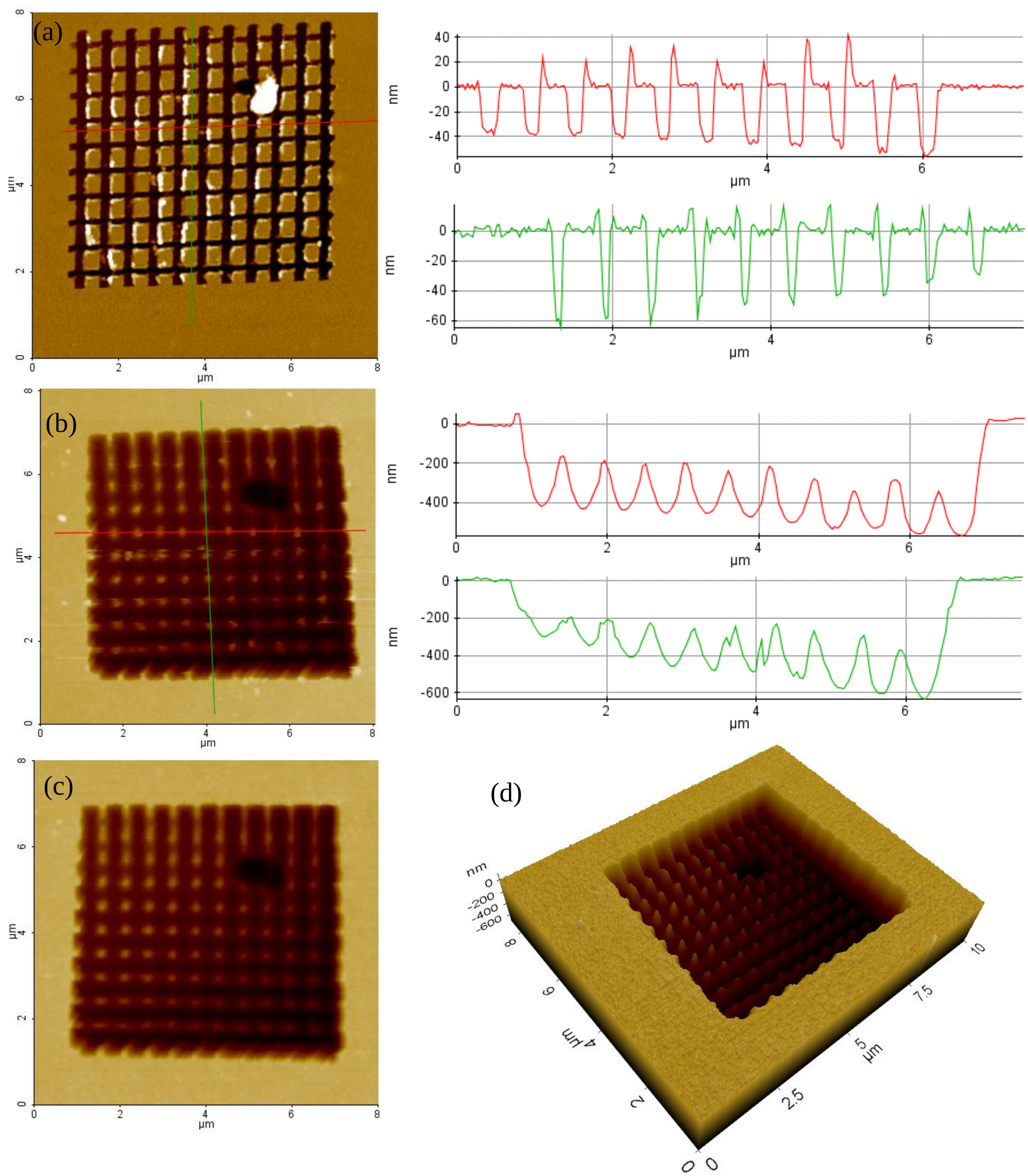

Figure 5.14 (a) 6×6 μm^2 PMMA pattern and its cross-sectional profiles after nanomachining. (b) Silicon pattern and its cross-sectional profiles after RIE. (c) Gold-coated silicon pattern after PVD. (d) Three-dimensional image of the gold-coated silicon pattern.

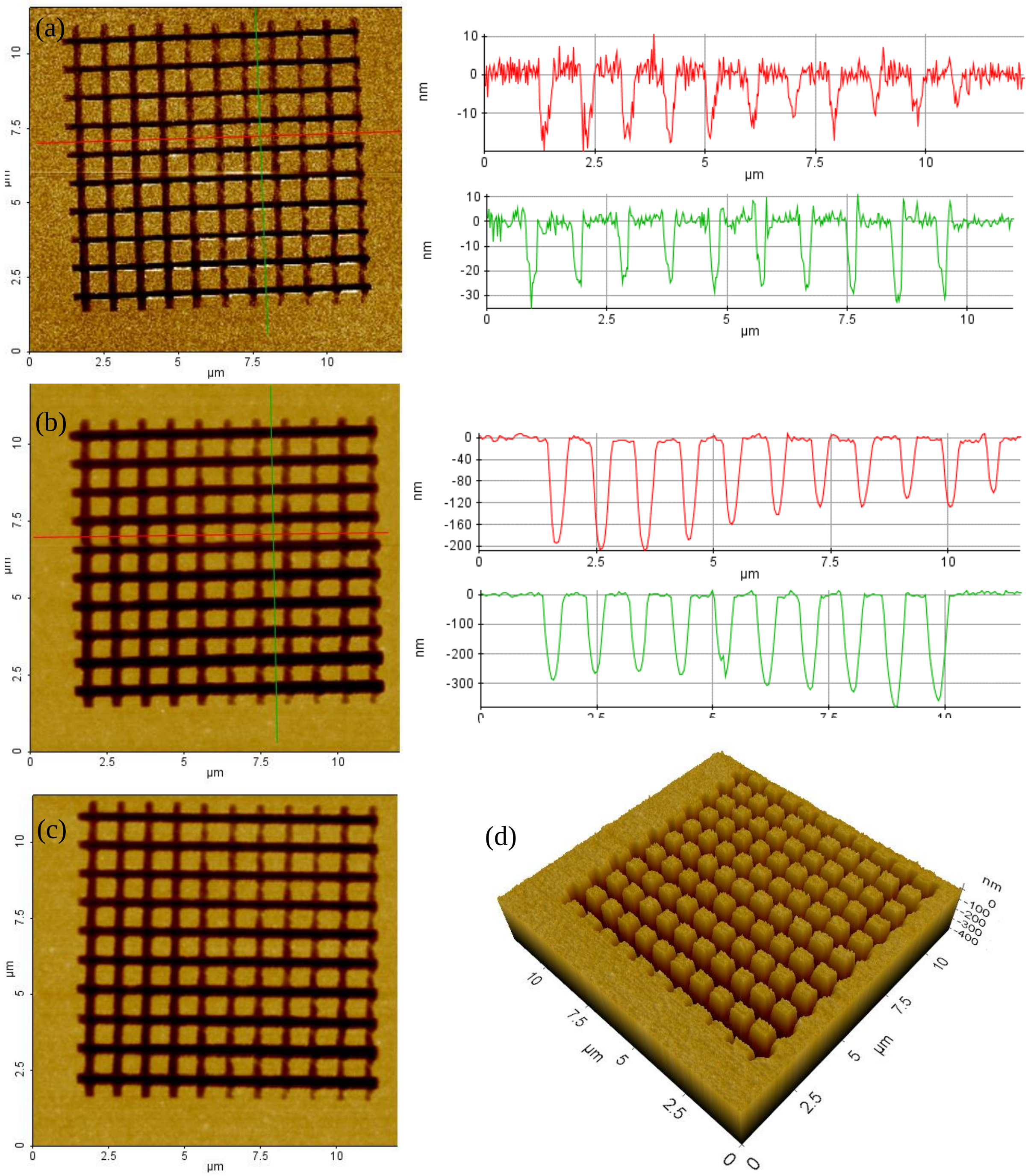

Figure 5.15 (a) 10×10 μm^2 PMMA pattern and its cross-sectional profiles after nanomachining. (b) Silicon pattern and its cross-sectional profiles after RIE. (c) Gold-coated silicon pattern after PVD. (d) Three-dimensional image of the gold-coated silicon pattern.

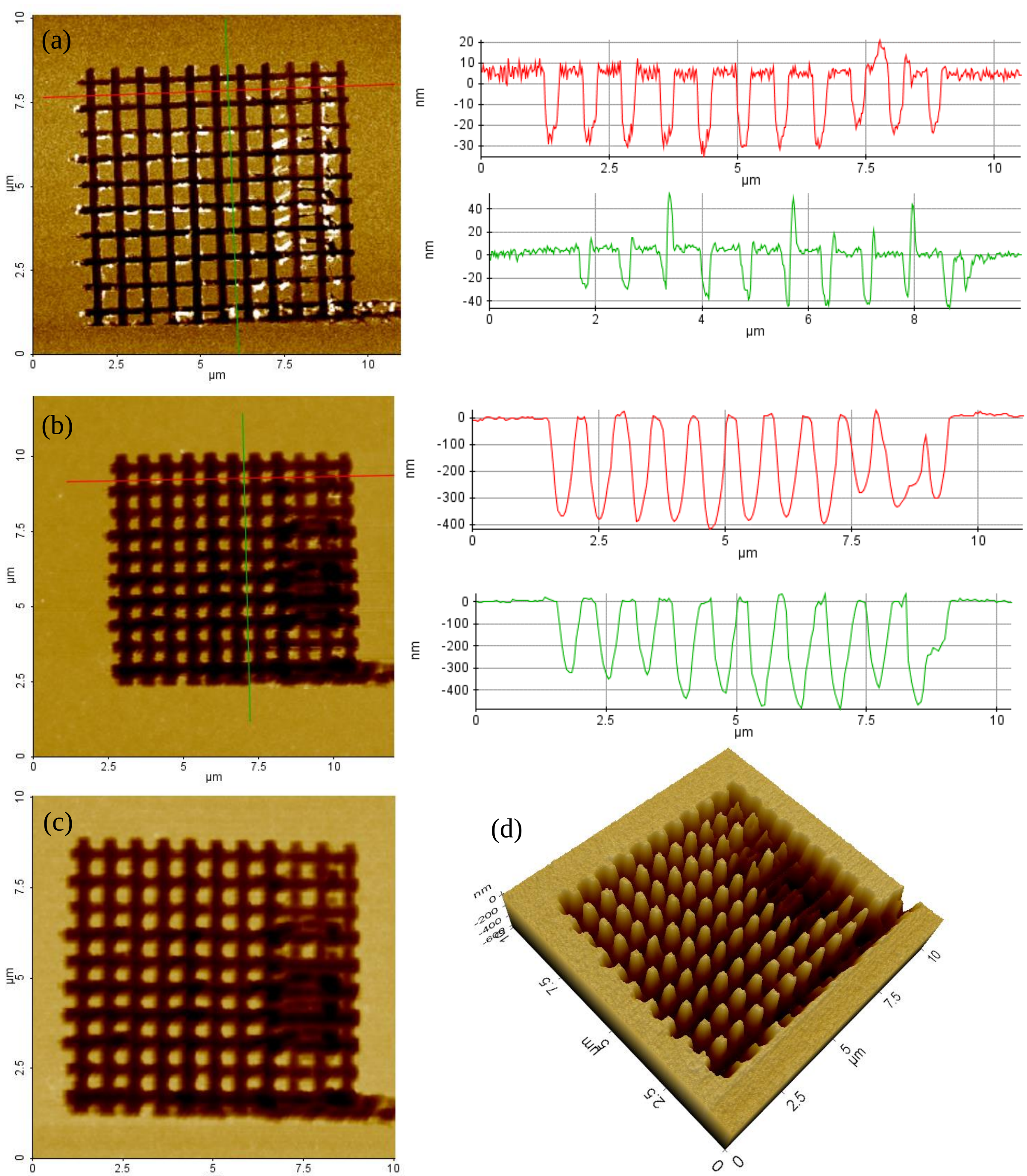

Figure 5.16 (a) 8×8 μm^2 PMMA pattern and its cross-sectional profiles after nanomachining. (b) Silicon pattern and its cross-sectional profiles after RIE. (c) Gold-coated silicon pattern after PVD. (d) Three-dimensional image of the gold-coated silicon pattern.

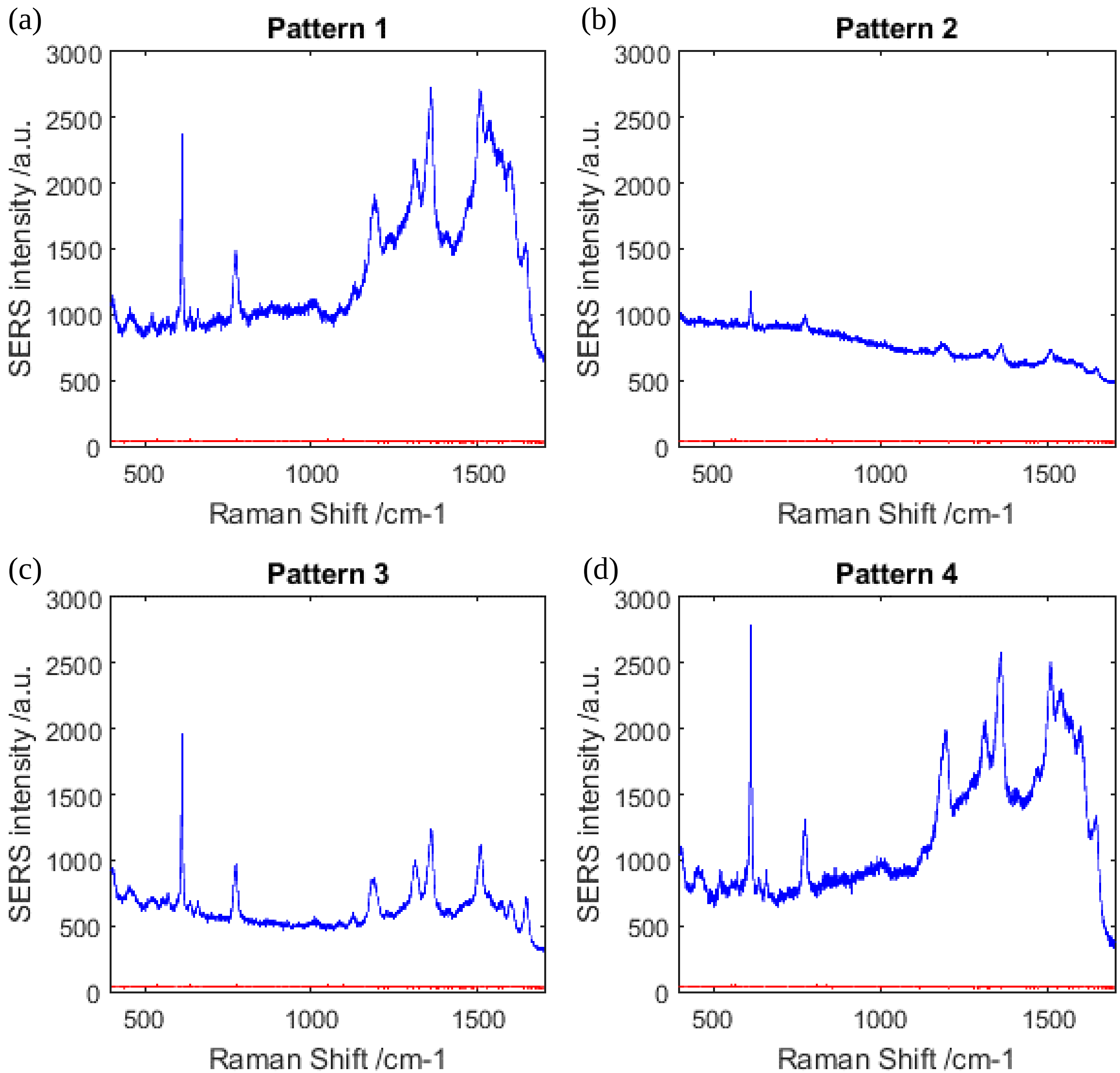

Figure 5.17 Raman scattering signals of SERS substrates after dropping 10 µL R6G with the concentration of 10 µM on a 6×6 mm^2 sample with (a) - (d) four patterns (blue lines) and flat gold without any patterns (red lines). These patterns are previous four patterns correspondingly.

(a)

(b)

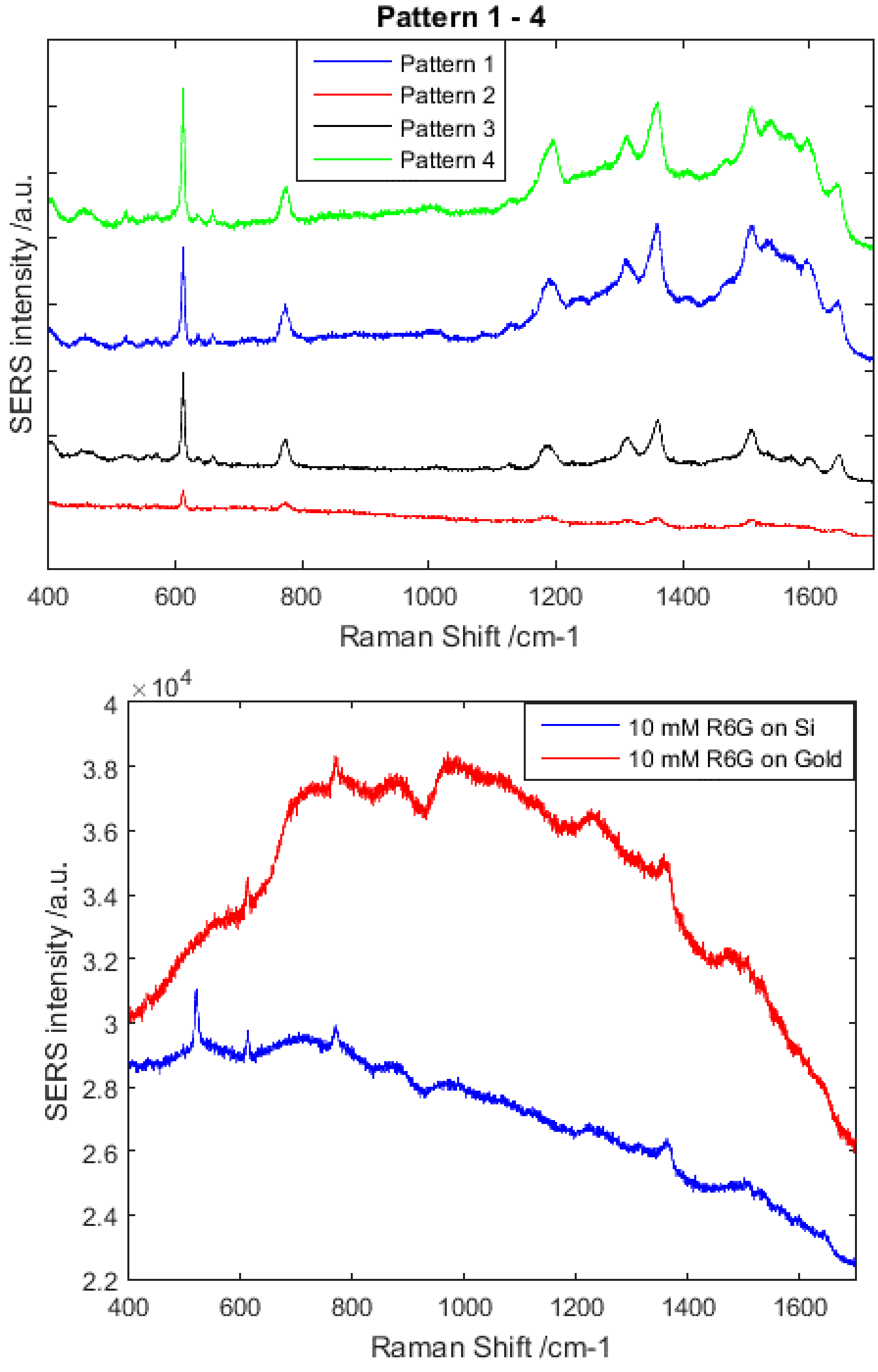

Figure 5.18 (a) Raman scattering signals of previous four patterns after dropping 10 µL R6G with the concentration of 10 µM on a 6×6 mm^2 sample. The peak counts are 805 and 645 at 612 $cm^{-1}$for gold and silicon substrates. (b) Raman scattering signals of 10 µL R6G with concentration of 10 mM on 6×6 mm^2 silicon (blue) and gold (red) substrates.

Figure 5.18 (a) shows the comparison of the SERS enhanced signals from four patterns. At Raman shift of 612 cm-1, pattern four has the largest count of 2009. Patterns 1 and 3 have the count of 1465 and 1308, respectively. The second pattern has the lowest SERS enhanced signals of 257.

Figure 5.18 (b) shows the normal Raman scattering signal of 10 μL R6G with concentration of 10 mM on 6×6 mm^2 silicon (blue line) and gold (red line) samples. At Raman shift of 612 cm-1, the gold and silicon substrates can result signals with the peak count of 805 and 645, respectively. The SERS enhancement factor can be calculated in its simplest form using Equation 5.1 [157]:

$$EF_{SERS} = \frac{I_{SERS}/N_{SERS}}{I_{NRS}/N_{NRS}} \tag{5.1}$$

where I_{SERS} and I_{NRS} are the SERS and normal Raman signal, and N_{SERS} and N_{NRS} are the number of molecules.

During the experiments, the laser power and integration time remain constant. Assuming the molecules are distributed u on the whole substrates after dispensing, so the number of the molecules are proportional to the concentration of the molecules. The enhancement factor of the SERS substrate of pattern four is 3.11×10^3. This is a reasonable enhancement factor that could detect 10 μM molecules. By dropping 10 μL on a 6×6 mm^2 sample, the probing molecules area density are 2.8×10^{-12} M/mm^2.

5.2.3 Conclusions on Fabrication of SERS Substrates

The results from the above two subsections gave us two options of fabricating SERS substrates. One is direct coating a gold layer on PMMA surface, and the other is to transfer the pattern onto silicon substrates before coating a gold layer. Both of them are able to enhance the intensity of Raman scattering in a reasonably discernable way in detecting Rhodamine chemicals with low concentration of 10 μM and the molecules area density of 2.8×10^{-12} M/mm^2. This is an easy, low cost and flexible approach of fabricating SERS substrates.

5.3 Chapter Summary

The previous developed 3D nanofabrication process is used as a novel technique in a few applications. Masters are fabricated for the low-cost and high-throughput soft lithography. I reversely molded 3D nanostructures on PDMS and duplicated them on PMMA substrates. Besides combining with complementary soft lithographic techniques, I fabricated some 3D nanostructures that can be either directly used or transferred on silicon as SERS substrates after coating 80 nm gold layers. They greatly enhanced the intensity of Raman scattering in the chemical detections with the enhancement factor of 3.11×10^3. These successful applications demonstrate the capability of the novel process of AFM-based 3D nanomachining.

CHAPTER 6 CONCLUSIONS AND FUTURE WORK

6.1 Research Summary

In this dissertation, I investigated the capability of AFM-based three dimensional nanofabrication processes. By fabricating various patterns, the 3D nanomachining process were developed and validated. Cleaning and transfer techniques were also developed and characterized after getting 3D patterns on PMMA. Two control modes were compared in terms of the results quality. In addition, RIE was used to transfer the 3D patterns on silicon substrates. After that, applications based on different 3D nanostructures were developed.

Based on the literature review, a novel three-dimensional nanofabrication process was developed using an AFM-based ultrasonic vibration assisted nanomachining system. In this system, the feature width of a single trench is increased with a high-frequency in plane circular xy-vibration. A virtual tool, whose diameter is controlled by the amplitude of xy-vibration, is able to achieve larger material removal rate than that of a regular AFM tip. The feature depth of a single trench increases with the involvement of ultrasonic vibration of sample in z-direction, which makes the 3D nanomachining process achievable. 3D nanostructures with complicated contours and continuously varying heights were fabricated on PMMA under both of the setpoint force control and z-height control. Setpoint force control allows the user to set a certain level of force on even tilting surfaces since it is a closed loop control system. Nevertheless, the noise and instability of force controlling during the machining process made the resulting surfaces have larger roughness than that of z-height control. The z-height control achieved better surfaces. But the disadvantage is that the absolute location of the AFM tip is open loop, so the AFM system needs to be warmed up in an appropriate long time before the nanomachining process.

After the nanomachining process, I developed a fluxing water-soluble film approach to remove the debris efficiently and effectively. By spin-coating a PVA layer on the PMMA substrate before nanomachining, PMMA debris comes off of the cavities of 3D nanostructures can be totally removed by combining the fluxing and ultrasonic bathing. It is essential to remove the debris. We could not get the dimensional information of 3D nanostructures without cleaning the sample, let alone using them in various applications. Furthermore, 3D nanostructures were transferred from PMMA surfaces onto silicon substrates using RIE process with shrinking or magnifying the feature depth capability. Recipes were characterized based on the functionality of the etching gas in the transfer process to achieve tunable selectivity and controllable surface finishes.

The validated 3D nanofabrication process with effective cleaning process were used in two applications, master fabrication for high-throughput soft lithography and SERS substrates fabrication for low concertation molecules detection. After reverse molding of 3D nanostructures on PDMS, 3D patterns were duplicated on new PMMA substrates. Tapered pillars were fabricated, which can be either directly used on PMMA or transferred on silicon as SERS substrates after coating 80 nm gold layers. They greatly enhanced the intensity of Raman scattering with the enhancement factor of 3.11×10^3. These applications strongly demonstrated the capability, flexibility, and compatibility with other existing techniques of the novel process of AFM-based 3D nanomachining.

6.2 Research Contributions

This novel AFM-based 3D nanomachining process provides a flexible and compatible approach of 3D nanofabrication. A summary of the contributions identified from the work are presented as follows:

1) This research developed and investigated a novel AFM-based 3D nanofabrication process. The characteristics of the process are discussed.
2) Two control modes, setpoint force and z-height, are investigated and compared in terms of fabricating 3D patterns by designing vectors and bitmap input images.
3) This research developed a novel fluxing water-soluble film approach to remove the debris during the nanomachining process effectively. In addition, it characterized the RIE recipe with the function of transferring nanostructures from PMMA to silicon in a controllable manner.
4) This research applied the novel nanofabrication process in applications. 3D masters in nanoscale are fabricated for high-throughput soft lithography and SERS substrates fabrication for low concertation molecules detection.

6.3 Future Work

Efficiency of fabricating 3D nanostructures is critical to all 3D fabrication process. In order to increase the fabrication speed, we need to increase the machining area per cutting path. However, it will decrease the resolution the 3D nanostructures can achieve. There is a trade-off in this static parameter controlling process. We may develop a control mechanism to dynamically control the amplitude of xy vibration to increase the area of one machining path if the machining ability is allowed this tuning process. With the help of xy vibration, virtual tool is formed during machining process. Tuning ability of xy vibrational amplitude is the ability of controlling the diameter of virtual tool. High resolution can be achieved with small xy vibrational amplitude, which can be applied when delicate features are need. For example, the teeth on the gear structure can be fabricated with higher resolution. On the contrary, large area can be machined with relative large xy vibrational amplitude, which can help increase the efficiency of this 3D nanofabrication process. Therefore, programmable integration of xy-vibarion and z-vibration control is also a promising research direction since this allows the dynamic controlling process easily achieved.

Another direction of the future work is further increase the lifetime of the AFM tip. With the assistance of the xy and z vibration, the AFM tip can machining longer distance with smaller tip wear on PMMA [19]. The machining process we developed are under room temperature. In the future, heating elements may be included in the nanomachining process since the PMMA yield strength decreases as the temperature increases. Therefore, as long as the working temperature not exceed the glass transition temperature, it is able to maintain the nanostructure after nanomachining. At the same time, there might be problems about PMMA debris sticking onto the AFM tip. Also, low temperature machining, milling and grinding processes are investigated. Low temperature nanomachining process might be another interesting future research direction.

In this dissertation, the only materials machined is PMMA. There are some materials with lower machinability are not covered yet, such as hard metal, silicon and rubber. For example, we know rubber is hard to machine, but cooling before machining makes it hard to deform and do not stick to the cutting edges of the tool.

In addition, applications done before can be further refined to get better results. For example, the pitch values of the SERS substrates could be reduced to improve the enhancement factor. The SAMIM process still has room to improve. The duplicated 3D nanostructures on new PMMA could have closer dimension comparing with the original PMMA patterns.

REFERENCES

[1] H. Gobel and P. von Blanckenhagen. Atomic force microscope as a tool for metal surface modifications. Presented at Third International Conference on Nanometer-Scale Science and Technology. 1995.

[2] B. A. Gozen and O. B. Ozdoganlar. A rotating-tip-based mechanical nano-manufacturing process: Nanomilling. *Nasno Scale Research Letters 5(9),* pp. 1403-7. 2010.

[3] L. G. Hector and S. R. Schmid. Simulation of asperity plowing in an atomic force microscope. part I. experimental and theoretical methods. *Wear 215(1-2),* pp. 247-256. 1998.

[4] S. Hu, S. Altmeyer, A. Hamidi, B. Spangenberg and H. Kurz. Novel approach to atomic force lithography. *Journal of Vacuum Science & Technology B (Microelectronics and Nanometer Structures) 16(4),* pp. 1983-6. 1998.

[5] X. Li, X. Wang, Q. Xiong and P. C. Eklund. Top-down structure and device fabrication using in situ nanomachining. *Appl. Phys. Lett. 87(23),* pp. 233113-1. 2005.

[6] S. R. Schmid and L. G. Hector. Simulation of asperity plowing in an atomic force microscope. II. plowing of aluminum alloys. *Wear 215(1-2),* pp. 257-66. 1998.

[7] M. Wendel, H. Lorenz and J. P. Kotthaus. Sharpened electron beam deposited tips for high resolution atomic force microscope lithography and imaging. *Appl. Phys. Lett. 67(25),* pp. 3732-4. 1995.

[8] Y. Yan, T. Sun, Y. Liang and S. Dong. Investigation on AFM-based micro/nano-CNC machining system. *International Journal of Machine Tools & Manufacture 47(11),* pp. 1651-9. 2007.

[9] Y. Yan, T. Sun, Y. Liang and S. Dong. Investigation on AFM-based micro/nano-CNC machining system. *International Journal of Machine Tools & Manufacture 47(11),* pp. 1651-9. 2007.

[10] J. Kim, D. C. Joy and S. -. Lee. Controlling resist thickness and etch depth for fabrication of 3D structures in electron-beam grayscale lithography. *Microelectronic Engineering 84(12),* pp. 2859-64. 2007.

[11] S. -. Lee and K. Anbumony. Accurate control of remaining resist depth for nanoscale three-dimensional structures in electron-beam grayscale lithography. *Journal of Vacuum*

Science & Technology B (Microelectronics and Nanometer Structures) 25(6), pp. 2008-12. 2007.

[12] M. Ali, T. Wagner, M. Shakoor and P. A. Molian. Review of laser nanomachining. *J. Laser Appl. 20(3),* pp. 169-184. 2008.

[13] L. Li, M. Hong, M. Schmidt, M. Zhong, A. Malshe, B. Huis In'Tveld and V. Kovalenko. Laser nano-manufacturing - state of the art and challenges. *CIRP Ann. Manuf. Technol. 60(2),* pp. 735-755. 2011.

[14] A. Albrecht, X. Wang, H. H. Mai, T. Schotzko, I. Memon, M. Bartels, M. Hornung and H. Hillmer. High vertical resolution 3D nanoimprint technology and its application in optical nanosensors. 2012.

[15] E. J. W. Berenschot, N. Burouni, B. Schurink, J. W. Van Honschoten, R. G. P. Sanders, R. Truckenmuller, H. V. Jansen, M. C. Elwenspoek, A. A. Van Apeldoorn and N. R. Tas. 3D nanofabrication of fluidic components by corner lithography. *Small 8(24),* pp. 3823-3831. 2012.

[16] Hong-Wei Li, Dae-Joon Kang, M. G. Blamire and W. T. S. Huck. Focused ion beam fabrication of silicon print masters. Presented at Trends in Nanotechnology (TNT 2002) Conference. 2003.

[17] N. Burouni, E. Berenschot, M. Elwenspoek and N. R. Tas. 3D nanofabrication of components by repeated corner lithography: Self aligned sub-50nm apertures. Presented at 2012 12th IEEE International Conference on Nanotechnology, NANO 2012, August 20, 2012 - August 23. 2012.

[18] L. Zhang, J. Dong and P. H. Cohen. Material-insensitive feature depth control and machining force reduction by ultrasonic vibration in AFM-based nanomachining. *IEEE Transactions on Nanotechnology 12(5),* pp. 743-50. 2013.

[19] L. Zhang and J. Dong. Ultrasonic vibration assisted nanomachining on PMMA with an AFM. Presented at SME Technical Papers - 4th Quarter 2012. 2012.

[20] D. R. S. Cumming, S. Thoms, J. M. R. Weaver and S. P. Beaumont. 3 nm NiCr wires made using electron beam lithography and PMMA resist. Presented at International Conference on Micro- and Nanofabrication. 1996.

[21] K. Liu, P. Avouris, J. Bucchignano, R. Martel, S. Sun and J. Michl. Simple fabrication scheme for sub-10 nm electrode gaps using electron-beam lithography. *Appl. Phys. Lett. 80(5),* pp. 865-7. 2002.

[22] Yang-Kyu Choi, N. Lindert, P. Xuan, S. Tang, D. Ha, E. Anderson, Tsu-Jae King, J. Bokor and C. Hu. Sub-20 nm CMOS FinFET technologies. Presented at Technical Digest. 2001.

[23] V. R. Manfrinato, L. Zhang, D. Su, H. Duan, R. G. Hobbs, E. A. Stach and K. K. Berggren. Resolution limits of electron-beam lithography toward the atomic scale. *Nano Letters 13(4),* pp. 1555-1558. 2013.

[24] D. Xia, J. Yan and S. Hou. Fabrication of nanofluidic biochips with nanochannels for applications in DNA analysis. *Small 8(18),* pp. 2787-2801. 2012.

[25] S. Cabrini, S. Dhuey, D. Cojoc, A. Carpentiero, M. Tormen and E. Di Fabrizio. Focused ion beam lithography applied to photonic and imprinting. Presented at Micromachining Technology for Micro-Optics and Nano-Optics V and Microfabrication Process Technology XII. 2007.

[26] N. Das, A. Karar, M. Vasiliev, L. T. Chee, K. Alameh and T. L. Yong. Analysis of nano-grating-assisted light absorption enhancement in metal-semiconductor-metal photodetectors patterned using focused ion-beam lithography. *Opt. Commun. 284(6),* pp. 1694-700. 2011.

[27] R. M. Langford. Focused ion beam nanof abri cat ion: A comparison with conventional processing techniques. *Journal of Nanoscience and Nanotechnology 6(3),* pp. 661-668. 2006.

[28] I. Utke, P. Hoffmann and J. Melngailis. Gas-assisted focused electron beam and ion beam processing and fabrication. *Journal of Vacuum Science & Technology B (Microelectronics and Nanometer Structures) 26(4),* pp. 1197-276. 2008.

[29] R. J. Young, J. R. A. Cleaver and H. Ahmed. Characteristics of gas-assisted focused ion beam etching. *Journal of Vacuum Science & Technology B (Microelectronics Processing and Phenomena) 11(2),* pp. 234-41. 1993.

[30] Wen-Di Li, W. Wu and R. S. Williams. Combined helium ion beam and nanoimprint lithography attains 4 nm half-pitch dense patterns. *Journal of Vacuum Science & Technology B (Microelectronics and Nanometer Structures) 30(6),* pp. 06-304. 2012.

[31] J. E. E. Baglin, A. J. Kellock and J. E. Frommer. Ion beam lithography for nano-scale pattern features. Presented at Ion-Beam-Based Nanofabrication Symposium. 2007.

[32] V. Gopal, V. R. Radmilovic, C. Daraio, S. Jin, P. Yang and E. A. Stach. Rapid prototyping of site-specific nanocontacts by electron and ion beam assisted direct-write nanolithography. *Nano Letters 4(11)*, pp. 2059-63. 2004.

[33] C. Wagner and N. Harned. EUV lithography: Lithography gets extreme. *Nature Photonics 4(1),* pp. 24-26. 2010.

[34] J. N. Burghartz, M. Irmscher, F. Letzkus, J. Kretz and D. Resnick. Lithography for the 32-nm node and beyond. Presented at 2006 Bipolar/BiCMOS Circuits and Technology Meeting. 2006.

[35] G. F. Lorusso, J. Hermans, A. M. Goethals, B. Baudemprez, F. Van Roey, A. M. Myers, I. Kim, B. S. Kim, R. M. Jonckheere, A. Niroomand, S. Lok, A. Van Dijk, J. -. de Marneffe, S. Demuynck, D. Goossens and K. Ronse. Imaging performance of the EUV alpha demo tool at IMEC. Presented at Emerging Lithographic Technologies XII. 2008.

[36] W. C. Seung, R. Ayothi, D. Bratton, D. Yang, N. Felix, H. B. Cao, H. Deng and C. K. Ober. Sub-50 nm feature sizes using positive tone molecular glass resists for EUV lithography. *Journal of Materials Chemistry 16(15),* pp. 1470-4. 2006.

[37] Y. Vladimirsky, "X-ray lithography towards 15 nm," Jefferson Laboratory Technical Note 03-016, January 2003.

[38] J. R. Maldonado and M. Peckerar. X-ray lithography: Some history, current status and future prospects. *Microelectronic Engineering 161*pp. 87-93. 2016.

[39] E. Di Fabrizio, R. Fillipo, S. Cabrini, R. Kumar, F. Perennes, M. Altissimo, L. Businaro, D. Cojac, L. Vaccari, M. Prasciolu and P. Candeloro. X-ray lithography for micro- and nano-fabrication at ELETTRA for interdisciplinary applications. *Journal of Physics: Condensed Matter 16(33),* pp. 3517-35. 2004.

[40] M. Faustini, B. Marmiroli, L. Malfatti, B. Louis, N. Krins, P. Falcaro, G. Grenci, C. Laberty-Robert, H. Amenitsch, P. Innocenzi and D. Grosso. Direct nano-in-micropatterning of TiO2 thin layers and TiO2/pt nanoelectrode arrays by deep X-ray lithography. *Journal of Materials Chemistry 21(11),* pp. 3597-603. 2011.

[41] Lin-Jun Wang, Jian-Min Liu, Qing-Feng Su, R. Xu, Hong-Yan Peng, Wei-Min Shi and Yi-Ben Xia. Optical characteristics of nano-crystalline diamond films as X-ray lithography masks for integrated circuit fabrication. Presented at 2006 8th International Conference on Solid-State and Integrated Circuit Technology. 2006.

[42] Y. Vladimirsky. X-ray lithography at CXrL-3D nanostructures. Presented at Tenth US National Conference. 1997.

[43] C. J. Buckley, R. Feder and M. T. Browne. Soft X-ray nano lithography of semitransparent masks for the generation of high-resolution high contrast zone plates. Presented at Short Wavelength Coherent Radiation: Generation and Applications. 1986.

[44] E. M. Di Fabrizio, D. Cojoc, S. Cabrini, L. Businaro, M. Altissimo, L. Vaccari, F. Romanato, R. Malureanu, B. Kaulich, T. Wilhein and J. Susini. Nano-optical elements fabricated by e-beam and x-ray lithography. Presented at Nano- and Micro-Optics for Information Systems. 2003.

[45] Y. L. Su, Y. N. Do, C. L. Hae, Chung-Jong Yu, Y. Hwu and C. K. Hyon. Direct-write X-ray lithography using a hard X-ray fresnel zone plate. *Journal of Synchrotron Radiation 22(3),* pp. 781-5. 2015.

[46] M. Truccato, A. Agostino, E. Borfecchia, L. Mino, E. Cara, A. Pagliero, N. Adhlakha, L. Pascale, L. Operti, E. Enrico, N. De Leo, M. Fretto, G. Martinez-Criado and C. Lamberti. Direct-write X-ray nanopatterning: A proof of concept josephson device on Bi2Sr2CaCu2O8+Superconducting oxide. *Nano Letters 16(3),* pp. 1669-1674. 2016.

[47] Y. Xia and G. M. Whitesides. Soft lithography. *Annual Review of Materials Science 28(1),* pp. 153-184. 1998.

[48] G. S. Watson, S. Myhra and J. A. Watson. Lithography of diamond-like-carbon (DLC) films for use as masters in soft-lithography. Presented at Device and Process Technologies for Microelectronics, MEMS and Photonics IV. 2005.

[49] M. S. R. Sankar and R. B. Gangineni. Study of nano imprinting using soft lithography on krafty glue PVDF polymer thin films. Presented at 58th DAE Solid State Physics Symposium 2013. 2014.

[50] J. Marczak, P. Slupski, P. Kunicki and K. Komorowska. Soft lithography processing of fresnel lens for on-chip applications. Presented at 2015 IEEE 15th International Conference on Nanotechnology (IEEE-NANO). 2015.

[51] K. Mogi, Y. Sugii, T. Yamamoto and T. Fujii. Rapid fabrication technique of nano/microfluidic device with high mechanical stability utilizing two-step soft lithography. *Sensors Actuators B: Chem. 201*pp. 407-12. 2014.

[52] V. Auzelyte, V. Flauraud, V. J. Cadarso, T. Kiefer and J. Brugger. Biomimetic soft lithography on curved nanostructured surfaces. *Microelectronic Engineering 97*pp. 269-71. 2012.

[53] K. Choi. Novel silicon-elastomers for advanced soft lithography. Presented at 2006 MRS Fall Meeting, November 27, 2006 - December 1. 2006.

[54] G. Binnig, C. F. Quate and C. Gerber. Atomic force microscope. *Phys. Rev. Lett. 56(9),* pp. 930-3. 1986.

[55] Y. Martin, C. C. Williams and H. K. Wickramasinghe. Atomic force microscope-force mapping and profiling on a sub 100-A scale. *J. Appl. Phys. 61(10),* pp. 4723-9. 1987.

[56] G. Meyer and N. M. Amer. Novel optical approach to atomic force microscopy. *Appl. Phys. Lett. 53(12),* pp. 1045-7. 1988.

[57] F. Ebrahimi and L. Kalwani. Fracture anisotropy in silicon single crystal. *Materials Science & Engineering A (Structural Materials: Properties, Microstructure and Processing) A268(1-2),* pp. 116-26. 1999.

[58] L. Chen, N. Morita and K. Ashida. Maskless pattern formation which used alkaline etching and nano-scale cutting by using friction force microscope. *Journal of the Japan Society of Precision Engineering 66(11),* pp. 1807-11. 2000.

[59] J. Guo, C. Song, X. Li, B. Yu, H. Dong, L. Qian and Z. Zhou. Fabrication mechanism of friction-induced selective etching on si(100) surface. *Nanoscale Research Letters 7*pp. 152 (9 pp.). 2012.

[60] C. Song, X. Li, B. Yu, H. Dong, L. Qian and Z. Zhou. Friction-induced nanofabrication method to produce protrusive nanostructures on quartz. *Nano Scale Research Letters 6*pp. 310 (9 pp.). 2011.

[61] C. Song, B. Yu and L. Qian. Effect of scan parameters and etching temperature on low-destructive nanofabrication of quartz. *Micro & Nano Letters 8(10),* pp. 735-9. 2013.

[62] B. Yu, H. Dong, L. Qian, Y. Chen, J. Yu and Z. Zhou. Friction-induced nanofabrication on monocrystalline silicon. *Nanotechnology 20(46),* pp. 465303 (8 pp.). 2009.

[63] B. Yu, L. Qian, H. Dong, J. Yu and Z. Zhou. Friction-induced hillocks on monocrystalline silicon in atmosphere and in vacuum. *Wear 268(9-10),* pp. 1095-102. 2010.

[64] B. Yu, X. Li, H. Dong, Y. Chen, L. Qian and Z. Zhou. Towards a deeper understanding of the formation of friction-induced hillocks on monocrystalline silicon. *J. Phys. D 45(14),* pp. 145301 (6 pp.). 2012.

[65] S. Miyake and J. Kim. Fabrication of silicon utilizing mechanochemical local oxidation by diamond tip sliding. *Japanese Journal of Applied Physics, Part 2 (Letters) 40(11),* pp. 1247-9. 2001.

[66] S. Miyake, M. Wang and J. Kim. Nano mechanical processing of silicon by atomic force microscopy. *Key Eng Mat 291-292*pp. 401-6. 2005.

[67] S. Miyake and J. Kim. Nanoprocessing of silicon by mechanochemical reaction using atomic force microscopy and additional potassium hydroxide solution etching. *Nanotechnology 16(1),* pp. 149-57. 2005.

[68] S. Miyake and J. Kim. Increase and decrease of etching rate of silicon due to diamond tip sliding by changing scanning density. *Japanese Journal of Applied Physics, Part 2 (Letters) 41(10),* pp. 1116-19. 2002.

[69] R. Magno and B. Bennett. Nanostructure patterns written in III–V semiconductors by an atomic force microscope. *Appl. Phys. Lett. 70(14),* pp. 1855-1857. 1997.

[70] M. Malekian, S. S. Park, D. Strathearn, M. G. Mostofa and M. B. G. Jun. Atomic force microscope probe-based nanometric scribing. *J Micromech Microengineering 20(11),* pp. 115016 (11 pp.). 2010.

[71] R. Rank, H. Brueckl, J. Kretz, I. Moench and G. Reiss. Nanoscale modification of conducting lines with a scanning force microscope. *Vacuum 48(5),* pp. 467-472. 1997.

[72] T. Sumomogi, T. Endo, K. Kuwahara, R. Kaneko and T. Miyamoto. Micromachining of metal surfaces by scanning probe microscope. Presented at International Conference on Scanning Tunneling Microscopy (STM '93). 1994.

[73] Te-Hua Fang and Win-Jin Chang. Effects of AFM-based nanomachining process on aluminum surface. *Journal of the Physics and Chemistry of Solids 64(6),* pp. 913-18. 2003.

[74] B. Cappella, H. Sturm and S. M. Weidner. Breaking polymer chains by dynamic plowing lithography. *Polymer 43(16),* pp. 4461-6. 2002.

[75] B. Cappella and H. Sturm. Comparison between dynamic plowing lithography and nanoindentation methods. *J. Appl. Phys. 91(1),* pp. 506-12. 2002.

[76] M. Wendel, S. Kuhn, H. Lorenz, J. P. Kotthaus and M. Holland. Nanolithography with an atomic force microscope for integrated fabrication of quantum electronic devices. *Appl. Phys. Lett. 65(14),* pp. 1775-7. 1994.

[77] B. Klehn and U. Kunze. SiO2 and si nanoscale patterning with an atomic force microscope. *Superlattices and Microstructures 23(2),* pp. 441-4. 1998.

[78] B. Klehn and U. Kunze. Nanolithography with an atomic force microscope by means of vector-scan controlled dynamic plowing. *J. Appl. Phys. 85(7),* pp. 3897-3903. 1999.

[79] S. Skaberna, M. Versen, B. Klehn, U. Kunze, D. Reuter and A. D. Wieck. Fabrication of a quantum point contact by the dynamic plowing technique and wet-chemical etching. Presented at International Conference on Scanning Probe Microscopy, Cantilever Sensors and Nanostructures. 2000.

[80] B. Vasic, M. Kratzer, A. Matkovic, A. Nevosad, U. Ralevic, D. Jovanovic, C. Ganser, C. Teichert and R. Gajic. Atomic force microscopy based manipulation of graphene using dynamic plowing lithography. *Nanotechnology 24(1),* pp. 015303 (9 pp.). 2013.

[81] M. Heyde, K. Rademann, B. Cappella, M. Geuss, H. Sturm, T. Spangenberg and H. Niehus. Dynamic plowing nanolithography on polymethylmethacrylate using an atomic force microscope. *Rev. Sci. Instrum. 72(1),* pp. 136-41. 2001.

[82] M. Heyde, B. Cappella, H. Sturm, C. Ritter and K. Rademann. Dislocation of antimony clusters on graphite by means of dynamic plowing nanolithography. *Surf. Sci. 476(1-2),* pp. 54-62. 2001.

[83] A. Majumdar, P. I. Oden, J. P. Carrejo, L. A. Nagahara, J. J. Graham and J. Alexander. Nanometer-scale lithography using the atomic force microscope. *Appl. Phys. Lett. 61(19),* pp. 2293-5. 1992.

[84] K. Wilder, C. F. Quate, D. Adderton, R. Bernstein and V. Elings. Noncontact nanolithography using the atomic force microscope. *Appl. Phys. Lett. 73(17),* pp. 2527-9. 1998.

[85] R. Nemutudi, N. J. Curson, N. J. Appleyard, D. A. Ritchie and G. A. C. Jones. Modification of a shallow 2DEG by AFM lithography. Presented at 26th International Conference on Micro- and Nano-Engineering. 2001.

[86] M. Yasutake, Y. Ejiri and T. Hattori. Modification of silicon surface using atomic force microscope with conducting probe. *Jpn J Appl Phys Part 2 Letter 32(7),* pp. L1021-L1023. 1993.

[87] H. C. Day and D. R. Allee. Selective area oxidation of silicon with a scanning force microscope. *Appl. Phys. Lett. 62(21),* pp. 2691-3. 1993.

[88] R. Garcia, M. Calleja and F. Perez-Murano. Local oxidation of silicon surfaces by dynamic force microscopy: Nanofabrication and water bridge formation. *Appl. Phys. Lett. 72(18),* pp. 2295-7. 1998.

[89] M. Calleja and R. Garcia. Nano-oxidation of silicon surfaces by noncontact atomic-force microscopy: Size dependence on voltage and pulse duration. *Appl. Phys. Lett. 76(23),* pp. 3427-9. 2000.

[90] A. M. Abdullah, S. D. Hutagalung and Z. Lockman. Influence of room humidity on the formation of nanoscale silicon oxide patterned by AFM lithography. *International Journal of Nanoscience 9(4),* pp. 251-5. 2010.

[91] F. S. S. Chien, J. -. Chang, S. -. Lin, Y. -. Chou, T. T. Chen, S. Gwo, T. -. Chao and W. -. Hsieh. Nanometer-scale conversion of Si3N4 to SiOx. *Appl. Phys. Lett. 76(3),* pp. 360-2. 2000.

[92] F. S. -. Chien, Y. C. Chou, T. T. Chen, W. -. Hsieh, T. -. Chao and S. Gwo. Nano-oxidation of silicon nitride films with an atomic force microscope: Chemical mapping, kinetics, and applications. *J. Appl. Phys. 89(4),* pp. 2465-72. 2001.

[93] X. N. Xie, H. J. Chung, C. H. Sow and A. T. S. Wee. Native oxide decomposition and local oxidation of 6H-SiC (0001) surface by atomic force microscopy. *Appl. Phys. Lett. 84(24),* pp. 4914-16. 2004.

[94] Xiang-Zheng Bo, L. P. Rokhinson, H. Yin, D. C. Tsui and J. C. Sturm. Nanopatterning of si/SiGe electrical devices by atomic force microscopy oxidation. *Appl. Phys. Lett. 81(17),* pp. 3263-5. 2002.

[95] B. W. Maynor, J. Li, C. Lu and J. Liu. Site-specific fabrication of nanoscale heterostructures: Local chemical modification of GaN nanowires using electrochemical dip-pen nanolithography. *J. Am. Chem. Soc. 126(20),* pp. 6409-6413. 2004.

[96] M. Ishii and K. Matsumoto. Control of current in 2DEG channel by oxide wire formed using AFM. Presented at 1994 International Conference on Solid State Devices and Materials (SSDM '94). 1995.

[97] V. Cambel, J. Martaus, J. Soltys, R. Kudela and D. Gregusova. Local anodic oxidation by AFM tip developed for novel semiconductor nanodevices. *Ultramicroscopy 108(10),* pp. 1021-4. 2008.

[98] X. N. Xie, A. T. S. Wee, H. J. Chung and C. H. Sow. Nanoscale materials patterning and engineering by atomic force microscopy nanolithography. *Materials Science & Engineering R: Reports 54(1-2),* pp. 1-48. 2006.

[99] E. S. Snow and P. M. Campbell. AFM fabrication of sub-10-nanometer metal-oxide devices with in situ control of electrical properties. *Science 270(5242),* pp. 1639-41. 1995.

[100] K. Matsumoto, Y. Gotoh, T. Maeda, J. A. Dagata and J. S. Harris. Room-temperature single-electron memory made by pulse-mode atomic force microscopy nano oxidation process on atomically flat -alumina substrate. *Appl. Phys. Lett. 76(2),* pp. 239-41. 2000.

[101] R. D. Piner, J. Zhu, F. Xu, S. Hong and C. A. Mirkin. Dip-pen nanolithography. *Science 283(5402),* pp. 661-3. 1999.

[102] N. A. Amro, S. Xu and G. Liu. Patterning surfaces using tip-directed displacement and self-assembly. *Langmuir 16(7),* pp. 3006-3009. 2000.

[103] B. W. Maynor, Y. Li and J. Liu. Au "ink" for AFM "dip-pen" nanolithography. *Langmuir 17(9),* pp. 2575-2578. 2001.

[104] S. Hong and C. A. Mirkin. A nanoplotter with both parallel and serial writing capabilities. *Science 288(5472),* pp. 1808-11. 2000.

[105] M. Zhang, D. Bullen, S. Chung, S. Hong, K. S. Ryu, Z. Fan, C. A. Mirkin and C. Liu. A MEMS nanoplotter with high-density parallel dip-pen nanolithography probe arrays. *Nanotechnology 13(2),* pp. 212-217. 2002.

[106] D. Bullen, X. Wang, J. Zou, S. Chung, C. A. Mirkin and C. Liu. Design, fabrication, and characterization of thermally actuated probe arrays for dip pen nanolithography. *J Microelectromech Syst 13(4),* pp. 594-602. 2004.

[107] D. Bullen, S. Chung, X. Wang, J. Zou, C. A. Mirkin and C. Liu. Parallel dip-pen nanolithography with arrays of individually addressable cantilevers. *Appl. Phys. Lett. 84(5),* pp. 789-791. 2004.

[108] K. Salaita, S. W. Lee, X. Wang, L. Huang, T. M. Dellinger, C. Liu and C. A. Mirkin. Sub-100 nm, centimeter-scale, parallel dip-pen nanolithography. *Small 1(10),* pp. 940-945. 2005.

[109] K. Salaita, Y. Wang, J. Fragala, R. A. Vega, C. Liu and C. A. Mirkin. Massively parallel dip-pen nanolithography with 55 000-pen two-dimensional arrays. *Angewandte Chemie - International Edition 45(43),* pp. 7220-7223. 2006.

[110] C. A. Mirkin. The power of the pen: Development of parallel dip-pen*massively nanolithography. *ACS Nano 1(2),* pp. 79-83. 2007.

[111] H. Zhang, N. A. Amro, S. Disawal, R. Elghanian, R. Shile and J. Fragala. High-throughput dip-pen-nanolithography-based fabrication of si nanostructures. *Small 3(1),* pp. 81-85. 2007.

[112] L. Huang, A. B. Braunschweig, W. Shim, L. Qin, K. L. Jong, S. J. Hurst, F. Huo, C. Xue, Jae-Won Jang and C. A. Mirkin. Matrix-assisted dip-pen nanolithography and polymer pen lithography. *Small 6(10),* pp. 1077-81. 2010.

[113] Ki-Bum Lee, So-Jung Park, C. A. Mirkin, J. C. Smith and M. Mrksich. Protein nanoarrays generated by dip-pen nanolithography. *Science 295(5560),* pp. 1702-5. 2002.

[114] R. B. Salazar, A. Shovsky, H. Schonherr and G. J. Vancso. Dip-pen nanolithography on (bio)reactive monolayer and block-copolymer platforms: Deposition of lines of single macromolecules. *Small 2(11),* pp. 1274-82. 2006.

[115] J. Hyun, W. Lee, N. Nath, A. Chilkoti and S. Zauscher. Capture and release of proteins on the nanoscale by stimuli-responsive elastin-like polypeptide "switches". *J. Am. Chem. Soc. 126(23),* pp. 7330-7335. 2004.

[116] K. Yamazaki and H. Yamaguchi. Flexible nanofabrication in three-dimensional electron-beam lithography enhanced by suppression of proximity effect. *Applied Physics Express 1(9),* pp. 0970011-0970013. 2008.

[117] K. Yamazaki, T. Yamaguchi and H. Namatsu. Three-dimensional nanofabrication with 10-nm resolution. *Japanese Journal of Applied Physics, Part 2 (Letters) 43(8),* pp. 1111-13. 2004.

[118] H. O. Seung, J. G. Kim, S. K. Chang, S. Chang, S. Lee and Y. J. Myung. The fabrication of three-dimensional nano-structures by defocused electron beam energy. *Microelectronic Engineering 88(6),* pp. 914-22. 2011.

[119] A. Schleunitz and H. Schift. Fabrication of 3D nanoimprint stamps with continuous reliefs using dose-modulated electron beam lithography and thermal reflow. *J Micromech Microengineering 20(9),* 2010.

[120] D. Pires, J. L. Hedrick, A. De Silva, J. Frommer, B. Gotsmann, H. Wolf, M. Despont, U. Duerig and A. W. Knoll. Nanoscale three-dimensional patterning of molecular resists by scanning probes. *Science 328(5979),* pp. 732-5. 2010.

[121] J. Taniguchi, K. Koga, Y. Kogo and I. Miyamoto. Rapid and three-dimensional nanoimprint template fabrication technology using focused ion beam lithography. *Microelectronic Engineering 83(4-9),* pp. 940-943. 2006.

[122] Y. Yan, Z. Hu, X. Zhao, T. Sun, S. Dong and X. Li. Top-down nanomechanical machining of three-dimensional nanostructures by atomic force microscopy. *Small 6(6),* pp. 724-8. 2010.

[123] Y. Mao, K. Kuo, C. Tseng, J. Huang, Y. Lai, J. Yen, C. Lee and W. Chuang. Research on three dimensional machining effects using atomic force microscope. *Rev. Sci. Instrum. 80(6),* 2009.

[124] A. W. Knoll, D. Pires, O. Coulembier, P. Dubois, J. L. Hedrick, J. Frommer and U. Duerig. Probe-based 3-D nanolithography using self-amplified depolymerization polymers. *Adv Mater 22(31),* pp. 3361-3365. 2010.

[125] S. Miyake and J. Kim. Nanoprocessing of silicon by mechanochemical reaction using atomic force microscopy and additional potassium hydroxide solution etching. *Nanotechnology 16(1),* pp. 149-57. 2005.

[126] G. Piaszenski, U. Barth, A. Rudzinski, A. Rampe, A. Fuchs, M. Bender and U. Plachetka. 3D structures for UV-NIL template fabrication with grayscale e-beam lithography. *Microelectronic Engineering 84(5-8),* pp. 945-8. 2007.

[127] L. Yu, R. J. Kasica, R. N. Newby, L. Chen and V. K. Luciani. The evaluation of photo/e-beam complementary grayscale lithography for high topography 3D structure. Presented at Advances in Resist Materials and Processing Technology XXX. 2013.

[128] C. David and D. Hambach. Line width control using a defocused low voltage electron beam. Presented at International Conference on Micro-and Nanofabrication. 1999.

[129] B. Niemann, T. Wilhein, T. Schliebe, R. Plontke, O. Fortagne, I. Stolberg and M. Zierbock. A special method to create gratings of variable line density by low voltage electron beam lithography. Presented at International Conference on Micro- and Nanofabrication. 1996.

[130] K. Yamazaki and H. Namatsu. Two-axis-of-rotation drive system in electron-beam lithography apparatus for nanotechnology applications. Presented at 29th International Conference on Micro and Nano Engineering. 2004.

[131] H. D. Wanzenboeck and S. Waid. *Focused Ion Beam Lithography* 2011.

[132] S. Waid, H. D. Wanzenboeck, M. Muehlberger, M. Gavagnin and E. Bertagnolli. Generation of 3D nanopatterns with smooth surfaces. *Nanotechnology 25(31),* pp. 315302 (10 pp.). 2014.

[133] W. Wu, M. Hu, S. O. Fung, Z. Li and R. S. Williams. Cones fabricated by 3D nanoimprint lithography for highly sensitive surface enhanced raman spectroscopy. *Nanotechnology 21(25),* pp. 255502 (6 pp.). 2010.

[134] X. Wang, A. Albrecht, H. H. Mai, C. Woidt, T. Meinl, M. Hornung, M. Bartels and H. Hillmer. High resolution 3D NanoImprint technology: Template fabrication, application in fabry-perot-filter-array-based optical nanospectrometers. *Microelectronic Engineering 110*pp. 44-51. 2013.

[135] H. H. Mai, A. Albrecht, C. Woidt, X. Wang, V. Daneker, O. Setyawati, T. Woit, K. Schultz, M. Bartels and H. Hillmer. 3D nanoimprinted fabry-perot filter arrays and methodologies for optical characterization. *Appl. Phy. B 107(3),* pp. 755-764. 2012.

[136] M. Konijn, M. M. Alkaisi and R. J. Blaikie. Nanoimprint lithography of sub-100 nm 3D structures. Presented at Proceedings of the 30th International Conference on Micro- and Nano-Engineering, September 19, 2004 - September 22. 2005.

[137] N. Kehagias, M. Zelsmann and C. M. S. Torres. Polymer optical devices made by reverse and 3D nanoimprint lithography. Presented at Opto-Ireland 2005: Optoelectronics, Photonic Devices, and Optical Networks. 2005.

[138] Y. Jung and X. Cheng. Self-aligned metallization on organic semiconductor through 3D dual-layer thermal nanoimprint. *J Micromech Microengineering 24(9),* pp. 095009 (9 pp.). 2014.

[139] F. Yesilkoy, V. Flauraud, M. Ruegg, B. J. Kim and J. Brugger. 3D nanostructures fabricated by advanced stencil lithography. *Nanoscale 8(9),* pp. 4945-4950. 2016.

[140] P. C. Ma, K. Zhang and W. Wu. Novel 3D nano-fence matrixes for integrated nanofluidic channels. Presented at 2014 9th IEEE International Conference on Nano/Micro Engineered and Molecular Systems (NEMS). 2014.

[141] J. M. Perry, Z. D. Harms and S. C. Jacobson. 3D nanofluidic channels shaped by electron-beam-induced etching. *Small 8(10),* pp. 1521-6. 2012.

[142] S. M. Stavis, E. A. Strychalski and M. Gaitan. Nanofluidic structures with complex three-dimensional surfaces. *Nanotechnology 20(16),* pp. 165302 (7 pp.). 2009.

[143] J. Hoffmann, C. Hafner, P. Leidenberger, J. Hesselbarth and S. Burger. Comparison of electromagnetic field solvers for the 3D analysis of plasmonic nano antennas. Presented at Modeling Aspects in Optical Metrology II. 2009.

[144] M. Malerba, M. Dipalo, G. C. Messina, H. Amin, R. La Rocca, V. Shalabaeva, A. Simi, A. Maccione, L. Berdondini and F. De Angelis. Novel 3D plasmonic nano-electrodes for cellular investigations and neural interfaces. Presented at Biosensing and Nanomedicine VII. 2014.

[145] M. Shafieipour and V. Okhmatovski. Error-controlled boundary element modeling of 3D plasmonic nano-structures via higher-order locally corrected nystrom method. Presented at 2015 IEEE International Symposium on Antennas and Propagation & USNC/URSI National Radio Science Meeting. 2015.

[146] H. Choo, Myung-Ki Kim, M. Staffaroni, J. S. Tae, J. Bokor, S. Cabrini, P. J. Schuck, M. C. Wu and E. Yablonovitch. Nanofocusing in a metal-insulator-metal gap plasmon waveguide with a three-dimensional linear taper. *Nature Photonics 6(12),* pp. 838-44. 2012.

[147] H. Choo. 3D nanofocusing plasmonic waveguide. Presented at 2014 International Conference on Optical MEMS and Nanophotonics (OMN). 2014.

[148] N. C. Lindquist, P. Nagpal, A. Lesuffleur, D. J. Norris and S. Oh. Three-dimensional plasmonic nanofocusing. *Nano Letters 10(4),* pp. 1369-1373. 2010.

[149] A. A. Zharov, N. A. Zharova, D. A. Smirnova and A. A. Zharov J. Three-dimensional nanofocusing of light through surface plasmon scattering by a lump-like defect in metal/dielectric/metal slot waveguides. *Journal of the Optical Society of America B (Optical Physics) 30(3),* pp. 626-30. 2013.

[150] L. Gao, S. Xu, C. Xue, Z. Hai, D. Sun and Y. Lu. Self-assembly of hierarchical 3D starfish-like Co3O4nanowire bundles on nickel foam for high-performance supercapacitor. *Journal of Nanoparticle Research 18(5),* 2016.

[151] L. Mao, C. Guan, X. Huang, Q. Ke, Y. Zhang and J. Wang. 3D graphene-nickel hydroxide hydrogel electrode for high-performance supercapacitor. *Electrochim. Acta 196*pp. 653-660. 2016.

[152] J. Zhu, L. Cao, Y. Wu, Y. Gong, Z. Liu, H. E. Hoster, Y. Zhang, S. Zhang, S. Yang, Q. Yan, P. M. Ajayan and R. Vajtai. Building 3D structures of vanadium pentoxide nanosheets and application as electrodes in supercapacitors. *Nano Letters 13(11),* pp. 5408-5413. 2013.

[153] N. C. Lindquist, T. W. Johnson, P. Nagpal, D. J. Norris and S. Oh. Plasmonic nanofocusing with a metallic pyramid and an integrated C-shaped aperture. *Scientific Reports 3*pp. 1857. 2013.

[154] W. Isaacson. *Steve Jobs* 2011.

[155] "File: Singlemode fibre structure.png - Wikimedia commons," 2007. [Online]. Available: https://commons.wikimedia.org/wiki/File:Singlemode_fibre_structure.png. Accessed: Jun. 22, 2016.

[156] Koshelev, Alexander, Giuseppe Calafiore, Carlos Piña-Hernandez, Frances Allen, Scott Dhuey, Simone Sassolini, Edward Wong, Paul Lum, Keiko Munechika, and Stefano Cabrini. High refractive index Fresnel lens on a fiber fabricated by nanoimprint lithography for immersion applications. arXiv preprint arXiv:1606.02322 (2016).

[157] Kleinman, Samuel L., et al. "Creating, characterizing, and controlling chemistry with SERS hot spots." Physical Chemistry Chemical Physics 15.1 (2013): 21-36.

[158] Lopes, J. F., & Simoneau, C. (2014). Solubility of Polyvinyl Alcohol in Ethanol. EFSA Supporting Publications, 11(9).